2010

Tuning The Properties Of Nanomaterials As Function Of Surface And Environment

Ajay Karakoti
University of Central Florida

TUNING THE PROPERTIES OF NANOMATERIALS AS A FUNCTION OF SURFACE AND ENVIRONMENT

by

AJAY SINGH KARAKOTI

Master of Science (Chemistry) University of Delhi, India, 2001

Master of Technology (Corrosion Science) IIT Bombay, India, 2003

A dissertation submitted in partial fulfillment of the requirements
for the degree of Doctor of Philosophy
in the Department of Mechanical, Materials and Aerospace Engineering
in the College of Engineering and Computer Science
at the University of Central Florida
Orlando, Florida, USA

Summer Term
2010

Major Professor: Sudipta Seal

ABSTRACT

Nanotechnology has shaped the research and development in various disciplines of science and technology by redefining the interdisciplinary research. It has put the materials science at the forefront of technology by allowing the researchers to engineer materials with properties ranging from electronics to biomedical by using materials as diverse as ceramics to just plain carbon. These exceptional properties are achieved by minimizing the dimension of particles in such smaller domains that the boundary between the individual atoms, ions or cluster of particles is very small. This results in a change in conventional properties of particles from continuum physics to quantum physics and hence the properties of nanoparticles can be tuned based upon their size, shape and dimensionality. One of the most apparent changes upon decreasing the particle size is the increase in surface area to volume ratio. Thus nanoparticles possess greater tendency to interact with the environment in which they are present and similarly the environment can affect the properties of nanomaterials. The environment here is described as the immediate solid, liquid or gaseous material in immediate contact with the external surface of the nanoparticles. In order to control the physico-chemical properties of nanoparticles it is important to control the surface characteristics of nanoparticles and its immediate environment. The current thesis emphasizes the role of tuning the surface of nanoparticles and/or the environment around the nanoparticles to control their properties.

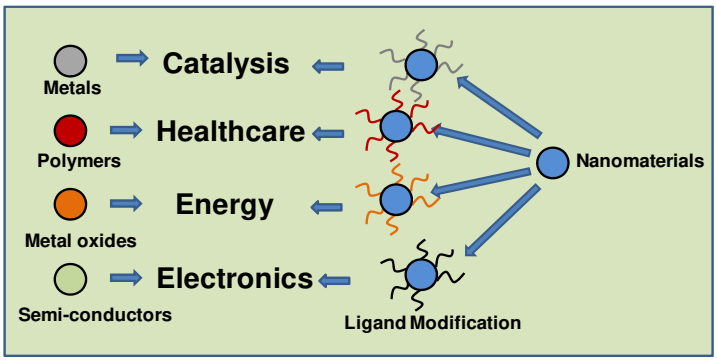

Schematic A1 - Schematic diagram demonstrating the importance of surface modified nanoparticles to achieve various function from a single platform nanomaterial.

The schematic describes the current approach in literature in which a platform nanoparticle can be used for a myriad of applications by just changing the surface species which tunes the property of nanoparticles. Such surface modification can provide nanomaterials with hydrophilic, hydrophobic, biocompatible, sensing, fluorescence and/or electron transfer properties.

The current thesis demonstrates the interaction between nanoparticles and the environment by changing the surface characteristics of nanomaterials through the use of oxide nanoparticles as examples. The first part of the thesis discusses the synthesis, modification and properties of cerium oxide nanoparticles (CNPs), a versatile material used in wide range of applications from catalysis to glass polishing, for their potential use in biomedical applications as a function of medium. The thesis starts by projecting the effect of environment on the properties of nanomaterials wherein it is shown that simple medium, such as, water can influence the optical properties of nanoparticles. It was shown that the strong polarizing effect of water on the non-bonding *f* electrons can cause a blue shift in the optical properties of CNPs as a function of increase in trivalent oxidation state of cerium in CNPs. This phenomenon, contradictory to existing literature in solid state where a red shift is observed upon increasing the trivalent oxidation state of cerium in CNPs, is purely attributed to the medium-inflicted change in properties of nanoparticles. This concept is built upon in the first half of thesis by increasing the colloidal stability of nanoparticles by surface and/or medium modification. It is shown that the narrow range of pH in which the colloidal CNPs are stable can be extended by changing the medium from water to polyhydroxy compounds such as glucose and dextran. The synthesis was designed specially to avoid the traditional precipitation and re-dispersion strategy of synthesis of

nanoparticles to preserve the surface activity. The complex forming ability of cerium with polysaccharides was employed to synthesize the CNPs in a one step process and the pH stability of the NPs was extended between 2.0 to 9.5. The difference in the complexing ability of the monomer - glucose and its anhydro glucose polymer - dextran is reflected in the ability of cerium to form super-agglomerates with the monomer while anhydro gluco polymer forms extremely disperse 3-5 nm nanoparticles through steric modification. It is shown that the antioxidant activity of nanoparticles remain unchanged by surface modification by demonstrating the cycling of the oxidation state of cerium in CNPs, with time, through hydrogen peroxide mediated transition of oxidation states of cerium.

It is demonstrated that the polymeric coatings, generally considered as passive surface coatings, can also play an active role in tuning the properties of nanomaterials and increasing their biocompatibility as well as bio-catalytic activity. It is demonstrated that the antioxidant activity of CNPs can be increased as a function of polyethylene glycol (PEG) while the biocompatibility is unaltered due to the biocompatible nature of PEG. The antioxidant activity of CNPs involves an electron transfer (ET) from the CNPs to the reactive oxygen species or vice versa. This heterogeneous ET system is further complicated by the presence of surface adsorbed species. Interfacial charge/electron transfer (ET) between a particle and adsorbed (or covalently bonded) molecule presents significant complexity as it involves a solid state electron transfer over long distance. Unlike a free ion, in solid state, the conducting electrons can be temporarily trapped by the coupling lattice sites. Adsorption/attachment of surface species to nanoparticle can disturb the electronic levels by further polarizing the electron cloud thereby localizing the electron and facilitating the charge transfer. Such an interfacial electron transfer between NPs and adsorbed organic species can be compared to the single electron transfer carried by organometallic

systems with a metal ion core modified with electron delocalizing porphyrin ligands. It is demonstrated that in this PEGyltaed CNPs system, the PEG essentially forms a complex with CNPs in the presence of hydrogen peroxide to facilitate this electron transfer process. The superoxide dismutase (SOD) and catalase mimetic ability of CNPs is described and special emphasis is given to its biocompatibility.

The second half of the thesis emphasizes the role of synthesis and surface modification in influencing the catalytic performance of cerium oxide modified titanium dioxide catalysts for decomposition of methanol. Noble metals supported on oxide nanoparticles have been an area of active research in catalysis. It is demonstrated that the modification of surface of the oxide nanoparticles by noble metals is a function of the synthesis process. By keeping the size of the nanoparticles constant, it was demonstrated that the differences in the oxidation state of noble metals can lead to change in the activity of noble metals. This contribution adds to the already existing controversy in the open literature about the role of the oxidation state of platinum in catalysis. The core level shifts in the binding energy of the *4f* electrons of platinum was used as a guide to the gauge the oxidation state. Results from an in-house built catalytic reactor coupled to mass spectrometer and in-situ diffuse reflectance infra-red spectroscopy are used to quantify the catalytic performance and identify the mechanism of reaction as well as products of methanol decomposition.

ACKNOWLEDGEMENTS

I would like to take this opportunity and express my sincere thanks to all the people who have helped me to reach this stage of my academic career and complete my doctoral thesis. The contributions, intellectual or moral, from everyone has transformed into achieving a doctoral degree from the University of Central Florida. I would like to start by thanking the School of Graduate Studies and the Advanced Materials Processing and Analysis Centre for providing me with an opportunity to pursue my doctoral studies at the UCF. I am thankful to the funding support in the form of prestigious Presidential Doctoral Fellowship from UCF which laid a very strong foundation and raised the level of expectation from a doctoral candidate. I greatly acknowledge the guidance, support (financial and moral), exposure and experience gained from my advisor Prof. Sudipta Seal. It has been a wonderful and memorable experience from the very first day I had started my graduate studies at UCF because of the valuable leadership and guidance of Prof Seal. The opportunities received by working with Prof Seal have allowed me to improve my competency in academics, oral presentation, and scholarly writing and communication skills at all levels. At this moment I would also like to thank the members of my thesis committee (Dr. Clovis Linkous, Dr. Helge Heinrich, Dr. Diego Diaz and Prof. Hyoung-Jin Cho) for their constant support, motivation and guidance and being patient with the limitations of a graduate student. In addition, I would like to thank Prof. T.R. Rama Mohan (IIT Bombay) who have constantly motivated me during my masters to pursue a doctoral degree and have recommended me to work with Prof. Seal. At this point it is also appropriate to acknowledge the support received from Dr. Debasis Bera and especially Dr. Satyanarayana (Satya) VNT Kuchibhatla who have helped to make a smooth transition from Prof. Mohan's lab to Prof Seal's lab. I would especially like to acknowledge Satya with whom I started the work on nanocerium oxide which has translated into a part of the thesis. Our ever confusing and often argumentative

discussions, along with inputs from Prof. Seal, have translated into research work which have been recognized by the scientific community and excelled the work done at Prof. Seal's laboratory.

At Prof. Seal's lab I had the opportunity to interact and work with several eminent scientists and their exceptional students, an experience, which have inspired and motivated me to reach this stage. I would like to express my sincere thanks to Prof Larry Hench (Imperial College, UK), Prof Dean Sayle (Defense academy of Sciences, UK), Prof. Jochen Schneider (Aachen University, Germany), Dr. William Self, Dr. Sanjay Singh, Eric Heckert and Janet Dowding (Burnett School of Biomedical Sciences, University of Central Florida), Prof. Artëm Masunov and Dr. Talgat Inerbaev (Nanoscience Technology Center, University of Central Florida), Dr. Christopher Reilly and Suzanne Hirst (VA-MD Regional College of Veterinary Medicine, Virginia Polytechnic Institute), Prof. (Physiology, Virginia College of Osteopathic Medicine), Dr. Daryl Bourdeaux and Dr. Bhabendra Pradhan (Nanoholdings LLC), Dr. Julian Jones and Dr. Olga Tsigkou (Imperial College, UK), Prof. Peter Brenneisen (Heinrich Heine University, Germany), Dr. Helge Heinrich (Department of Physics, University of Central Florida) , Dr. Deigo Diaz, Nathan Greenletch and Jordan Spence (Department of Chemistry, University of Central Florida). I am especially thankful to Prof. Seal for presenting a unique opportunity to train and work with Dr. Don Baer, Dr. Theva Thevuthasan, Dr. Nachimuthu Ponnuswamy and Dr. Shutta Shuttanandan at Environmental and Molecular Sciences Laboratory (Pacific Northwest National Laboratory). Working with these people I have realized the importance of research in fundamental science and have helped me to obtain in depth understanding of our work on nanocerium oxide.

I would also like to thank the American Vacuum Society for honoring me with the AVS top level award for portions of my doctoral work. I also thank the AVS Florida Chapter which has honored the work done under my supervision by Jessica King. I greatly acknowledge the travel support from the graduate studies at the University of Central Florida. I would also like to thank the travel fellowship from NSF IREE for travel to Germany to learn and train with eminent researchers.

I would like to express my sincere thanks to all the members of Surface Engineering and Nanotechnology Facility, "***Our Lab***". The world is a merrier place with friends and family and everyone at our lab makes the experience richer and fuller for pursuing meaningful research. I would like to thank my seniors Dr. Debasis Bera, Dr. Satyanarayana VNT Kuchibhatla, Dr. Swanand Patil, Dr. Sameer Deshpande, Rudy Filmalter, and Erik Brinley for their guidance, work and support during the initial stages of my doctoral studies. I have been fortunate to train and work with my current lab members Dr. Suresh Krishna, Dr. Michael Murray, Amit Kumar, David Reid, Dr. Abhilash Vincent, Dr. Soumen Das, Virendra Singh and Jessica King. I would also like to thank all the current and past members of the lab who have worked with me on various aspects of my research including the REU students (Amit Kumar, Maura Malinska, Divya Bernard, Ranjith Thanneeru, Jessica King, Linda Nguyen, Saritha Samudralaya). I wish all of them good wishes in all their future personal and professional endeavors. I would like to thank everyone (Karen Glidewell, Cynthia Harle, Angelina Feliciano, Judith Ramos, Kari Stiles, Waheeda Illasaire) at the AMPAC and MCF office who have helped us throughout in administrative matters and made the time spent at the University of Central Florida shorter than what it appears. I would especially like to thanks Karen Glidewell for her constant moral

support, words of encouragement and patiently listening to our complaints that used to sort out on their own. Her charismatic presence had made this place much closer to home.

At the end I would like to thank the most important people in my life without whom this journey and this accomplishment would not have been possible and without whom achieving this milestone would be meaningless. I would like to express my sincere admiration and absolute gratitude to my beloved wife, Saroj Karakoti, for her support, encouragement, patience and love that has made this academic career a wonderful trip. Her constant support, motivation and personal sacrifices have helped me to achieve this academic milestone in life. I would like thank my beloved parents for their constant support during my entire educational career. I thank them for standing behind me in tough times and for being a part of my academic career. I greatly acknowledge the support from my sister Anuradha Bora as it was only because of her support that I could gather the strength to come this far for higher education. Her constant and unconditional support to my family, back home has kept the pressure off of me and helped me to concentrate on my studies and achieve this milestone. I would also like to thank my dear friend Nirmal Singh Bisht for his constant admiration, encouragement and guidance that have helped me to overcome major hurdles in my life.

I believe that everyone in my family and friends have contributed to this degree and this degree reflects the achievement of a family and a community and I would like to thank God “The Almighty” for blessing us with opportunity and giving us the strength, courage and determination to achieve all personal and professional milestones in life.

TABLE OF CONTENTS

LIST OF FIGURES

LIST OF TABLES

LIST OF SCHEMES

1 INTRODUCTION

1.1 Organization of the dissertation

The central theme underlying this dissertation discusses the role of synthesis in tuning the surface characteristics of oxide based nanomaterials to change their physico-chemical properties thereby extending their use in various catalytic applications including biochemical catalysis. In essence the thesis reflects that the properties of nanomaterials are a function of their surface and how these can be tuned to obtain desired properties. Major emphasis of this thesis is focused on the properties of cerium oxide nanomaterials for biomedical applications and additional work is being described on mixed cerium oxide – titanium oxide nanoparticles for decomposition of methanol as a source of hydrogen.

The thesis is divided into 5 chapters including introduction covering two different segments of catalytic applications. All the chapters reflect different manuscripts written by the author that are either accepted or submitted to peer reviewed journals. Additional details, wherever necessary, are thus provided as supplementary information and presented at the end of the thesis as an appendix.

Properties of nanomaterials are a function of their surface and thus the environment which is in direct contact with the surface plays a crucial role in modifying its properties. This important aspect is exemplified in second chapter and discusses the water induced blue shift in the band gap of cerium oxide nanoparticles. It is widely accepted in literature that the band gap of cerium oxide nanoparticles shows a red shift as a function of increase in Ce^{3+} concentration. Oxygen vacancies (defects) can be stabilized by increasing the concentration of Ce^{3+} in the fluorite lattice of cerium oxide. Most of the experimental data reported in the literature are based on dry powders and/or thin films grown and measured in ultra high vacuum conditions. In contrast when the nanoparticles are suspended in water, the optical spectra showed a blue shift induced

by the polarizing effect of the water on the non-bonding electrons of cerium oxide. A comparison of both experimental and theoretical data with the values reported in the literature is discussed in this chapter. In addition to the optical properties, the role of environmental parameters in changing the physical characteristics of cerium oxide nanoparticles is presented in Appendix – A. This appendix discusses the self assembly behavior of cerium oxide nanoparticles in water at room temperature, refrigerated conditions and in freezing conditions. It was observed that while the self assembly at room temperature leads to the formation of superoctahedral structures, the self assembly in ice leads to the formation of ceria nanorods guided by the micro and nanochannels in the ice.

The third chapter in the thesis discusses the synthesis of cerium oxide nanoparticles in polyhydroxyl medium. Our lab has demonstrated the antioxidant properties of cerium oxide nanoparticles and has shown these nanoparticles to be non-toxic to the cells. While the nanoparticles by themselves are non–toxic, synthesis of nanoparticles using methods such as reverse microemulsion involve the synthesis of these nanoparticles in toluene, a very toxic material. Owing to the high surface adsorption tendency of nanoparticles, removal of surfactants and toluene from the surface is a very challenging and involved process. Thus there was an imminent need to develop alternate synthesis methods in more biocompatible and less aggressive environment. The synthesis of nanoparticles in purely aqueous environment limited their stability to a narrow range of pH between 2.0 and 5.0. It is known that the stability of nanoparticles can be increased by steric or electrostatic stabilization. Such procedures usually require precipitation and re-dispersion of nanoparticles for enhancing their stability. Based on our experience that the precipitation and re-dispersion of cerium oxide nanoparticles reduces their biological activity, the cerium oxide nanoparticles were synthesized directly in polyhydroxyl medium such as glucose

and dextran (M.W – 1000 daltons). It was found that the stability of the nanoparticles synthesized in glucose and dextran could be extended from pH 2.0 to 9.5 and that the complexation of cerium ions with the polyhydroxyl group facilitates the direct synthesis of nanoparticles during its oxidation. It was found that cerium oxide nanoparticles form super-agglomerates in a glucose medium while the same was not evident in dextran, a polymer of glucose. The role of available hydroxyl groups in determining the size, shape and stability of cerium oxide nanoparticles is discussed in this chapter and the work was published in the Journal of Physical Chemistry C. The application of nanoparticles synthesized in dextran is discussed in appendix B and C. Appendix B shows the applicability of dextran coated nanoparticles in reducing the tumor stroma interaction and was presented as a poster in the conference on Basic Frontiers in Cancer research in Oct 2009. This work in collaboration with Germany is currently being written as a manuscript. To confirm the presence of dextran coated nanoparticles in the cells an additional chemical procedure was done to attach a fluorescent dye to the dextran attached to the surface. Important highlights from this work, along with the procedure to attach fluorescent tags to the dextran coated nanoparticles are presented as appendix B. Some of the important differences between the nanoparticles synthesized in acidic and alkaline media in terms of their reactivity are presented in appendix C. The effect of cerium oxide nanoparticles (coated and uncoated with dextran) in increasing the proliferation of collagen produced in porous 3-D bioactive glass scaffolds in discussed in appendix C. This manuscript is currently submitted.

The stabilization of nanoparticles discussed in Chapter 3 is described as passive stabilization, as they do not affect the catalytic antioxidant behavior of cerium oxide nanoparticles. In fact it has been shown that the catalytic activity of nanoparticles decreases with increase in the coating thickness and/or the solution polymer concentration. It was shown previously that the catalytic

activity of cerium oxide nanoparticles is a function of Ce^{3+} concentration. Through specific experiments we could show that the antioxidant properties of cerium oxide nanoparticles stems from its ability to scavenge superoxide and peroxide radicals. While Ce^{3+} is extremely effective in scavenging superoxide radicals, it has very poor peroxide scavenging activity. On the other hand, Ce^{4+} is much more efficient in scavenging hydrogen peroxide. It is shown in chapter 4 how the peroxide scavenging activity of cerium oxide nanoparticles with predominant Ce^{3+} oxidation state can be increased by changing the medium from aqueous to polyethylene glycol. It is shown that PEGylated nanoceria particles are efficient superoxide as well as peroxide radical scavengers. The role of concentration of PEG in tuning the activity as well as regeneration of cerium oxide nanoparticles through the formation of complexes and the biocompatibility of such nanoparticles is discussed. This work was published in Journal of the American Chemical Society.

Chapter 5 demonstrates the role of surface modification of mixed oxide catalysts in thermal catalysis of methanol to hydrogen. It discusses the importance of synthesis in changing the oxidation state of Pt coated on the surface of ceria-titania mixed oxide in optimizing its catalytic behavior for thermal decomposition of methanol. Metal-decorated over reducible and non-reducible metal oxides are used in catalysis for decomposition of organic compounds and catalyzing several important reactions. The synergistic effects of support oxides and noble metals have been debated for a long time now in improving the catalytic efficiency. One of the open debates in the literature discusses the role of oxidation state of platinum in its catalytic efficiency. The major barrier to this effect has been the synthesis of similarly sized Pt nanoparticles over a same support with different stable oxidation states. In this chapter the author synthesized Pt coated nanoparticles using two different synthesis procedures and have shown

that the while the size of nanoparticles is nearly constant in each procedure, the reduction environment chosen to coat mixed oxide nanoparticles has a profound effect on the oxidation state of platinum. An in-house built catalytic reactor was used to test the thermal decomposition of methanol. It was shown that platinum in an oxidized state is more active in decomposition of methanol at a rate as high as 3.5 mmol of MeOH/min/g of the catalyst while the catalyst with higher concentration of platinum in metallic state was less active. The oxidized form also lead to a decrease in the poisoning of the catalyst during the decomposition of methanol. The effect of synthesis conditions on changing the surface oxidation state, shape and activity of platinum is compared and discussed.

List of all publications authored or co-authored by the author of the thesis is presented as appendix D. A scope of things to come is also listed under the title "manuscript submitted" while the work under progress is listed as the manuscript under preparation. The copyrights forms for published manuscripts reproduced in this thesis are listed in appendix E.

An introduction of each chapter is provided separately at the beginning of each chapter; however, to make the choice of cerium oxide nanoparticles as a case study for demonstrating the biomedical applications of ceria is provided in chapter one. This chapter covers the basic characteristics of cerium oxide nanoparticles and provides an overview of its antioxidant properties and behavior. This chapter is submitted as a review article to the Chemical Society Reviews.

1.2 History of cerium oxide in biological applications

Cerium compounds have been used traditionally as drug components in both water soluble (nitrates, acetates and chlorides) and insoluble (oxalate) form[1] and the first few publications on the use of cerium as drugs dates back to 1850. Cerium compounds are known as

antiemetic, bacteriostatic, bactericidal, immuno-modulating and antitumour agents[1, 2]. In fact, trivalent cerium ions are used for treatment of burn victims to reduce infection, treat burn sepsis and reduce inflammatory response. Cerium chloride was shown to possess antitumor properties by inhibiting the proliferation of gastric cancer cells and leukemia cells[2]. Cerium compounds have also found usage in agriculture and as a nutrient in fodder. Cerium nitrate pretreatment was shown to increase the germination in rice by increasing the SOD, catalase and peroxidase activity and decreasing the concentration of superoxide and malonaldehyde[3]. Similarly it was shown the supplementing the fodder with lanthanides increased the daily weight gain and food assimilation in cattle[4]. Lanthanides were shown to be non toxic in animals and the accumulation in the vital organs was minimal[5, 6]. It was shown by Heckert et al[7] that Ce^{3+} ions could potentially be harmful and can catalyze Fenton like reactions in cells. Oxide nanoparticles which do not release free cerium ions but behave as ions ions may act as good catalysts yet remain relatively benign to cells. In this respect, a well dispersed 3-5 nm CNPs can be described as soluble ceria having ion like properties in an oxide lattice. Specific examples of the use of cerium oxide nanoparticles for protection against oxidant injury from the current literature are listed in table 1.

Table 1-A: Antioxidant properties of CNPs in various model systems

Synthesis and Size	Type of Study	Cell Line	Dosage	Results	Ref
Microemulsion stripped off surfactant (3-5nm)	Radiation damage to normal cells in radiation therapy for cancer treatment	CRL8798 (normal) and MCF-7 (tumor) cells	0-5 μM nanoceria 10 Gy radiation dose	CNPs protect the radiation induced damage. Protection conferred only to normal cells and not to tumor cells.	8
Water based direct synthesis in solution (3-5nm w/agglomerates of 15-20nm)	Macular degeneration induced by ROI using light induced model	Albino mice and photoreceptor cells	10nM – 1000 nM 3800 lux of white light	Complete protection of photoreceptor cells upon 24 hrs pretreatment with CNPs. Post injury protection conferred to decrease further damage	9
6 nm and 12 nm by precipitation	Neuroprotection using cell viability and oxidative stress	HT-22 and RAW 164		CNPs are neuroprotective and the protection is independent of particle size in the study range	10
Water based nanoceria (3-5nm) varying Ce3+/Ce4+ ratio	SOD mimetic activity	Competitive inhibition of reduction of ferricytochrome C by superoxide anion	N/A	CNPs with higher Ce3+ ratio are found to be SOD mimetic	11
Microemulsion stripped off surfactant (3-5nm)	Peroxide injury model to spinal cord neurons	Adult spinal cord neuron cells	10nM	Neuroprotective effect of CNPS demonstrated through electrophysiological data and prevention from hydrogen peroxide mediated injury to spinal cord neurons	12

Synthesis and Size	Type of Study	Cell Line	Dosage	Results	Ref
Sol gel nanoceria (7-10 nm)	Myocardial histology, nitrotyrosine formation, expression of cytokines, and ER stress	MCP-1 transgenic mice and wild type mice	15 nM 2X/week for 2 weeks	CNPs show protection against ROS-induced cardiac dysfunction, reduces the expression of pro-inflammatory cytokines and reduces ER stress	13
Dextran-coated nanoceria	Peroxide injury model	MCF-7 and CRL-7303 cell line		pH-dependent protection offered by dextran coated CNPs. Only protection at near neutral pH and no protection at acidic pH values	14
Water based direct synthesis in solution (3-5nm in agglomerates of 15-20nm)	Inflammation protection and	J774 Macrophages	10 nM to 10 μM	CNPs reduces the inflammation by scavenging ROI and reducing the expression of pro-inflammatory enzymes such as i-NOS and Cox-2	15
High temperature (8nm, cubic)	Oxidative stress measurement using MTS assay and ROS generation using abiotic and biotic conditions	Raw 267.4 and BEAS-2B cell line		CNP exposure did not result in oxidative stress. Cellular internalization of CNPs without any structural changes in mitochondria through membrane lined vesicles	16

Synthesis and Size	Type of Study	Cell Line	Dosage	Results	Ref
Precipitation and calcination at 800 (6-16nm)	Alzheimer's model	SH-SY5Y neuroblastoma cells	100 µM	CNPs instigate the neuronal survival through signaling pathways such as ERK1,2, ERK5 and BDNF. Protection by the CNPs points towards their function as modulator of pathways crucial for neuronal survival	17
Microemulsion stripped off surfactant (3-5 nm)	Radiation induced Pneumonitis	CCL 135 and in vivo (athymic nude mice)	0.0017µg/mL in vitro and 0-135 mg/kg in vivo	CNPs are well tolerated and protect from radiation induced cell death and pneumonitis. CNPs were shown to provide better protection than amifostine the only acceptable and currently available drug	18
Dextran coated CNPs (5,12 14 and 100 nm)	Oxidase like property at acidic pH	N/A	N/A	Dextran coated polymers can oxidize various biologically relevant molecules at acidic pH without the use of hydrogen peroxide. Conjugation of CNPs with organic targeting ligands can be used as detection tool in immunoassays	19
PAA stabilized and citrate stabilized water soluble CNPs(1-2nm)	Antioxidant property of nanoparticles to prevent oxidation of anthocyanins by peroxides	N/A	N/A	CNPs protect anthocyanins (bioflavonoids) from oxidation by hydrogen peroxide. The antioxidant activity of CNPs exceeds that of polyphenols.	20

Synthesis and Size	Type of Study	Cell Line	Dosage	Results	Ref
CNPs synthesized directly in PEG (3-5 nm in agglomerate of 15-20nm).	Superoxide and hydrogen peroxide scavenging	HaCat (keratinocyte) cell line	0 – 500 µM	CNPs as well as PEGylated CNPs were biocompatible upto 500uM concentration. CNPs in very high concentration (80%) show slight decrease in cell viability at incubation time ≥ 48 hrs. Superoxide scavenging was unaffected by PEG concentration	21

1.3 Antioxidant behavior of CNPs

Among various catalytic applications shown by the CNPs, one of the most interesting properties which was discovered by our group is the catalytic reaction with superoxide (O_2^-)[11, 22]. We are currently investigating whether these nanoparticles can also react with peroxides and reactive nitrogen species such as nitric oxide radical or peroxynitrite. The rationale for such studies lies in the knowledge that other SOD mimetics are capable of catalytic removal of hydrogen peroxide or peroxynitrite[23]. The catalytic removal of superoxide and potentially other ROS and RNS species is likely the molecular mechanism behind the 'antioxidant' properties that these nanoparticles have exhibited in several cell culture and animal studies. We will briefly review this work, followed by an analysis of how the chemistry of cerium oxide and its synthesis relate to the catalysis in biologically relevant conditions.

Radiation therapy, one of the most accepted methods for treatment of cancer, is not selective and causes equivalent damage to both cancerous and normal cells. Ionizing radiation produces a cascade of free radicals that damages the normal cells in the close proximity of tumor cells. In controlled experiments CNPs were shown to protect primary cells against radiation-induced damage (0 – 10 Gy dose range) while not signficantly altering death of tumor cells[8]. Differences in the inter and intracellular pH between the normal and the tumor cells were attributed to possible reasons for differential efficacy of CNPs in protecting normal cells as compared to tumor cells. In a more recent study CNPs were shown to protect against radiation induced pneumonitis using both in vitro and in vivo models[18]. Nanoceria not only prevented the radiation induced damage but also outperformed the currently accepted and widely used drug amifostine for prevention of radiation-induced damage. Although the mechanism of protection is lacking, these exciting results require further

studies to determine the nature of catalytic activity exhibited by CNPs which imparts differential protection of terminally differentiated 'normal' cells versus cancer cells.

In another study, CNPs (10 nM to 1000 nM concentration) protected against light-induced injury in a retinal neuronal culture model, and preserved visual function of the retina in an animal model[9]. Protection by CNPs occurred across the entire retina and was not limited to the area of injection of the nanoparticles. Post treatment with CNPs in a sensitized cell also protected cells from further damage induced by a cascade of ROS.

This initial animal study ignited the research in our group to understand the mechanism of action of these nanoparticles. After an initial screen to determine whether CNPs were potent scavengers of several ROS and RNS, we found that CNPs exhibited potent SOD mimetic activity[11] in an initial report. It was subsequently shown that CNPs with higher Ce^{3+}/Ce^{4+} ratio (likely due to oxygen vacancies at the surface) displayed a higher SOD activity than the ones with lower Ce^{3+}/Ce^{4+} ratio[24]. It was further shown by changing the Ce^{3+}/Ce^{4+} ratio that the SOD activity decreases with oxidation of CNPs (by high levels of H_2O_2) and the scavenging activity returns upon reduction of the particles in solution. Using combined UV-VIS and EPR analysis, the specificity of CNPs to react with superoxide radicals was also shown[24]. Our group is currently testing the hypothesis that these nanoparticles will indeed behave similar to a class of manganese porphyrins that are well described as SOD mimetics[23].

Oxidative stress and generation of free radicals are also associated with several neurodegenerative diseases such as trauma, aging, Alzheimer's and Parkinson's disease. The ability of CNPs to prevent oxidative stress induced damage was extended to the neuronal cells and it was shown that a single dose of CNPs could trigger the survival of brain cell

neurons against peroxide mediated injury[12]. Schubert et al[10] reported protection from exogenous oxidants in a neuronal cell line (HT22) in the presence of cerium oxide and yttrium oxide nanoparticles (another rare earth oxide material). We have not been able to observe any catalytic activity in yttrium oxide nanoparticles in vitro, so the mechanism by which these particles protected these cells is still speculative and may depend on how the materials are made in the laboratories. Recently, D'Angelo et al[17] showed ability of CNPs to trigger neuronal survival (neuroblastoma SH-SY5Y cell ine) in a human Alzheimer disease model. It was suggested in this study that CNPs (calcined preparation) not only act as antioxidants but also affect signal transduction pathways involved in the neuroprotection. Perhaps the most interesting feature of this work was the protection offered by CNPs calcined at 800^{o}C which shows that even after high temperature treatment the activity of the nanoparticles was not lost. These results suggests that CNPs can also affect the expression of proteins in a mammalian cell, although we have not observed signficant changes in CNP treated cultures (data not shown).

Both reactive oxygen and nitrogen species play a critical role in development of cardiovascular diseases. Using a transgenic mouse model expressing monocyte chemoattractant protein-1 (MCP-1), CNPs were shown to protect against inflammation induced by high levels of this cytokine, and the protection reduced biomarkers of ROS and RNS[25]. It was shown that redox sensitive transcription of pro inflammatory factors such as Tumor necrosis factor-α, Interleukin-6, MCP-1 and Interleukin-8 were significantly suppressed by injection of the animals with CNPs. CNPs also supressed endoplasmic reticulum (ER) stress and reduced the apoptic cell death in the myocardium. This was the first study to show that CNPs could protect against vascular injury related to ROS from the

pro-inflammatory response. Taken together with results in neurodegenerative and cancer models, there is good evidence that CNPs protect against oxidant injury through their ability to scavenge superoxide, similar to the mechanism of protection afforded by fullerenes.

1.4 Oxygen vacancies and defect engineering of CNPs - role in catalysis

Cerium oxide (ceria) is one of the most versatile rare earth oxide materials. Cerium is a rare earth metal of the lanthanide series and exists in two different oxidation states 3+ and 4+ which differ from the occupation of one electron in the 4f orbital. Due to the its two different stable oxidation states, ceria can exist in two forms of oxides as Ce_2O_3 ((sesquioxide) having a hexagonal lattice [26] and CeO_2 with a cubic fluorite lattice structure. The lattice oxygen in cerium oxide is considered to be highly mobile over a wide range of working temperatures. High oxygen mobility imparts several important properties to nanoceria such as (i) oxygen storage and release (ii) promoting noble metal activity and dispersion for application in catalysis[27] (iii) stabilization of chemically active Ce^{3+} oxidation state (iv) reduction in band gap and solar cells[28]. All the properties mentioned above are governed by the ease of creation, availability at the surface/subsurface and distribution of the oxygen vacancies. In case of ceria, creation of an oxygen vacancy by removing a neutral oxygen atom leads to localization of two electrons over 4f states[29, 30]. Such a localization results in reduction of two coordinated cerium cations (from Ce^{4+} to Ce^{3+}) per oxygen and if there is a cluster of vacancy formed on the surface it can lead to the formation of a hot spot having a cluster of Ce^{3+} ions while the cerium ions adjacent to these trivalent ions still maintain their tetravalent character[30]. Thus the creation of oxygen vacancies stabilizes the thermodynamically instable Ce^{3+} in cerium oxide.

It was shown that the oxygen vacancies could originate on the surface or subsurface and could act as catalytically active hot spots[29]. Recent observations through scanning tunneling

microscopy (STM) have shown these surface and subsurface single vacancies and their clusters as dimers or trimers however, theoretical work [31] show that the formation of diads and triads of vacancies as an energetically uphill task. A more important observation from the point of view of biological applications of nanoceria is the defect structure and ease of formation of vacancies in aqueous solution[32]. Adsorption of water molecule on the surface reduces the energy of formation of vacancy by a significant margin[33]. Such an observation thus emphasizes the synthesis of highly pure CNPs directly in water without the need for precipitation and re-dispersion techniques. While most of the theoretical models seem to agree with the relative ease of adsorption of water (0.25 to 1 monolayer [ML]) on reduced ceria surfaces, theory seems to disagree about the role of water in reduction or oxidation of cerium oxide at the nanoscale regime. It is hypothesized that there is slight possibility of oxidation of water molecules on the surface of ceria and the results seems to agree, at least qualitatively, with the simulations from Watkins et al[34] and Chen et al[35] while other literature seems to disagree with this observation on stoichiometric ceria surfaces[32]. This observation is in stark contrast to the experimental observation where water does not seem to oxidize the reduced ceria surface[36]. In a more detailed investigation it was reported that the presence of water molecules on stoichiometric ceria surface may increase the number of vacancies on ceria (111) surface[32]. Thus the aqueous media around cerium oxide nanoparticles may favor the surface reduction and retention of Ce^{3+} oxidation state.

1.5 Oxidation state and formation of oxygen vacancies as a function of size and dopants

Creation and mobility of oxygen vacancies on cerium oxide at elevated temperatures is well documented. Several properties including catalytic activity, corrosion prevention and oxygen storage capacity (OSC) of cerium oxide was explained in terms of creation of vacancies and subsequent reduction of cerium from Ce^{4+} to Ce^{3+} oxidation state at elevated temperatures[37,

[38]. The oxygen nonstiochiometry at elevated temperatures can be retained upon fast quenching of particles. To a similar extent the doping of various trivalent lanthanides has also been investigated with the purpose of creating oxygen vacancies and/or subsequent reduction of cerium. Various lanthanides such as lanthanum, samarium, gadolinium and yttrium have been used as dopants in cerium oxide and investigated for various applications[39]. Doping of lower valence cations in cerium matrix results in the creation of oxygen vacancies (and reduction of Ce^{4+} to Ce^{3+} maintain the charge neutrality in the system) and forms solid solution with the dopant element of the form $Ce_{1-x}R_xO_{2-y}$ (where R refers to the dopant rare earth metal, X refers to the lattice site and V refers to the vacancy)[40]. It goes without saying that the lattice structure should not be modified by doping and the doping element should replace cerium substitutionally rather than interstitially. The formation of oxygen vacancies can be represented in Kroger Vink Notation as:

$$2Ce^{x}_{Ce} + O^{x}_{O} = 2Ce^{`}_{ce} + V^{**}_{O} + \tfrac{1}{2}\, O_2(g) \qquad (1)$$

Thus replacement of two cerium tetravalent ions with two trivalent rare earth ions results in oxygen nonstoichiometry with formation of one oxygen vacancies and reduction of two cerium atoms adjacent to the oxygen vacancy to maintain charge neutrality in the system.

Reducing the size of the particles to the nano regime introduces oxygen non stoichiometry in the oxide systems including cerium oxide. . The oxygen nonstoichiometry increases with decrease in particle size and it was shown by Deshpande et al[41] using rigorous X-ray Photoelectron Spectroscopy (XPS) measurements . The dependence of oxidation state on the size of nanoparticles is not linear and the values in literature differ with variation is the synthesis procedures and inability to produce and demonstrate conclusively a monodisperse

size of nanoparticles free from adsorbed impurity (Table 2). Reducing the size of the nanoparticles down to nano regime increases the percentage of surface atoms thereby increasing the number of unsatisfied and uncoordinated atoms/bonds. Such thermodynamic instability can be accompanied creation of oxygen vacancies and charge redistribution causing the reduction of surface cerium atoms to Ce^{3+} while the atoms in the core remain Ce^{4+}. Such a core shell structure for CNPs was demonstrated using Electron Energy Loss Spectroscopy (EELS) wherein the surface concentration of Ce^{3+} varied significantly from the bulk as the particle size decreased below 15 nm. The authors predicted a fully reduced CNPs at 3-5 nm particle size)[42].

Table 1-B: Size dependent changes in concentration of trivalent cerium in CNPs

Particle Size (nm)	**Ce^{3+} concentration**	**Synthesis**	**Quantification Methodology**	**Ref**
23-28	15.6	Thin Films	XPS	43
3	44	Microemulsion	XPS	41
6	29	Water based		
30	17	Thermal		
3	18	Templated on Silica aerogel	Electron Magnetic Resonance (EMR)	44
6	35.6	Wet chemical and precipitation	XPS	45
10	24.2			
5000	12.5			
4	6		X-ray Absorption Near Edge Spectroscopy (XANES) (subtraction method)	45
10	1			
		Wet chemical and precipitation		

Particle Size (nm)	Ce^{3+} concentration	Synthesis	Quantification Methodology	Ref
7	21	Size fractionation after emulsion synthesis	Lattice expansion model	46
4.6	38			
2.6	74			

1.6 Potential mechanisms of antioxidant properties

The mechanism of antioxidant action of CNPs and the ability to regenerate and cycle between the trivalent and tetravalent oxidation state in biological environment is relatively uknown. The chemical and physical aspects in reaction of cerium oxide with ROS and its regeneration have to be addressed in more detail before coming to conclusive mechanism. As explained earlier the only definitive mechanism known so far is the clear scavenging of superoxide, and this property correlates with a higher content of Ce^{3+} oxidation state in the material. It was reported recently that CNPs do not show antioxidant property at acidic pH[14, 20]. A review of literature on cerium chemistry could explain some of the redox reactions of cerium ions with hydrogen peroxide. The perplexing chemistry of cerium with hydrogen peroxide in highly acidic medium was identified as early as 1951[47]. Several publications then identified the course of mechanism through the reversible reaction of cerium with hydrogen peroxide (equation 2, 3, 4) at highly acidic pH[48-51].

$$Ce^{4+} + H_2O_2 \rightarrow Ce^{3+} + HOO^- + H^+ \quad (2)$$

$$Ce^{4+} + HOO^- \rightarrow Ce^{3+} + H^+ + O_2 \quad (3)$$

$$Ce^{3+} + HO_2 + H^+ \rightarrow Ce^{4+} + H_2O_2 \quad (4)$$

All these reactions were studied at highly acidic pH values of 1.5 or below. Attempts were made to determine the rate of forward (K_1) and backward (K_{-1}) reactions and it was suggested that K_1 and K_{-1} could compete with each other and thus can not only scavenge hydrogen peroxide but may also lead to formation of hydrogen peroxide at acidic pH[52]. Thus it seems reasonable to argue that at acidic pH at some relative concentration of Ce^{3+}/Ce^{4+} the scavenging action of cerium towards H_2O_2 may not be kinetically favorable. It must be noted that most of the reactions listed above were observed with cerium ions while we are comparing the mechanism for nanoparticles being a solid heterogenous phase. Thus there exists two different complexities in deciphering the mechanism of action of CNPs 1) CNPs are present as heterogenous particles (not ions) and must react slowly (as compared to other surrounding being diffusion limited) with homogenously present free radicals 2) The physiolgical pH is different than the commonly documented reactions and mechanism for reaction of cerium ions with hydrogen peroxide. The most plausible rationale for the reaction of nanoparticles as a heterogenous phase with homogenously distributed free radicals could be argued if we consider ultra small nanoparticles of the order of few nano meters. In such a case the physical boundary between the particles and clusters of ions could be diminishing and one can assume the CNPs to be present in the form of soluble ceria. Thus the reaction between soluble nanoparticles and soluble free radicals will no longer be diffusion limited.

1.7 Presence of ionic species

Some insights into the reaction of CNPs at a range of pH and its inability to protect cells at slightly acidic pH could be gained from the modified pourbaix diagram of the system Ce(III/IV)-H_2O-H_2O_2/O_2 systems developed by Yu et al[53]. These diagrams which were developed for understanding the cerium based conversion coatings serve as perfect example how interdisciplinary nature of science can help the scientists to understand and unravel

perplexing phenomenon through mingling of unrelated fields. It was established that at reduced pH (<1.0) Ce^{4+} could be reduced to Ce^{3+} by H_2O_2 while at pH values between 1.0 – 4.0 Ce^{3+} will be oxidized to Ce^{4+} by H_2O_2 depending upon the concentration of H_2O_2. An important finding from this study was the fact that the final species formed from the oxidaiton of Ce^{3+} may not be just CeO_2 but several intermediate species may form such as $Ce(OH)^{3+}$, $Ce(OH)_2^{2+}$, and $Ce(OH)_4$. Considering that in the case of CNPs there are no free Ce^{3+} ions makes the situation diffcult to reconcile[53, 54]. Nonetheless it suggests that the redox conditions under mild to severely acidic pH may form different surface species on CNPs that may induce potential toxicity to cells which could be misinterpreted as pH-dependent antioxidant activity. It is clear that a better understanding of the catalytic nature of CNPs in biologically relevant conditions is needed.

1.8 Regeneration via complexation.

The complexation of cerium with hydrogen peroxide has been used previously to detect the presence of intracellular H_2O_2. It was shown that ceruim ions, administered in the form of free cerium chloride, form an electron dense complex (cerium monoperoxy hydroxide – $Ce(OH)_2(OOH)$ that can react with hydrogen peroxide and could be detected by transmission electron microscopy[55]. Recently, this complex has been a focus of numerous studies in the area of material science and Scholes et al[56, 57] could show that the oxidation of Ce (III) to Ce(IV) upon reaction with hydrogen peroxide occurs through formation of an intermediate compound cerium oxy peroxo complex $CeO_2(OH)_2$. In contrast, Djuricic et al[58] described this compound as $Ce(OH)_{4-x}(OOH)_x$ based on thermogravimetric analysis. Even though both studies started with cerium ions and report the formation of a complex after addition of hydrogen peroxide to cerium ions, we have observed the formation of this compound upon addition of hydrogen peroxide to grounded cerium oxide nanoparticles (below 20 nm) and an

aqueous suspension of CNPs. Further evidence on the tendency of CNPs to form peroxo type complexes was reported by Guzman et al[59]. Thus the formation of peroxo complex is a natural tendency of cerium whether present as an ion or nano oxide. How this unstable peroxo complex decomposes determines the final oxidation state of CNPs. Scholes et al[56] described that the peroxo complex forms in alkaline medium and decomposes in air as

$$Ce(III) + H_2O_2 + 2OH^- \rightarrow CeO_2(OH)_2 + 2H^+ \quad (5)$$

$$CeO_2(OH)_2 \rightarrow CeO_2 + 1/2O_2 + H_2O \quad (6)$$

Such decomposition of peroxo complex in air was reported to occur over a period of several months. The decomposition of such complex may occur through different mechanism in water and we have observed that in contrast to equation 6, CNPs are regenerated with higher Ce^{3+} oxidation state rather than stoichiometric ceria as suggested. The role of water and surrounding pH is critical to this observation and is currently under investigation.

1.9 Role of vacancies and defects in scavenging ROS

As stated earlier, ceria is a versatile redox catalyst used for several different applications such as combustion of organics, car exhaust gas cleaning, water gas shift (WGS), carbon monoxide preferential oxidation (PROX), intermediate temperature solid oxide fuel cells or sulfur removal in FCC units. The release of lattice oxygen reduces the cerium from Ce^{4+} to Ce^{3+} with oxidation of adsorbed species on the surface. During the process of re-oxidation 4 electrons are transferred from neighbouring Ce^{3+} to the incoming oxygen molecule (O_2) to produce two oxygen anion O_2^- in the lattice. Reactive oxygen intermediates such as superoxide and peroxide have been identified on the surface of CNPs using electron paramagnetic resonance and vibrational spectroscopy. For example, spectroscopic evidence for the presence of peroxide species was reported during the oxidation of CO to carbon

dioxide[59]. However these studies and many similar reports are carried out at high temperatures and thus direct analogy to a biological aqueous reaction is tenuous. However, the atomistic simulation of electron transfer from Ce^{3+} to the adsorbed oxygen, superoxide and peroxide species could serve as good starting point for developing theoretical understanding of the reaction mechanism. The combination of studies to determine the catalytic reactions of CNPs in aqueous solution with this literature can give a clearer picture of the reactivity of CNPs in the coming years.

1.10 Recent studies highlighting bioavailability.

Thus far the focus of research has centered on exploring the use of CNPs as antioxidants in different models that are affected and/or controlled by ROS. Current gaps exist in our understanding of how these particles work in culture and animal models. Two critical areas include the biodistribution and bioavailability of CNPs in cells, tissues and animals and theoretical modeling and catalytic properties of CNPs with ROS and RNS in an aqueous environment. In one of our recent studies we have shown that CNPs can be tailored to have both SOD mimetic and catalase mimetic properties by synthesizing NPs directly in polyethylene glycol[60]. It was hypothesized that CNPs form a charge transfer (CT) complex with PEG in presence of hydrogen peroxide and the regeneration of the trivalent oxidation state of CNPs is a function of decomposition of this CT complex. The pH dependent oxidase like property of CNPs by coating the NPs with dextran and poly acrylic acid (PAA) is documented[19, 61,47]. It was shown that the organic coating can interfere with the activity of NPs and thus with the use of thinner coatings the authors could demonstrate CNPs as a tool for developing immunoassays under acidic conditions. The oxidation state of cerium in CNPs was not discussed in these reactions and it seems that for demonstrating oxidase like activity the NPs should have higher tetravalent oxidation state in acidic environment. In terms of

drug delivery Mallik et al[62] have demonstrated the use of CNPs as a drug delivery medium for treatment of glaucoma by attaching the human carbonic anhydrase II (hCAII) inhibitor to nanoceria. The choice of CNPs as the delivery medium arises from the two different properties a) excellent diffusion and b) the ability of CNPs to protect the retina from oxidative stress. Biodistribution is largely unstudied, yet one study showed that a single tail vein injection of mice resulted in the detection of electron dense precipitates in various organs of the body[15]. More importantly the histological examination of stained thin sections of major organs post 7 days of injection (liver, spleen, brain, kidney and pancreas) were free from any lesions and did not show any significant differences as compared to the control mice. The distribution and rate of removal of these nanoparticles from these organs is currently under investigation to determine the pharmacological profile and potential toxicity of CNPs.

1.11 Toxicity of CNPs

In contrast to numerous studies on toxicity of fullerenes, relatively few have dealt with toxicity of rare earth oxides. Specifically only cerium oxide nanoparticles have been studied, yet as in the case of fullerenes, results are conflicting between these reports. This is likely due to differences in the procedures used to synthesize these nanoparticles, leading to changes in particle structure and surface chemistry. Nonetheless we will consider the results from each study, and discuss our unpublished findings as well.

Lin et al. first analyzed the toxicity of cerium oxide nanoparticles (20 nm in diameter) produced by a supercritical synthesis in BEAS-2B cells (lung) in 2006[73]. They found increases in reactive oxygen species, decreases in glutathione levels and increases in malondialdehydes. The range of concentrations used in this study was from 3.5 to 23.3 μg/mL, and this represents concentrations in the 20-150 micromolar range (with respect to

cerium concentration). A second study by the same group analyzed similar endpoints in the same culture model system, this time altering average particle size from 15 nm to 45 nm[74]. Again, an increase in oxidative stress was observed, this time monitoring changes in gene expression. The range of concentrations in the second study was from 30-250 micromolar. A more recent paper by the same group built upon previous studies show that several major regulatory pathways were stimulated including p38 MAP kinase, nuclear factor-kappaβ (NF-kappaβ) and nuclear factor-E2-related factor-2 (Nrf-2). Nrf-2 is well known to be a global responder to oxidative injury. Thus it is clear that this preparation of cerium oxide leads to toxicity in this cell line.

Using the same culture model, Nel and his colleagues compared the toxicity of ZnO and CeO_2 nanoparticles[16]. While ZnO exposure elicited an oxidative stress response, cerium nanoparticles did not. Moreover CNPs protected cells against oxidative injury. This study is in stark contrast to those discussed above. It should be noted that in both studies the subcellular localization of CNPs was tested and these particles were found to be largely perinuclear[16, 74]. A more recent risk analysis of the safety of CNPs as a fuel additive also suggests there is little toxicity of these materials, and a similar finding that CNPs are not genotoxic[75, 76].

Although our group has not focused on toxicity of these materials, we have tested CNPs in various culture models in concentrations ranging from low nano-molar to low milli-molar levels (with respect to cerium). We have shown that these particles are not toxic at nano-molar to micro-molar levels in several publications [21, 22, 77]. At high micro-molar to milli-molar ranges (750 μM – 1 mM) we do see toxicity in many cell types such as A549, HaCat, and HUVECs (data not shown). This is based on assessment by either tetrazolium dye reduction (MTT) or

release of lactate dehydrogenase (LDH). These levels are extremely high, and it is likely that CNPs are toxic due to their bulk interference in redox-dependent biological processes given the nature of the surface chemistry, or perhaps due to one-electron reduction of oxygen to form superoxide. We cannot however resolve the differences in toxicity of wet chemical synthesis (our preparations) and supercritical synthesis procedures of the Park group [73, 74, 78]. We suspect either changes in surface chemistry or the cell-nanoparticle interactions are quite different, as it is clear that their preparations are characterized with hard, angular edges [73, 74]. However it is clear that a comprehensive animal toxicological profile (absorption, distribution, metabolism, and excretion or ADME) is needed to better understand the toxicology and the potential benefit of CNPs in biology.

1.12 References

[1] M. A. Jakupec, P. Unfried, B. K. Keppler, in *Reviews of Physiology Biochemistry and Pharmacology, Vol. 153*, **2005**, pp. 101.

[2] Y. J. Ji, B. Xiao, Z. H. Wang, M. Z. Cui, Y. Y. Lu, *Biomedical and Environmental Sciences* **2000**, *13*, 287.

[3] H. Fashui, *Biological Trace Element Research* **2002**, *87*, 191.

[4] S. Schuller, C. Borger, M. L. He, R. Henkelmann, A. Jadamus, O. Simon, W. A. Rambeck, *Berliner Und Munchener Tierarztliche Wochenschrift* **2002**, *115*, 16.

[5] M. L. He, D. Ranz, W. A. Rambeck, *Journal of Animal Physiology and Animal Nutrition* **2001**, *85*, 263.

[6] M. L. He, Y. Z. Wang, Z. R. Xu, M. L. Chen, W. A. Rambeck, *Journal of Animal Physiology and Animal Nutrition* **2003**, *87*, 229.

[7] E. G. Heckert, S. Seal, W. T. Self, *Environmental Science & Technology* **2008**, *42*, 5014.

[8] R. W. Tarnuzzer, J. Colon, S. Patil, S. Seal, *Nano Letters* **2005**, *5*, 2573.

[9] J. Chen, S. Patil, S. Seal, J. F. McGinnis, *Nat Nano* **2006**, *1*, 142.

[10] D. Schubert, R. Dargusch, J. Raitano, S. W. Chan, *Biochemical and Biophysical Research Communications* **2006**, *342*, 86.

[11] C. Korsvik, S. Patil, S. Seal, W. T. Self, *Chem Commun (Camb)* **2007**, 1056.

[12] M. Das, S. Patil, N. Bhargava, J. F. Kang, L. M. Riedel, S. Seal, J. J. Hickman, *Biomaterials* **2007**, *28*, 1918.

[13] J. Niu, A. Azfer, L. M. Rogers, X. Wang, P. E. Kolattukudy, *Cardiovasc Res* **2007**, *73*, 549.

[14] J. M. Perez, A. Asati, S. Nath, C. Kaittanis, *Small* **2008**, *4*, 552.

[15] S. M. Hirst, A. S. Karakoti, R. D. Tyler, N. Sriranganathan, S. Seal, C. M. Reilly, *Small* **2009**, *9999*, NA.

[16] T. Xia, M. Kovochich, M. Liong, L. Madler, B. Gilbert, H. Shi, J. I. Yeh, J. I. Zink, A. E. Nel, *ACS Nano* **2008**, *2*, 2121.

[17] B. D'Angelo, S. Santucci, E. Benedetti, S. Di Loreto, R. A. Phani, S. Falone, F. Amicarelli, M. P. Ceru, A. Cimini, *Current Nanoscience* **2009**, *5*, 167.

[18] J. Colon, L. Herrera, J. Smith, S. Patil, C. Komanski, P. Kupelian, S. Seal, D. W. Jenkins, C. H. Baker, *Nanomedicine-Nanotechnology Biology and Medicine* **2009**, *5*, 225.

[19] A. Asati, S. Santra, C. Kaittanis, S. Nath, J. M. Perez, *Angewandte Chemie-International Edition* **2009**, *48*, 2308.

[20] V. K. Ivanov, A. V. Usatenko, A. B. Shcherbakov, *Russian Journal of Inorganic Chemistry* **2009**, *54*, 1522.

[21] A. S. Karakoti, S. Singh, A. Kumar, M. Malinska, S. V. Kuchibhatla, K. Wozniak, W. T. Self, S. Seal, *J Am Chem Soc* **2009**, *131*, 14144.

[22] E. G. Heckert, A. S. Karakoti, S. Seal, W. T. Self, *Biomaterials* **2008**, *29*, 2705.

[23] M. A. Sharpe, R. Ollosson, V. C. Stewart, J. B. Clark, *Biochem J* **2002**, *366*, 97.

[24] E. G. Heckert, A. S. Karakoti, S. Seal, W. T. Self, *Biomaterials* **2008**, *29*, 2705.

[25] J. Niu, A. Azfer, L. M. Rogers, X. Wang, P. E. Kolattukudy, *Cardiovasc Res* **2007**, *73*, 549.

[26] H. Barnighausen, G. Schiller, *Journal of the Less-Common Metals* **1985**, *110*, 385.

[27] Q. Fu, H. Saltsburg, M. Flytzani-Stephanopoulos, *Science* **2003**, *301*, 935.

[28] A. Corma, P. Atienzar, H. Garcia, J. Y. Chane-Ching, *Nature Materials* **2004**, *3*, 394.

[29] C. T. Campbell, C. H. F. Peden, *Science* **2005**, *309*, 713.

[30] F. Esch, S. Fabris, L. Zhou, T. Montini, C. Africh, P. Fornasiero, G. Comelli, R. Rosei, *Science* **2005**, *309*, 752.

[31] J. C. Conesa, *Catalysis Today* **2009**, *143*, 315.

[32] M. Fronzi, S. Piccinin, B. Delley, E. Traversa, C. Stampfl, *Physical Chemistry Chemical Physics* **2009**, *11*, 9188.

[33] S. Kumar, P. K. Schelling, *The Journal of Chemical Physics* **2006**, *125*, 204704.

[34] M. B. Watkins, A. S. Foster, A. L. Shluger, *Journal of Physical Chemistry C* **2007**, *111*, 15337.

[35] H. T. Chen, Y. M. Choi, M. L. Liu, M. C. Lin, *Chemphyschem* **2007**, *8*, 849.

[36] M. A. Henderson, C. L. Perkins, M. H. Engelhard, S. Thevuthasan, C. H. F. Peden, *Surface Science* **2003**, *526*, 1.

[37] M. V. Ganduglia-Pirovano, A. Hofmann, J. Sauer, *Surface Science Reports* **2007**, *62*, 219.

[38] J. A. Kilner, *Chemistry Letters* **2008**, *37*, 1012.

[39] C. G. Feng, G. D. Fan, *Journal of Rare Earths* **2005**, *23*, 309.

[40] S. Babu, R. Thanneeru, T. Inerbaev, R. Day, A. E. Masunov, A. Schulte, S. Seal, *Nanotechnology* **2009**, *20*.

[41] S. Deshpande, S. Patil, S. Kuchibhatla, S. Seal, *Applied Physics Letters* **2005**, *87*.

[42] L. J. Wu, H. J. Wiesmann, A. R. Moodenbaugh, R. F. Klie, Y. M. Zhu, D. O. Welch, M. Suenaga, *Physical Review B* **2004**, *69*.

[43] P. Patsalas, S. Logothetidis, L. Sygellou, S. Kennou, *Physical Review B* **2003**, *68*.

[44] P. Dutta, S. Pal, M. S. Seehra, Y. Shi, E. M. Eyring, R. D. Ernst, *Chemistry of*

Materials **2006**, *18*, 5144.

[45] N. Kohler, G. E. Fryxell, M. Q. Zhang, *Journal of the American Chemical Society* **2004**, *126*, 7206.

[46] S. Tsunekawa, R. Sivamohan, S. Ito, A. Kasuya, T. Fukuda, *Nanostructured Materials* **1999**, *11*, 141.

[47] A. Medalia, B. Byrne, *Anal. Chem.* **1951**, *23*, 453.

[48] P. B. Sigler, B. J. Masters, *Journal of the American Chemical Society* **2002**, *79*, 6353.

[49] G. Czapski, B. H. J. Bielski, N. Sutin, *J. Phys. Chem.* **1963**, *67*, 201.

[50] W. F. Libby, *J. Phys. Chem.* **1952**, *56*, 863.

[51] B. H. J. Bielski, E. Saito, *The Journal of Physical Chemistry* **2002**, *66*, 2266.

[52] P. B. Sigler, B. J. Masters, *J. Am. Chem. Soc.* **1957**, *79*, 6353.

[53] P. Yu, S. A. Hayes, T. J. O'Keefe, M. J. O'Keefe, J. O. Stoffer, *Journal of the Electrochemical Society* **2006**, *153*, C74.

[54] S. A. Hayes, P. Yu, T. J. O'Keefe, M. J. O'Keefe, J. O. Stoffer, *Journal of the Electrochemical Society* **2002**, *149*, C623.

[55] R. Gossrau, C. J. F. Vannoorden, W. M. Frederiks, *Histochemistry* **1989**, *92*, 349.

[56] F. H. Scholes, A. E. Hughes, S. G. Hardin, P. Lynch, P. R. Miller, *Chemistry of Materials* **2007**, *19*, 2321.

[57] F. H. Scholes, C. Soste, A. E. Hughes, S. G. Hardin, P. R. Curtis, *Applied Surface Science* **2006**, *253*, 1770.

[58] B. Djuricic, S. Pickering, *Journal of the European Ceramic Society* **1999**, *19*, 1925.

[59] J. Guzman, S. Carrettin, A. Corma, *Journal of the American Chemical Society* **2005**, *127*, 3286.

[60] A. S. Karakoti, S. Singh, A. Kumar, M. Malinska, S. Kuchibhatla, K. Wozniak, W. T. Self, S. Seal, *Journal of the American Chemical Society* **2009**, *131*, 14144.

[61] A. Asati, S. Santra, C. Kaittanis, S. Nath, J. M. Perez, *Angew Chem Int Ed Engl* **2009**, *48*, 2308.

[62] S. Patil, S. Reshetnikov, M. K. Haldar, S. Seal, S. Mallik, *Journal of Physical Chemistry C* **2007**, *111*, 8437.

[63] N. Lewinski, V. Colvin, R. Drezek, *Small* **2008**, *4*, 26.

[64] G. Oberdorster, E. Oberdorster, J. Oberdorster, *Environmental Health Perspectives* **2005**, *113*, 823

[65] N. Sera, H. Tokiwa, N. Miyata, *Carcinogenesis* **1996**, *17*, 2163.

[66] J. P. Kamat, T. P. A. Devasagayam, K. I. Priyadarsini, H. Mohan, J. P. Mittal, *Chemico-Biological Interactions* **1998**, *114*, 145.

[67] X. L. Yang, C. H. Fan, H. S. Zhu, *Toxicology in Vitro* **2002**, *16*, 41.

[68] E. Oberdorster, *Environmental Health Perspectives* **2004**, *112*, 1058.

[69] C. M. Sayes, A. A. Marchione, K. L. Reed, D. B. Warheit, *Nano Letters* **2007**, *7*, 2399.

[70] A. Isakovic, Z. Markovic, B. Todorovic-Markovic, N. Nikolic, S. Vranjes-Djuric, M. Mirkovic, M. Dramicanin, L. Harhaji, N. Raicevic, Z. Nikolic, V. Trajkovic, *Toxicol. Sci.* **2006**, *91*, 173.

[71] C. M. Sayes, J. D. Fortner, W. Guo, D. Lyon, A. M. Boyd, K. D. Ausman, Y. J. Tao, B. Sitharaman, L. J. Wilson, J. B. Hughes, J. L. West, V. L. Colvin, *Nano Letters* **2004**, *4*, 1881

[72] M. S. Hull, A. J. Kennedy, J. A. Steevens, A. J. Bednar, C. A. Weiss, Jr., P. J.

Vikesland, *Environ Sci Technol* **2009**, *43*, 4169.

[73] W. Lin, Y. W. Huang, X. D. Zhou, Y. Ma, *Int J Toxicol* **2006**, *25*, 451.

[74] E. J. Park, J. Choi, Y. K. Park, K. Park, *Toxicology* **2008**, *245*, 90.

[75] B. Park, K. Donaldson, R. Duffin, L. Tran, F. Kelly, I. Mudway, J. P. Morin, R. Guest, P. Jenkinson, Z. Samaras, M. Giannouli, H. Kouridis, P. Martin, *Inhal Toxicol* **2008**, *20*, 547.

[76] B. K. Pierscionek, Y. Li, A. A. Yasseen, L. M. Colhoun, R. A. Schachar, W. Chen, *Nanotechnology*, *21*, 035102.

[77] A. Vincent, S. Babu, E. Heckert, J. Dowding, S. M. Hirst, T. M. Inerbaev, W. T. Self, C. M. Reilly, A. E. Masunov, T. S. Rahman, S. Seal, *ACS Nano* **2009**, *3*, 1203.

[78] H. J. Eom, J. Choi, *Toxicol Lett* **2009**, *187*, 77.

2 WATER INDUCED BLUE SHIFT IN CERIUM OXIDE NANOPARTICLES

2.1 Introduction

In present communication we report the possible origin of blue shift in water suspended nanoceria particles and its dependence on concentration of Ce^{3+} using both experimental and computational results at constant particle size. Ceria (cerium oxide) is one of the most abundant rare-earth metal oxides. It attracts the interest of researchers due to its particularly high performance in a variety of applications such as catalysis, fuel cells and biomedical applications, especially in nanocrystalline form[1-4]. Bulk cerium oxide has at least two stable stoichiometries: the cubic fluorite-type dioxide (CeO_2) *Fm3m*[5] and the hexagonal cerium sesquioxide (Ce_2O_3) *P-3m*[6]. Close thermodynamic stability of these stoichiometries leads to continuous range of partially reduced (also called "mixed valence") CeO_{2-x} phases, where oxygen vacancy can be rapidly formed or eliminated[1]. As a result of this "oxygen storage capacity", ceria is used in number of catalytic processes, most notably for purification of exhaust gases in three-way automotive catalytic converters[2,3]. It was shown that concentration of Ce^{3+} in nanoceria also critically influences its optical properties[7-15]. Several studies have been reported on optical properties of nanocrystalline thin films[7-11] and solvent suspended ceria nanocrystallites[12-15]. For both systems direct and indirect optical electronic transitions are associated with O2*p*→Ce5*d* and O2*p*→Ce4*f* electronic excitations. In the case of nanostructured ceria thin films red shift for both direct and indirect bands was observed experimentally with decrease in nanoparticles' size[7-9]. In contrast, shift to higher energy in absorption spectra with decrease in nanocrystalline size, was observed in toluene and aqueous sols of ceria nanoparticles [12-17]. Different theories attributed this blue shift to the change in valence state Ce ions[8,9,12-15,18] or the quantum confinement effect[19,20] and the role of suspending media and its dependence on concentration of Ce^{3+} has been neglected to a large extent.

2.2 Results and discussion:

In current experiments we used ceria nanoparticles of 3-5 nm in diameter synthesized by wet chemical procedure described elsewhere[21]. The values of direct and indirect optical band gaps were measured using the conventional method[22]. Results presented in Fig. 1a, along with various reported values in literature, show a blue shift with increase in concentration of Ce^{3+}. Further confirmation of the oxidation state of cerium was obtained from x-ray photoelectron spectroscopy which demonstrated that cerium was predominantly present in Ce^{4+} oxidation state upon oxidation by H_2O_2, while aging in acidic solution reduced cerium to the trivalent oxidation state (Ce^{3+}) as shown in Fig. 2a. The exact origin of this reduction upon aging in water/H_2O_2 is not clear at present. The individual particle size of the 3-5nm was confirmed for both oxidized and reduced surface by transmission electron microscopy as observed in Fig. 2b and 2c. Summarizing, the experimental observations reveal the blue-shift in optical transitions with increase in [Ce^{3+}] in the nanoparticles. An opposite trend as compared to the previously reported experimental data[9] (a red shift in the indirect optical transitions with increase in concentration of Ce^{3+}) could be explained if the solvent effect is taken into account. Strong polarizing effect of aqueous environment results in a blue shift in optical transitions of cerium oxide nanoparticles with increase in concentration of Ce^{3+}.

The selection of representative nanoparticle structure is critical for the reliability of the prediction. The smallest possible nanoparticle with octahedral shape was constructed by cutting off (111) planes from the bulk fluorite CeO_2 lattice. These nanoparticles with chemical formula $Ce_{19}O_{32}$ and $Ce_{44}O_{80}$ are presented in Fig. 1b and are in accordance with the experimental findings[23,24-26]. Ceria nanoparticles at the size range considered are inherently non-stoichiometric

and thus we used octahedral non-stoichiometric nanoparticles instead of introducing oxygen vacancies in the most stable stoichiometric ceria nanoparticles[27,28].

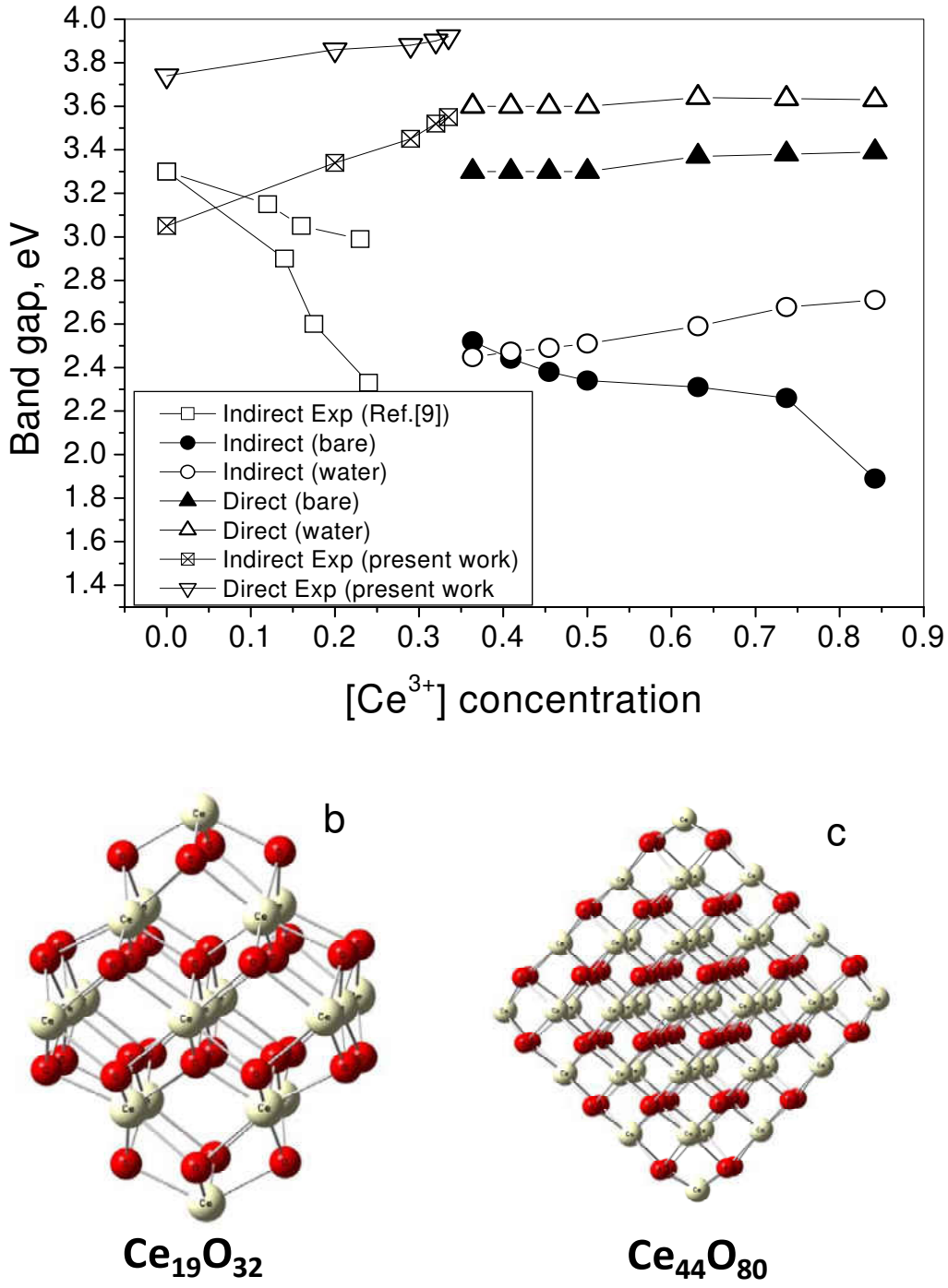

Figure 2-1: (a) Theoretically calculated direct and indirect optical band gaps for bare and water covered $Ce_{19}O_{32}$-n and $Ce_{44}O_{80}$-n NPs in comparison with corresponding experimental values measured in aqueous solution (present work) and literature available results for nanocrystalline ceria film prepared in ultrahigh vacuum chamber. 9 (b) Theoretically investigated octahedral

ceria nanoparticles which are cut by (111) planes from the bulk CeO_2 to form the non-stoichiometric particles.

To investigate the effect of water on electronic properties of nanoceria we considered ceria nanoparticles with 12 and 24 water molecules adsorbed on the surface (for $Ce_{19}O_{32}$ and $Ce_{44}O_{80}$ models, respectively) to provide 1 ML (monolayer) of the surface coverage. Effect of the other molecules or ions in bulk liquid water was neglected. Adsorbed water forms two hydrogen bonds with the oxygen atoms on the surface of the nanoparticle in a configuration similar to the one reported by Fronzi et al[29]. Binding energy between ceria nanoparticles and H_2O was calculated to be 0.54 eV per adsorbed water molecule, in close agreement with the previous DFT studies [7,11,29].

We compared the calculated PDOS of ceria nanoparticles with PDOS for bulk CeO_2 and Ce_2O_3 (not shownf [30]). The calculated values of E_{in} for indirect O2*p*→Ce4*f* and E_d for direct Ce4*d*→Ce4*f* electronic transitions are c.a. 2.38 eV each for bulk CeO_2. The corresponding experimental values for electronic transitions to the localized 4f states within the band gap are equal to 3.3 and 3.6 eV respectively[10]. The theoretical values of optical band gap for bulk ceria are underestimated even at DFT+*U* theory level, and can be overcome only by using hybrid DFT approach[30,31]. The direct band gap of bulk ceria on the other hand corresponding to the O2*p*-Ce5*d* transition has an experimental value of 6 eV[32] which is in close agreement with our calculated value of E_d = 5.33 eV. In the case of Ce_2O_3 the band gap of 2.4 eV was reported and associated with intra-atomic Ce4*f*→Ce5*d* transition[33].

Comparing PDOS for both modifications of bulk ceria with corresponding values for the model ceria nanoparticles (Fig. 3), one can observe that electronic properties of nanoceria are qualitatively closer to Ce_2O_3 rather than to CeO_2. For the model ceria nanoparticles the calculated values for indirect (O2*p*-Ce4*f*) and direct (O2*p*-Ce5*d*) transitions are equal to 2.31 eV and 3.37 eV for $Ce_{19}O_{32}$, 2.52 eV and 3.3 eV for $Ce_{44}O_{80}$ respectively. Calculated location of

indirect band is found to be approximately 0.8 – 1 eV below the direct band. This is in a good agreement with experimental observations, which report the indirect band located c.a. 0.5 eV below the direct one[7,9]. Calculated trends in the optical band gaps for $Ce_{19}O_{32}$ and $Ce_{44}O_{80}$ agree with dependence of the band gap on Ce^{3+}/Ce^{4+} ratio observed in nanostructured ceria films[9]. The small discrepancy arises from the size of theoretical model of nanoceria which is significantly smaller than the experimentally obtained nanoparticles.

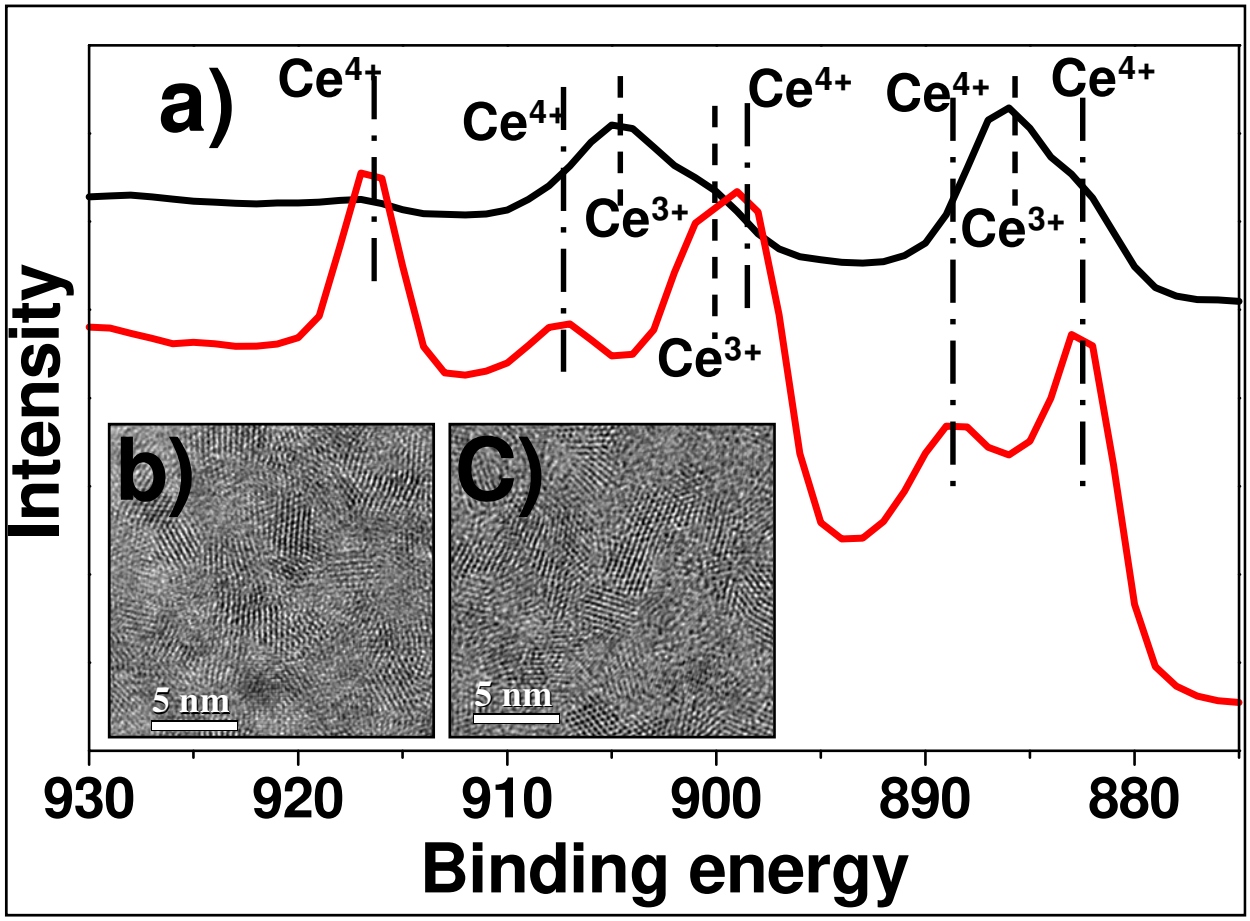

Figure 2-2 a) XPS spectra depicting the predominant oxidation states of cerium oxide nanoparticles upon treatment with hydrogen peroxide (oxidized (Ce^{4+})– peaks at 882.3, 888.1, 898.0, 906.8 and 916.7 eV) and upon aging in aqueous acidic medium (reduced (Ce^{3+}) – peaks at 885.1, 899.5 and 903.5 eV). HRTEM images depicting that the particles size remains unchanged (3-5nm) in b) oxidized and c) reduced cerium oxide nanoparticles and thus the changes in the band gap can be ascribed only to the oxidation state of nanoparticles. The peaks between 875 and 895 eV belong to the Ce $3d_{5/2}$ while peaks between 895–910 eV correspond to the Ce $3d_{3/2}$ levels. The peak at ~916 eV is a characteristic satellite peak for Ce^{4+} oxidation state

We further investigated the optical band gap dependence on the Ce^{3+}/Ce^{4+} ratio, considering nanoceria of fixed size with varying number of oxygen vacancies. Results of theoretical study are summarized in Fig. 1a and compared with experimental data available from the literature[9], and measurements from the present work.

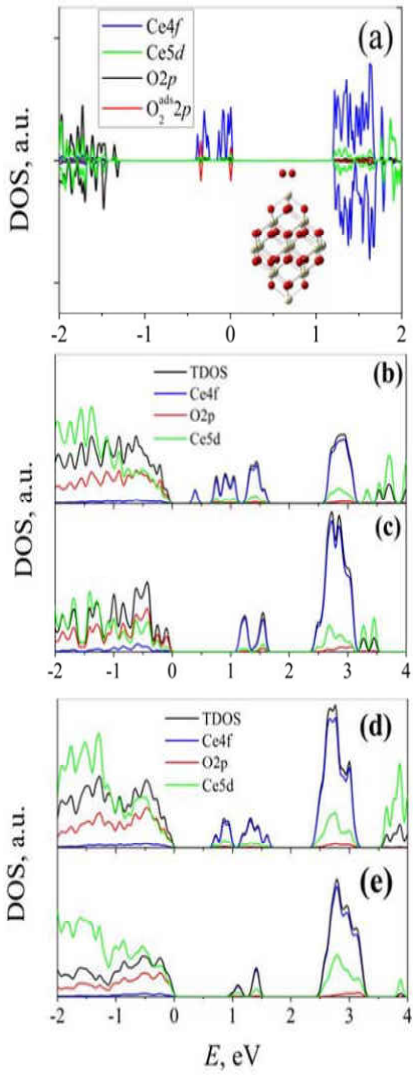

Figure 2-3: Calculated electronic DOS for (a) $Ce_{19}O_{32}$ with adsorbed oxygen molecule; bare (b) $Ce_{19}O_{32}$; (c) $Ce_{44}O_{80}$ nanoparticles; (d) $Ce_{19}O_{32}$-$(H_2O)_{12}$; (e) $Ce_{44}O_{80}$-$(H_2O)_{24}$. Zero level energy is selected to be the top of the occupied O2p band. Projected density of states (PDOS) demonstrate that PDOS of the adsorbed oxygen molecule are similar to the PDOS of bare O_2^{2-} specie (not shown), but differ from PDOS for bare oxygen molecule which has two unpaired

electrons in the ground state. Analysis of the charge and spin distribution in the system reveal the transfer of two electrons from ceria particle to the adsorbed oxygen molecule resulting in oxidation of cerium ion. The adsorption of water molecules leads to splitting of empty f levels giving multiple peaks in indirect optical transition.

Calculated values of optical indirect band gap for both the nanoceria particles ($Ce_{19}O_{32}$ and $Ce_{44}O_{80}$) are smooth functions of [Ce^{3+}] while the values of direct band gap for both bare and water covered nanoceria are nearly independent of [Ce^{3+}]. While E_d values are close for $Ce_{19}O_{32}$ and $Ce_{44}O_{80}$ nanoparticles (they differ by about 0.05 eV), adsorption of the water molecules leads to significant (0.3eV) blue shift in E_d. More quantitative comparison with experimental values is complicated by the fact that only the size dependence of E_d had been reported, without direct measurements of change in [Ce^{3+}] at constant particle size. Current and future experiments from our group are aimed at filling this gap. Both the models of nanoceria demonstrate red-shift in indirect optical band gap with increase in [Ce^{3+}] in the absence of water. The value of E_{in} steadily decreases from 2.52 eV for [Ce^{3+}]=0.36 to 1.89 eV for [Ce^{3+}]=0.84. The slope of E_{in} increases with increase in concentration of Ce^{3+}. The theoretical results for latter case are in good qualitative agreement with experimental measurements performed on nanostructured ceria thin films[7,9]. In contrast, the presence of water increases the value of E_{in} observed by both computational modeling and experimental measurements as a function of concentration of Ce^{3+}. Theoretically obtained increase in E_{in} in the considered range of concentration of Ce^{3+} is c.a. 0.2 eV, nearly twice less than experimentally observed variation in E_{in}. This difference in values could arise from the different range of Ce^{3+}/Ce^{4+} ratio under investigation.

2.3 Summary

Both values of optical band gaps for direct and indirect transitions depend on the aqueous environment. Polarization by the water molecules leads to significant blue shift in E_d that is independent of concentration of Ce^{3+} or number of *f*-electrons. This independence is expected

from O2*p*→Ce5*d* electronic transition. Energy of *d*-levels is independent of *f*-electrons, and in turn E_d is independent of concentration of Ce^{3+}. In contrast, value of E_{in} depends on structure of *f*-band and is sensitive to the amount of *f*-electrons in the system. For bare nanoceria particles increase in concentration of *f*-electrons (due to increase in concentration of Ce^{3+}) leads to energy downshift of the *f*-band. This stabilization of the energy level with increase of its occupation number is typical for vacant orbitals. On the other hand, adsorbed water molecules destabilize *f*-band due to increase in the number of electrons occupying this band. This can be attributed to the ligand field effect, where non-bonding electrons on the metal atom are destabilized by the exchange repulsion with the donor electron pair of the oxygen atom. It can also be noticed from figure 3 that adsorption of water leads to splitting of empty *f*-level. The appearance of multiple peaks in indirect optical transitions also explains the difficulty in determining the dependence of band gap for indirect optical transitions of nanoceria in some of the earlier work[15]. These difficulties are addressed in this work by considering the effect of solvent induced splitting of *f* orbital.

Monotonic dependence of E_{in} on concentration of Ce^{3+} opens the possibility to determine the concentration of oxygen vacancies in ceria nanoparticles with high precision using optical methods. This technique is expected to be much more sensitive and accurate than the methods based on nanoparticle size measurements[20]. Our calculations demonstrate that even though small number of oxygen vacancies does not affect the nanoparticle size, they strongly influence the optical properties. Introduction of vacancies leads to the increase of nanoparticle's "lattice constant", derived from the average Ce-Ce distance ($a_0 = \sqrt{2}\ d_{Ce\text{-}Ce}$). For bare $Ce_{44}O_{80-n}$ ceria nanoparticles, equilibrium values of the lattice parameter are equal to 5.296, 5.298, 5.303, and 5.316 Å for n=0, 1, 2 and 3 respectively. While a_0 remains within ±0.003Å range for n=0, 1, 2,

the E_{in} value undergoes pronounced changes from 2.52 to 2.38 eV. Both these values are in a very good agreement with experimentally reported values[9,20]. For a small variation in [Ce^{3+}] changes in a_0 are almost negligible, whereas changes in E_{in} are substantial. Better, more precise methods or combination of sample characterization have to be employed in order to validate the explanation of blue shift in ceria nanoparticles by quantum confinement effect. Our experimental and theoretical results show that the local environment (such as water) can influence the optical characteristics of the cerium oxide nanoparticles. At this point, authors are convinced that the origin of blue shift in ceria nanoparticles is due to the destabilization effect of water molecules on the *f*-electron states in cerium oxide.

2.4 Materials and methods:

2.4.1 Theoretical simulation

In order to understand the optical properties of ceria nanoparticles, we performed density functional theory (DFT) calculations using plane-wave based Vienna *ab initio* simulation package (VASP 4.8)[34,35]. The electronic ground state was determined using local density (LDA) approximation. We used LDA+*U* version with local part described by Ceperley-Adler function. On site Coulomb and exchange interaction were treated by a single effective parameter U_{eff}=*U*-*J*. Plane waves were included up to an energetic cutoff of 415 eV, electronic wave functions were described using the projected augmented wave (PAW) method and U_{eff}=5 eV[36]. The same protocol was recently employed for investigation of ceria and it was shown that LDA+*U* approximation demonstrates better agreement with experiment for structure properties than generalized gradient approximation (GGA+*U*) approach[37]. The interaction energy between nanoceria and water molecules were estimated using GGA+*U* since this value is overestimated when LDA is used. PW91 exchange-correlation function was employed with U_{eff}=3eV[27,28]. Supercells were chosen with at least 10 Å between replicas to remove periodicity artifacts.

2.4.2 Reversible change in color of CNPs

In order to simulate the reversible color changes in nanoceria treated with hydrogen peroxide, we investigated the electronic structure of $Ce_{19}O_{32}$ with adsorbed O_2 molecule. The most energetically favorable configuration was found to include O_2 molecule attached to nanoceria vertex as shown in inset of Fig.3a.

2.4.3 Transmission electron microscopy

High-resolution transmission electron microscopy (HRTEM) images were obtained using FEI-Tecnai F-30 electron microscope operated at 300KV with a point-to-point resolution of ~0.2nm. The TEM samples were prepared by coating the holey carbon-coated copper grids with few drops of solution. Images were collected from the grids dried overnight in vacuum and non dried grids to remove any artifacts that may arise from drying process. 15-20 nm agglomerates with individual particle size of 3-5 nm were consistently observed in the sample. The individual particle size did not change with aging or drying of nanoparticles.

2.4.4 X-ray photoelectron spectroscopy (XPS)

Qualitative analysis of the oxidation state of cerium in CNPs was gauged from XPS analysis of the samples using PHI ESCA 5400 spectrophotometer operated at 300W at a base pressure of 2 x 10^{-8} torr or less and Al Kα as source of x-rays. The samples for the XPS analysis were prepared in glove box with continuous flow of argon by drop coating a 5mM suspension of CNPs on a silicon wafer. To ensure the uniformity of sample preparation equal amount of sample was dropped on the silicon wafer for coating. The samples were then transferred to a sealed sample transfer chamber inside the glove box for transferring to the XPS chamber without any exposure to ambient atmosphere to avoid any interference of atmosphere with the valence chemistry of cerium. The spectrophotometer was calibrated using a gold standard prior to XPS run and any

charge shift in the samples was corrected using adventitious carbon as a reference at binding energy of 284.8 eV.

2.4.5 UV-Visible spectrophotometry and measurement of concentration of Ce^{3+} oxidation state

The composition of Ce^{3+} was ascertained indirectly by measuring the absorption of Ce^{4+} using UV-Visible spectrophotometer (Lambda 750S). The original concentration of 5mM nanoceria sample was diluted to 0.5 mM to record the changes in absorbance with aging time. The absorption maximum at 298 nm following 1 day of the addition of hydrogen peroxide was assumed to originate from 100% concentration of Ce^{4+} ions. A calibration plot was obtained by measuring the absorbance at 298 nm with serial dilutions. This calibration plot was used to estimate the concentration of cerium +4 oxidation state in nanoceria by measuring the absorbance at 298 nm, after the addition of hydrogen peroxide and aging time.

2.4.6 Synthesis of nanoparticles

Cerium oxide nanoparticles were synthesized using previously published protocols. Cerium nitrate hexahydrate was dissolved in DI water and stirred for 15 – 30 minutes. The solution was filtered using 200 nm filter (ANODISC) to remove any unwanted and undissolved impurities. The solution was then oxidized using excess of oxidizers and the pH of the solution was maintained at 2.5 – 4.0. The solution was then aged at room temperature in acidic medium (pH - 2.5 to 3.5) to catalyze the formation of nanoceria with predominant trivalent oxidation state of cerium.

2.4.7 Oxidation of cerium

For experimental work the concentration of cerium in its reduced state in nanoceria particles suspended in water was controlled chemically by oxidizing Ce^{3+} to Ce^{4+} using hydrogen peroxide [38]. The oxidation is accompanied by change in color of the solution from colorless to yellow/orange depending on hydrogen peroxide concentration. It was recently established that

chemical reaction between ceria nanocrystals and hydrogen peroxide results in the formation of the yellow and orange complexes with O_2^{2-} ions[39]. Our computational results show that such coloring of nanoceria-O_2^{2-} complex is caused by electron transfer from O_2^{2-} ions on nanoceria surface to cerium ions. These transitions are distinctly different from the optical properties of nanoceria itself and are not discussed further.

2.5 References

1 Kang, Z.C. & Eyring, L., The structural principles and their consequences for the anion-deficient fluorite-related oxides of the higher rare earths in Oxides (Trans Tech Publications, Clausthal Zellerfe), **155-1,**301-358 (1998).

2 Heinemann, C., Cornehl, H.H., Schroder, D., Dolg, M., & Schwarz, H., The CeO_2^+ cation: Gas-phase reactivity and electronic structure. *Inorganic Chemistry* **35,** 2463-2475 (1996).

3 Seal, S. & Shukla, S., Sol-gel derived oxide and sulfide nanoparticles. in *Functionalization and Surface Treatment of Nanoparticles*, edited by M. Baraton & H.S. Nalwa (Academic Press, San Diego, CA) (2002).

4 Yabe, S. & Sato, T., Cerium oxide for sunscreen cosmetics. *J. Solid St. Chem.* **171,** 7-11, 2003.

5 Duclos, S.J., Vohra, Y.K., Ruoff, A.L., Jayaraman, A., & Espinosa, G.P., High-Pressure X-Ray-Diffraction Study of CeO_2 to 70 Gpa and Pressure-Induced Phase-Transformation from the Fluorite Structure. *Phy. Rev. B* **38,** 7755-7758 (1988).

6 Barnighausen, H. & Schiller, G., The Crystal-Structure of a-Ce_2O_3. *Journal of the Less-Common Metals* **110,** 385-390 (1985).

7 Suzuki, T., Kosacki, I., Petrovsky, V., & Anderson, H.U., Optical properties of undoped and Gd-doped CeO_2 nanocrystalline thin films. *J. App. Phy.,* **91,** 2308-2314 (2002).

8 Patsalas, P., Logothetidis, S., & Metaxa, C., Optical performance of nanocrystalline transparent ceria films. *App. Phy. Lett.,* **81,** 466-468 (2002).

9 Patsalas, P., Logothetidis, S., Sygellou, L., & Kennou, S., Structure-dependent electronic properties of nanocrystalline cerium oxide films. *Phy. Rev. B,* **68,** 035104 (2003).

10 Guo, S., Arwin, H., Jacobsen, S.N., Jarrendahl, K., & Helmersson, U., Spectroscopic ellipsometry study of cerium dioxide thin-films grown on sapphire by RF magnetron sputtering. *J App. Phy.,* **77,** 5369-5376 (1995).

11 Toro, R.G. *et al.*, Relationship between the nanostructures and the optical properties of CeO_2 thin films. *J Phys. Chem. B* **108,** 16357-16364 (2004).

12 Tsunekawa, S., Fukuda, T., & Kasuya, A., X-ray photoelectron spectroscopy of monodisperse CeO_{2-x} nanoparticles. *Surf. Sc.,* **457,** L437-L440 (2000).

13 Tsunekawa, S., Sahara, R., Kawazoe, Y., & Kasuya, A., Origin of the blue shift in ultraviolet absorption spectra of nanocrystalline $CeO_{(2-x)}$ particles. *Mater. Trans. JIM,* **41,** 1104-1107 (2000).

14 Tsunekawa, S., Wang, J.-T., Kawazoe, Y., & Kasuya, A., Blueshifts in the ultraviolet absorption spectra of cerium oxide nanocrystallites. *J. App. Phy.* **94,** 3654-3656 (2003).

15 Tsunekawa, S., Fukuda, T., & Kasuya, A., Blue shift in ultraviolet absorption spectra of monodisperse CeO_{2-x} nanoparticles. *J. App. Phy.,* **87,** 1318-1321 (2000).

16 Masui, T. *et al.*, Characterization of Cerium(IV) oxide ultrafine particles prepared using reversed micelles. *Chem. Mat.* 9 (10), 2197-2204 (1997).

17 Masui, T., Machida, K., Sakata, T., Mori, H., & Adachi, G., Preparation and characterization of cerium oxide ultrafine particles dispersed in polymer thin films. *J. Alloy. Compd.* **256,** 97-101 (1997).

18 Tsunekawa, S., Wang, J.T., Kawazoe, Y., & Kasuya, A., Blueshifts in the ultraviolet absorption spectra of cerium oxide nanocrystallites. *J. App. Phy.,* **94,** 3654-3656 (2003).

19 Nie, J.C., Hua, Z.Y., Dou, R.F., & Tu, Q.Y., Quantum confinement effect in high quality nanostructured CeO[sub 2] thin films. *J App. Phy.* **103,** 054308-054307 (2008).

20 Hernandez-Alonso, M.D. *et al.*, Confinement effects in quasi-stoichiometric CeO_2 nanoparticles. *PCCP* **6,** 3524-3529 (2004).

21 Karakoti, A.S., Kuchibhatla, S., Babu, K.S., & Seal, S., Direct synthesis of nanoceria in aqueous polyhydroxyl solutions. *J Phys. Chem. C* **111,** 17232-17240 (2007).

22 Vanleeuwen, R.A., Hung, C.J., Kammler, D.R., & Switzer, J.A., Optical and electronic transport-properties of electrodeposited thallium(iii) oxide-films. *J. Phys. Chem.* **99,** 15247-15252 (1995).

23 Skorodumova, N.V., Baudin, M., & Hermansson, K., Surface properties of CeO_2 from first principles. *Phys. Rev. B* **69,** 075401-8 (2004).

24 Yang, S.W. & Gao, L., Controlled synthesis and self-assembly of CeO_2 nanocubes. *J. Am. Chem. Soc.* **128,** 9330-9331 (2006).

25 Zhang, J. *et al.*, Colloidal ceria nanocrystals: A tailor-made crystal morphology in supercritical water. *Adv. Mater.* **19**, 203- (2007).

26 Kuchibhatla, S., Karakoti, A.S., Sayle, D.C., Heinrich, H., & Seal, S., Symmetry-driven spontaneous self-assembly of nanoscale ceria building blocks to fractal superoctahedra. *Crystal Growth & Design* **9,** 1614-1620 (2009).

27 Loschen, C., Migani, A., Bromley, S.T., Illas, F., & Neyman, K.M., Density functional studies of model cerium oxide nanoparticles. *PCCP* **10,** 5730-5738 (2008).

28 Loschen, C., Bromley, S.T., Neyman, K.M., & Illas, F., Understanding ceria nanoparticles from first-principles calculations. *J Phys. Chem. C* **111,** 10142-10145 (2007).

29 Fronzi, M., Piccinin, S., Delley, B., Traversa, E., & Stampfl, C., Water adsorption on the stoichiometric and reduced CeO_2(111) surface: a first-principles investigation. *PCCP* **11,** 9188-9199 (2009).

30 Da Silva, J.L.F., Ganduglia-Pirovano, M.V., Sauer, J., Bayer, V., & Kresse, G., Hybrid functionals applied to rare-earth oxides: The example of ceria. *Phys. Rev. B* **75,** 045121–10 (2007).

31 Hay, P.J., Martin, R.L., Uddin, J., & Scuseria, G.E., Theoretical study of CeO_2 and Ce_2O_3 using a screened hybrid density functional. *J Chem. Phys.* **125**, 34712-34718 (2006).

32 Wuilloud, E., Delley, B., Schneider, W.D., & Baer, Y., Spectroscopic Evidence for Localized and Extended f-Symmetry States in CeO_2. *PRL* **53,** 202 (1984).

33 Prokofiev, A.V., Shelykh, A.I., & Melekh, B.T., Periodicity in the band gap variation of Ln(2)X(3) (X=O, S, Se) in the lanthanide series. *J. Alloy. Compd.* **242,** 41-44 (1996).

34 Kresse, G. & Hafner, J., Ab-initio molecular-dynamics for liquid-metals. *Phys. Rev. B* **47,** 558-561 (1993).

35 Kresse, G. & Furthmuller, J., Efficient iterative schemes for ab initio total-energy calculations using a plane-wave basis set. *Phys. Rev. B* 54 (16), 11169-11186 (1996).

36 Blochl, P.E., Projector augmented-wave method. *Phys. Rev. B* **50,** 17953-17979 (1994).

37 Loschen, C., Carrasco, J., Neyman, K.M., & Illas, F., First-principles LDA plus U and GGA plus U study of cerium oxides: Dependence on the effective U parameter. *Phys. Rev. B* **75,** 8 (2007).

38 Heckert, E.G., Karakoti, A.S., Seal, S., & Self, W.T., The role of cerium redox state in the SOD mimetic activity of nanoceria. *Biomat.* **29,** 2705-2709 (2008).

39 Scholes, F.H., Hughes, A.E., Hardin, S.G., Lynch, P., & Miller, P.R., Influence of hydrogen peroxide in the preparation of nanocrystalline ceria. *Chem. Mat.* **19,** 2321-2328 (2007).

3 INCREASING THE STABILITY OF CERIUM OXIDE NANOPARTICLES BY SURFACE MODIFICATION WITH POLYHYDROXYL COMPOUNDS

3.1 Introduction

Fueled with exciting and major developments in the past few years [1-4], cerium oxide can be considered as the most important rare earth oxides. In conjunction with the benefits of nanotechnology it has found numerous applications in catalysis, sensors and biomedical science[5-11]. These applications stem from its ability to switch oxidation states between +IV and +III depending on the ambience (oxidizing and reducing environment). This renders nanoceria an important biomedical property for radical quenching. Not only does the nanoceria impart protection to cells against the reactive oxygen species (ROS) but has also been shown to protect the normal cells against radiation damage[3]. We have also shown the ability of ceria nanoparticles to prevent retinal degeneration induced by intracellular peroxides[1]. The application of ceria nanoparticles in the treatment of spinal cord injury and other central nervous system based neuron degenerative diseases has proven the biological importance of nanoceria beyond doubt[2]. A whole new world of biological applications of nanoceria is opening with several interesting findings[1-4]. In the light of several reports and concerns of toxic potential of nanomaterials[12], nanoceria, with its unique property of radical quenching can change the present outlook of nanomaterials[13]. However, nanoceria needs to be stabilized in aqueous or non-aqueous media for all practical applications in biology. Thus it is imperative to find a suitable delivery medium for carrying nanoceria to specific locations as an alternative route to intravenous administration.

Earlier we have systematically engineered nanoceria with controlled shapes, sizes as stable dispersions in different media[14,15]. Several different methods of nanoceria synthesis exist in the literature[16-19]. The stability of nanoceria in aqueous and polymeric species was discussed earlier[20-24]. Recently an interesting work was reported on the synthesis of nanoceria in alkaline

medium using alcohothermal treatment[25]. Most of the reported methods are stability protocols and depend on the surface functionalization of nanoceria with high molecular weight polymeric species. The surface functionalization changes the zeta potential of the system thereby extending the stability over a wide pH range. With the increasing use of nanoceria in bio-medical applications, zeta potential and pH of the suspension play a vital role. The adsorption of nanoparticles by the biological species can be influenced by the change in zeta potential. Motivated by these factors; direct synthesis of nanoceria was accomplished in polyhydroxyl solutions. Dextran, glucose, polyethylene glycol (PEG), and polyvinyl alcohol (PVA) are lucrative media for stabilizing nanoceria. Dextran, PVA and PEG have been used prolifically for stabilizing the nanoparticles[26-29] and are also used as solvents/lubricants in commercial eye drops[30]. Poly(acrylic acid) and PEG have been used to stabilize and re-disperse ceria nanoparticles[31]. The biocompatibility of these mediums make them ideal candidate as carriers, provided they can stabilize nanoparticles. Stability can be imparted by steric hindrance or, by complexing ability of the polyhydroxyl compounds through the electronegative oxygen. PEG plays an entirely different role providing only the steric stability to the system resulting in self assembled polyhedral structures and has been discussed by our group elsewhere[15].

Saccharides are an important class of polyhydroxyl compounds. Complexation of trivalent lanthanide cations by mono, di and poly saccharides had been established previously[32-35]. However, the more prominent use of cerium involves its role in oxidation of mono or polysaccharides[36]. In fact, cerium (IV)–alcohol redox systems had been used for chemical initiation of vinyl polymerization[36]. More recently Ce(IV) was used for hydrolysis of DNA which emphasizes the importance of cerium in biological chemistry[37]. The mechanism of complex formation using both open chain and closed chain form of glucose are discussed in

various publications [36,38,39]. The vital points in the mechanism for engineering functionalized nanoceria are listed below.

- Ce(IV) is reduced to Ce(III) in the process of oxidation of glucose to arabinose.
- Polysaccharides have stronger tendency to complex Ce(IV) than the monosaccharides
- Reduction of Ce(IV) to Ce(III) takes place in only highly acidic medium (pH <2) and at this concentration no colloidal particles were detected by light scattering photometry.

We utilized the redox chemistry of the cerium in polysaccharides to synthesize nanoceria. From the revised Pourbaix diagrams[40] it is known that cerium in aqueous solution prefers to stay as $CeO_2.2H_2O$ ($Ce(OH)_4$). Thus a polysaccharide solution of Ce(IV) should produce functionalized nanoceria particles which can easily switch oxidation states upon exposure to highly oxidizing environments (like radicals). However, to utilize the complexing ability and simultaneously form the ceria nanoparticles Ce(III) salt was chosen as a precursor. Also special care was taken to minimize the oxidation of glucose and dextran by maintaining the pH above 2.0 in acidic medium and in the vicinity of 7-8 in basic medium.

In the present paper we discuss the direct synthesis of nanoceria by simple wet chemical routes in polyhydroxyl groups and their stability. Specifically we have discussed the role of oxidizing environment and utilization of complexation of ceria for synthesis in dextran and glucose based aqueous solutions. The size and oxidation state are compared with pure aqueous dispersions and using TEM and UV-Vis spectroscopy. An attempt has been made to understand the role of functional groups in synthesis and stability of the nanoceria particles in acid and basic media. It must be noted that the main emphasis of the present article is to discuss the synthesis in various polyhydroxyl media and hence must not be compared with the precipitation and re-dispersion type procedures. The specific difference between the two methods is the type of functionalization

achieved. Unlike precipitation re-dispersion techniques which depend upon the surface functionalization and modification of charges, we have explored the complex forming ability of ceria with polyhydroxyl compounds as a precursor to synthesize ceria nanoparticles. The role of concentration and type of oxidizer in achieving stable nanoceria particles is the main aspect of the study.

3.2 Results and discussion

3.2.1 Aqueous behavior of cerium

It is known that Ce(IV) remains as a transparent yellow solution below a pH of 3.5 and precipitates as a purple-brown cloudy precipitate above this pH[40] (Equation 1). Similarly Ce(III) remains as a clear solution below pH 6.0 and precipitates as slightly brown to brown purple to white/yellow gel as the pH increases further (Equation 2). This limits the stability of ceria nanoparticles to highly acidic solution (pH 2.0 – 3.5) which is not suitable for biological application.

$Ce^{+4} + 4OH^- \rightarrow Ce(OH)_4$ (1)

$Ce^{+3} + 3OH^- \rightarrow Ce(OH)_3$ (2)

The standard reduction potential of cerium (IV) to cerium (III) is -1.74V (in $HClO_4$). Thus cerium (IV) acts as an effective oxidizing agent. From the Pourbaix diagrams[40] it is also known that oxidation of cerium (III) to cerium (IV) is also possible under controlled conditions where the reverse of equation 3 occurs.

$Ce^{+4} + e^- \rightarrow Ce^{+3}$ (3)

The standard reduction potential for this reaction changes with pH from -1.741V at -0.7818 to below -1.58V at pH value higher than 1.670[40]. The standard reduction potential range suggests

that ceria has a tendency to come back to +III oxidation state in aqueous solution containing electron donors.

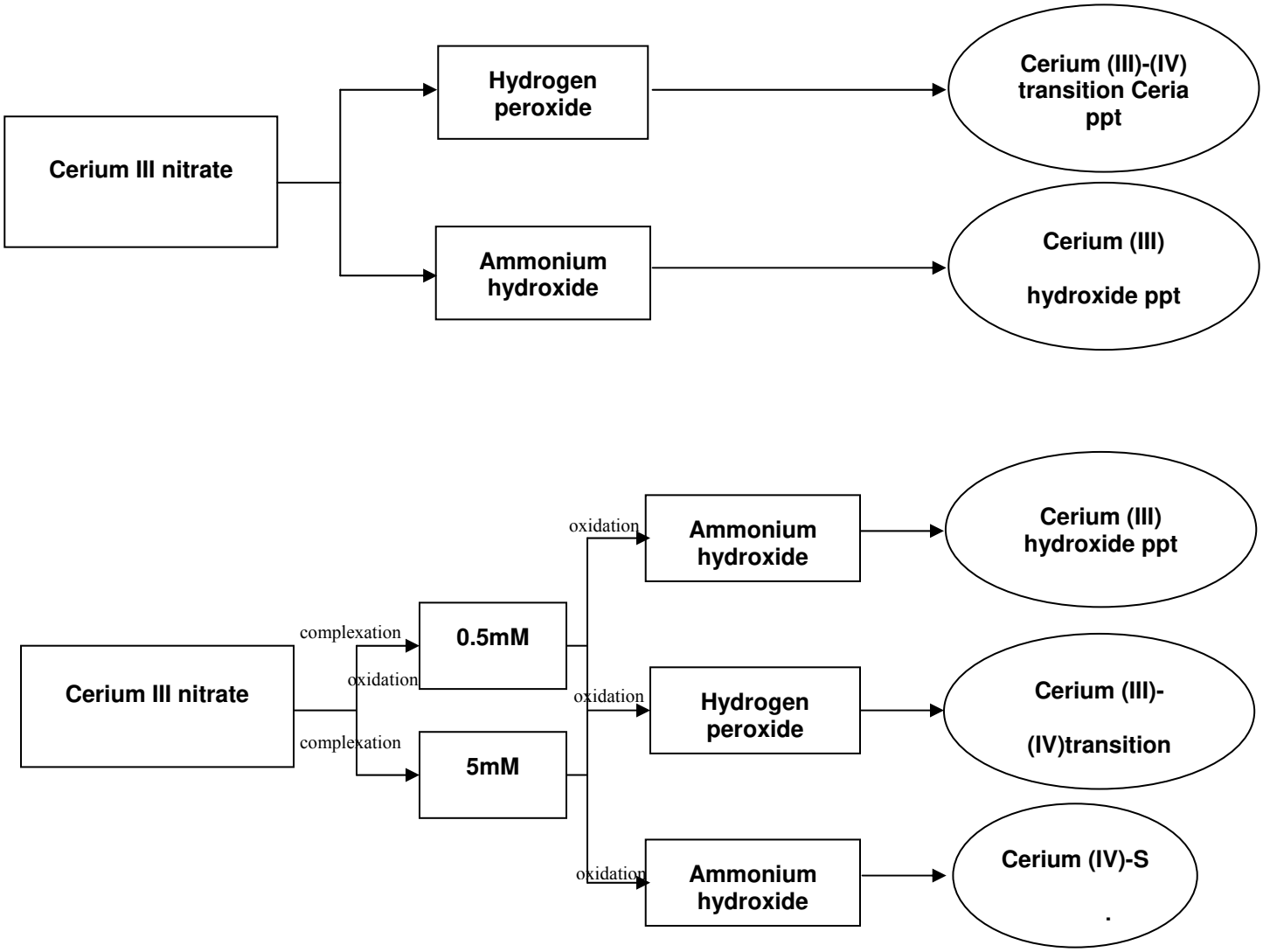

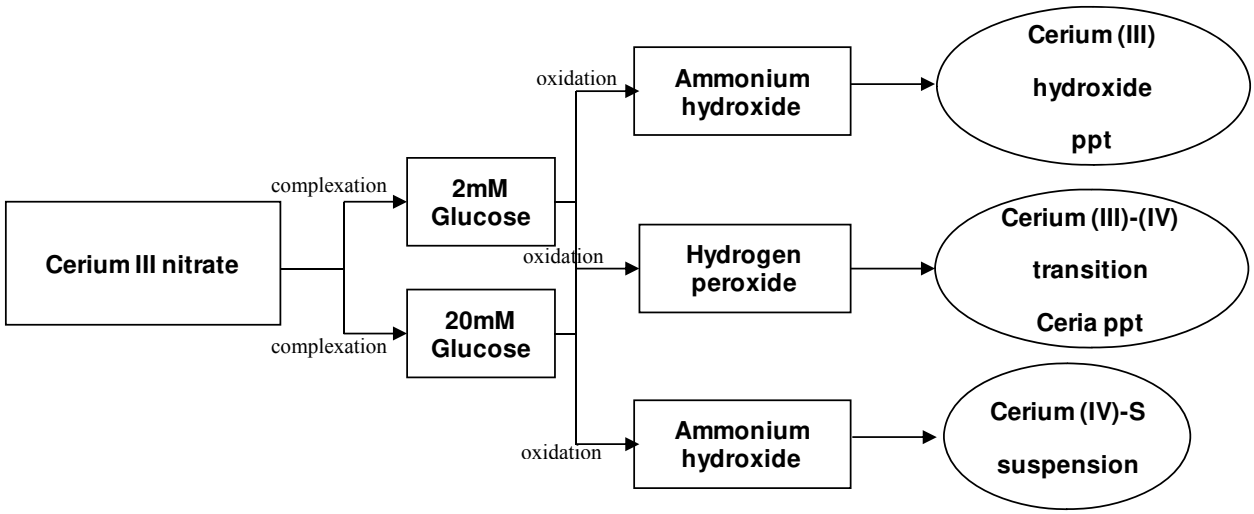

Figure 3-1: Scheme of reactions to stabilize ceria nanoparticles in water glucose and dextran using hydrogen peroxide as acid and ammonia as base (Ce-S cerium saccharides complex)

In the present work H_2O_2 was used as an oxidizer as well as to provide the acidic conditions. H_2O_2 has been used previously to study the rate of change of cerium from +IV to +III oxidation state and its reversal[43-46]. Several research groups have proven the ability of cerium to switch oxidation states which is the prime reason to select H_2O_2 to provide acidic environment[43,45,46]. It must be noted that H_2O_2 dissociates by equation 4 and its redox potential value of $E^0 = 1.5V$ is the driving force for switching of oxidation states of ceria in aqueous dispersions of H_2O_2. Upon addition of H_2O_2 to an aqueous solution of cerium nitrate, cerium (III) was immediately oxidized to form ceria nanoparticles (Ce(IV)) which is confirmed by the yellow color of the solution. Stoichiometric amount of H_2O_2 was added to maintain the pH of the solution above 2 as below this pH Ce(IV) remains in ionic form and no colloidal dispersion is formed[37]. Moreover below a pH 2.0, oxidation of saccharides, will result in the formation Ce(III) hydroxide.

$$H_2O_2 \rightarrow HO_2 + H^+ + e^- \quad E^0 = -1.5V \qquad (4)$$

As the pH is changed from acidic to basic conditions, both Ce(III) and Ce(IV) form hydroxides which settle as a precipitate at a pH of 6.0 and above. Ammonia has been used to provide the basic conditions in the present work. Lanthanides are known to form complexes with

polyhydroxyl molecules[33,34]. This property was used in stabilizing the cerium salts in basic medium which was further exploited to oxidize Ce(III) precursor salt to Ce(IV). A clear yellow solution was observed upon addition of ammonia to cerium nitrate salt dissolved in glucose or dextran while a white-purple precipitate was observed in the absence of saccharides. It must be noted that a minimum amount of glucose/dextran was needed to stabilize the solution in basic medium while no precipitation was observed in acidic conditions. It was found that a concentration of 5mM dextran (mol wt 1000) and 20mM glucose is required to obtain a stable suspension of 30mM ceria. Attempts to use lesser concentration of saccharides resulted in precipitation of cerium hydroxide, thus the results are mostly compared based upon 5mM dextran and 20mM glucose based synthesis in acidic or basic ambience.

3.2.2 Complexation of cerium with sugars

The precipitation of cerium occurs as cerium hydroxide when the ionic product of cerium hydroxide increases above its solubility product. Cerium (III) hydroxide has limited solubility in basic medium and precipitation occur almost instantaneously[40]. If we utilize a base such as ammonium hydroxide for oxidation of cerium (III) the concentration of hydroxyl ion is sufficiently high and precipitation occurs at fairly low concentration of cerium ions. On the other hand, if the cerium ions are utilized in a complexation reaction with polyhydroxyl compounds then it cannot be precipitated by adding base as the molar concentration of free cerium ions is decreased. Only those cerium ions that are free and not involved in bonding with hydroxyl groups of organic species will be precipitated. A simple semi-quantitative analysis can be done to find the minimum concentration of sugars needed to avoid precipitation in presence of ammonia as a precipitating agent.

The number of cerium (III) ions present in 100 mL solution of cerium nitrate is 1.8×10^{21}. The number of glucose units in 100 mL of 2 mM glucose solution is 1.2×10^{20} and in 20 mM glucose solution is 1.2×10^{21} Similarly the number of dextran units (Mol. Wt 1000 daltons) in 0.5 mM dextran solution is 3.01×10^{19} and in 5 mM dextran solution is 3.01×10^{20}

Now assuming that a single bond of cerium with glucose is sufficient to avoid precipitation and since glucose has 5 hydroxyl groups which can be used in complexing ceria molecule, we can at least assume two of these as the possible site for coordination (as shown in scheme 1, 2, the cerium can complex with one or two of the available hydroxyls from glucose which still leaves three more hydroxyl groups that can be complexed with further available cerium ions). Which means each glucose unit can at the least provide two possible sites for coordination with cerium and hence the effective number of cerium binding to one glucose molecule is twice the total number of glucose molecules. Therefore the number of binding units in 2 mM glucose in 100 mL solution is 2.4×10^{20}. Similarly the number of binding units in 20 mM glucose in 100 mL solution is 2.4×10^{21}.

As dextran is a polymer of glucose and by the molecular weight (1000 a.m.u) of the dextran we can safely assume that each dextran has approximately 6 units of glucose. Each glucose unit in dextran can only complex one molecule of cerium because of steric constraints[47] and hence 6 glucose unit in dextran can provide six units for complexation. Thus the effective number of binding sites in 0.5 mM dextran is 1.82×10^{20} while number of binding sites in 5 mM dextran is 1.82×10^{21}.

It is clear that the number of binding sites in glucose (in 2 mM) and dextran (in 0.5 mM) are one order of magnitude less in than the number of cerium ions available in the solution. The free cerium ions precipitate upon addition of base to these solutions. On the other hand at higher

concentration the number of dextran (5 mM) and glucose (20 mM) binding sites are sufficient to bond all cerium ions with at least one unit of dextran or glucose and thereby prevent precipitation in basic medium.

The cerium ions are likely to form a complex as depicted in scheme I and III which can be oxidized from Cerium (III) – Saccharides to Cerium (IV) – Saccharides. It must be noted that cerium is always bonded to the organic species in basic medium and hence always stays as cerium–saccharide complex before oxidation. This is unlike surface functionalization and keeps cerium-saccharide-n(OH) in suspended form. The yellow color of the solution fades slowly indicating the slow reduction of cerium from +IV to +III oxidation state in presence of saccharides and base.

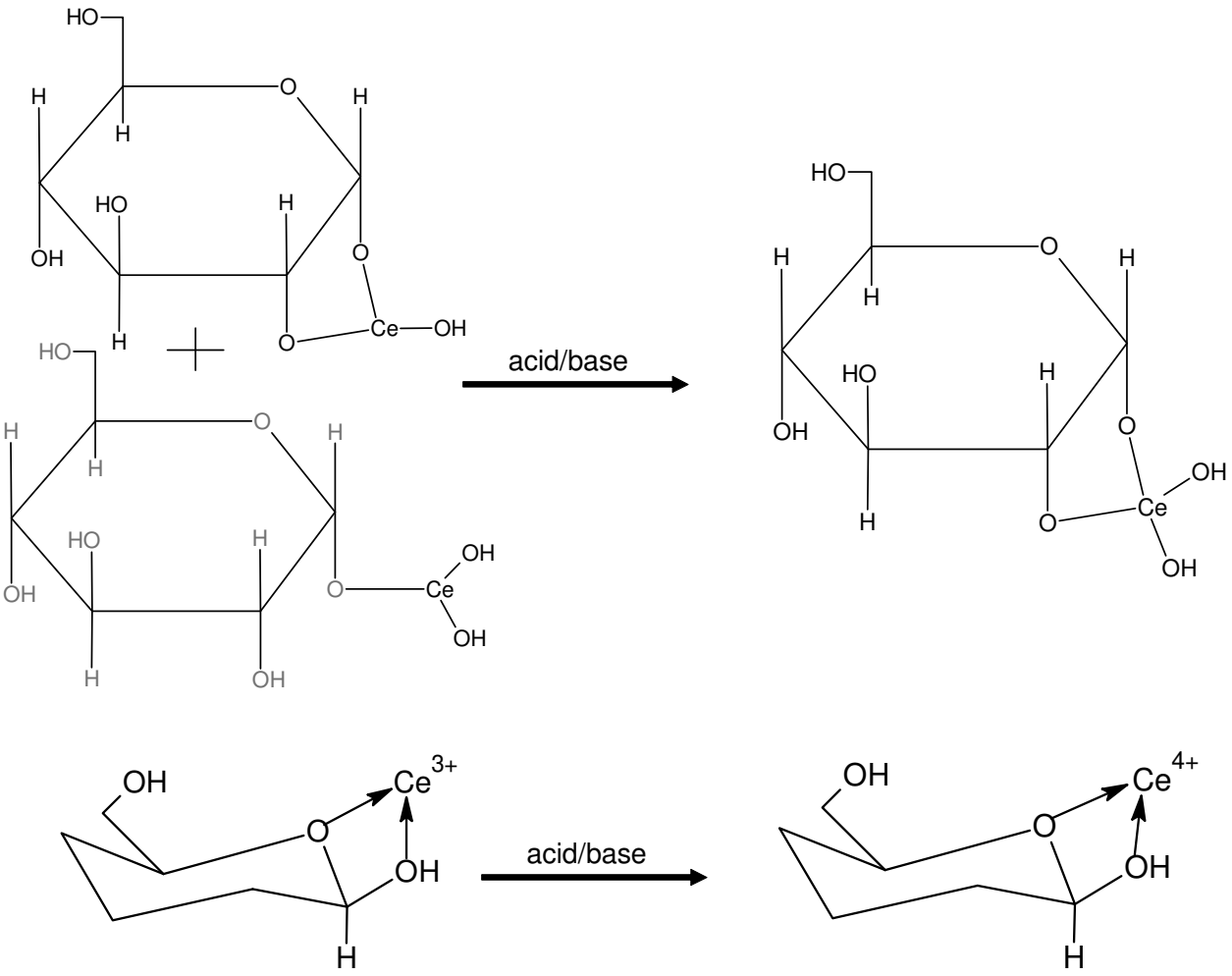

Scheme 3-1: Complexation of cerium(III) with glucose and subsequent oxidation

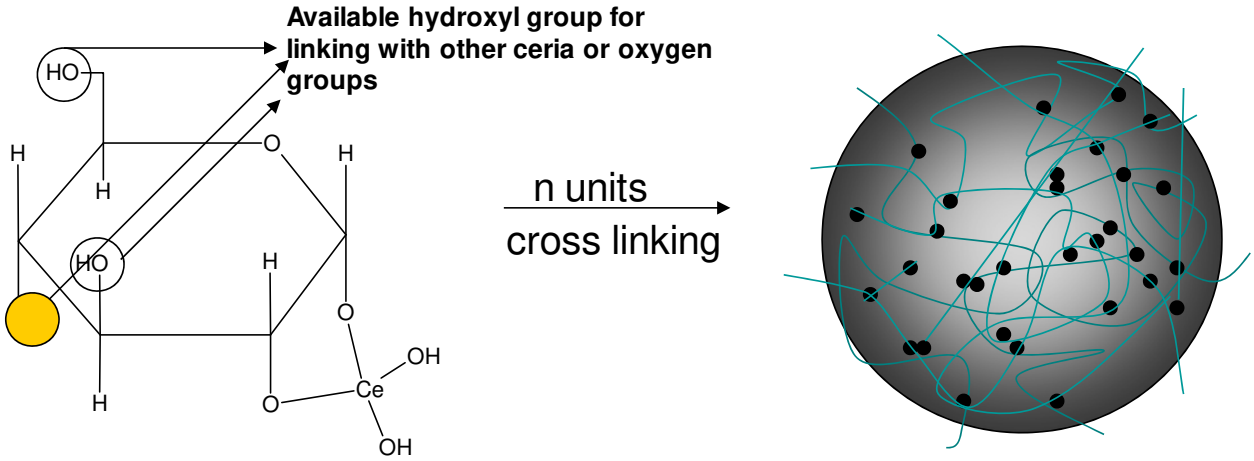

Scheme 3-2: A schematic showing the formation of ceria-saccharides superstructure by cross linking of groups due to further complexation of free hydroxyl groups of glucose with cerium (IV)

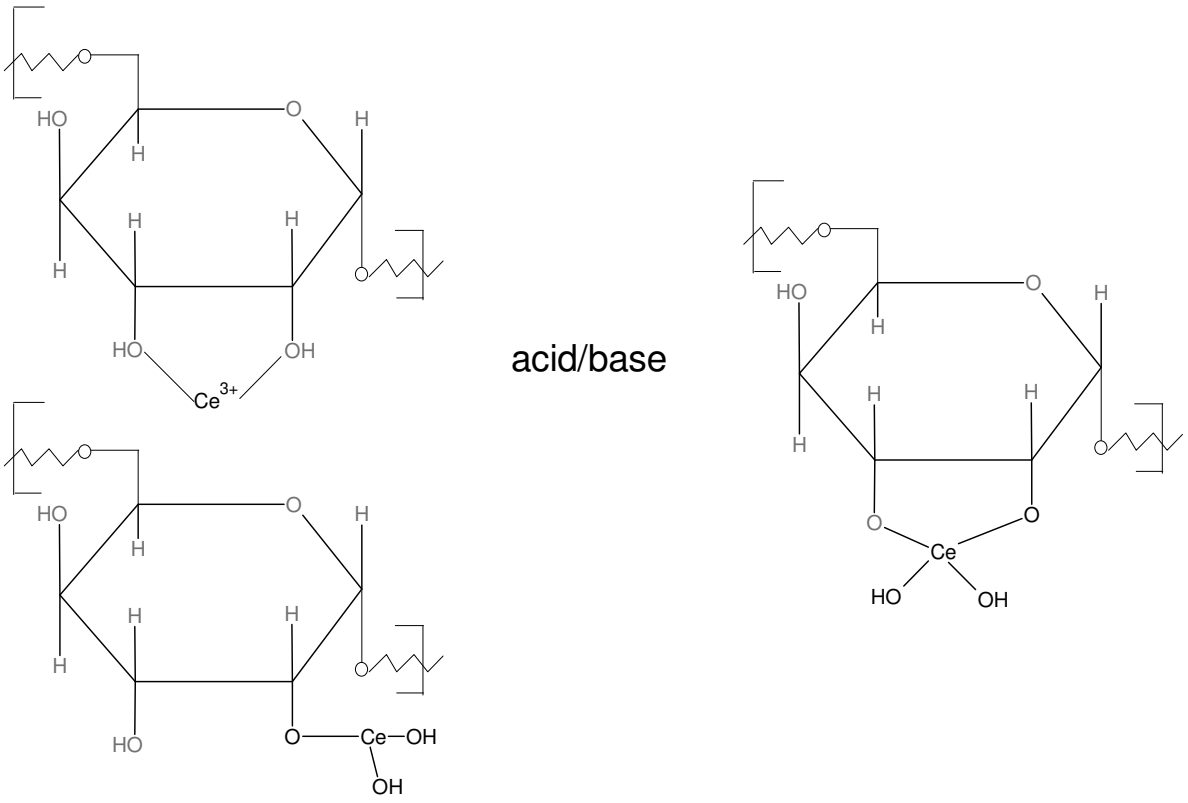

Scheme 3-3: Complexation of cerium(III) with dextran and subsequent oxidation

3.2.3 Dynamic light scattering and particle size

The results from the DLS measurements after 1 day of synthesis are listed in table 1. The particle size measurements were not done for 0.5mM dextran and 2mM glucose based solution in basic medium as they immediately precipitated. The sizes are reported based on the intensity as well as volume distribution. It can be seen that there is no particular trend in particle size based on concentration in acidic medium. The particle sizes as observed by volume percent match closely with water based nanoceria particles. It can also be observed that the particle size increases for higher concentration of glucose while it decreases for higher concentration of dextran. This could

arise from the fact that glucose being smaller sized molecule utilizes free hydroxyls to bring the ceria particle together and this increases with increasing concentration of glucose. Dextran on the other hand is a large molecule and the steric effects keep ceria particles as separate from each other as possible resulting in smaller size with increasing concentration. The particle sizes obtained are compared with the particle size observed under TEM. It must be noted that HRTEM indicates the individual particle size (crystallite size) to be 3-5 nm for each cluster and what is reported as particle size is actually the aggregate size of nanoparticles. A sampling of 100 particles was done and the mean value is given as the particle size for TEM measurements. The difference in the observed particle sizes as explained by several researchers could be ascribed to the way particles behave in solution[20,21]. The maximum and minimum particle size observed in TEM for different synthesis methods is almost the same in all the cases independent of the composition of sugars. The difference in the values obtained from electron microscopy and DLS measurement can be ascribed to the absence of contrast from the polymers in electron diffraction as explained by Berret et.al[21]. However, it can be observed that the particle size in basic medium in both glucose and dextran looks unreasonable. One of the reasons for such an observation could be presence of very small particles which are always attached / surrounded by an envelope of saccharide. The appearance of the same as ceria nanoparticles (3-5 nm) in TEM (discussed in section 3.4) proves the existence of ceria nanoparticles in highly dispersed state.

Table 3-A: Comparison of particle size (agglomerate size) observed under DLS and TEM

Sample	**Particle size (DLS) (nm)**		**Particle Size (TEM) (nm)**
	Volume %	Intensity	Average

Glucose 2mM (Acid)	24.86 ±3	35.09 ±1	17.2
Glucose 20mM (Acid)	28.98 ±2	47.19 ±2.5	15.8
Water	28.48 ±0.8	33.95 ±0.5	10.6
Dextran 0.5mM (Acid)	31.19 ±2.1	44.67 ±0.9	17.2
Dextran 5mM (Acid)	27.5 ±0.2	30.3 ±0.2	13.4
Glucose 20mM (Base)	0.64	0.69	3-5
Dextran 5mM (Base)	0.66	0.74	3-5

Zeta potential measurements were carried out to find the affect of synthesis medium. The value of the zeta potential varied between +16 to + 40 mV for different solutions but was always positive. The nanoparticles present in the solution are in a state of constant change in oxidation state as well as particle size which will be evident from the results of UV-Vis and TEM analysis in the following sections. The envelope of glucose and dextran around the particles changes with the change in oxidation state upon aging.. This resulted in inconsistent zeta potential values in aged solutions and is not reported.

3.2.4 TEM analysis

Figure 2 shows the TEM images of the ceria nanoparticles synthesized under various experimental conditions. Though no significant difference could be observed in the particles synthesized in either dextran or glucose, a marked difference was seen in the size of the particles synthesized in acidic and basic medium.

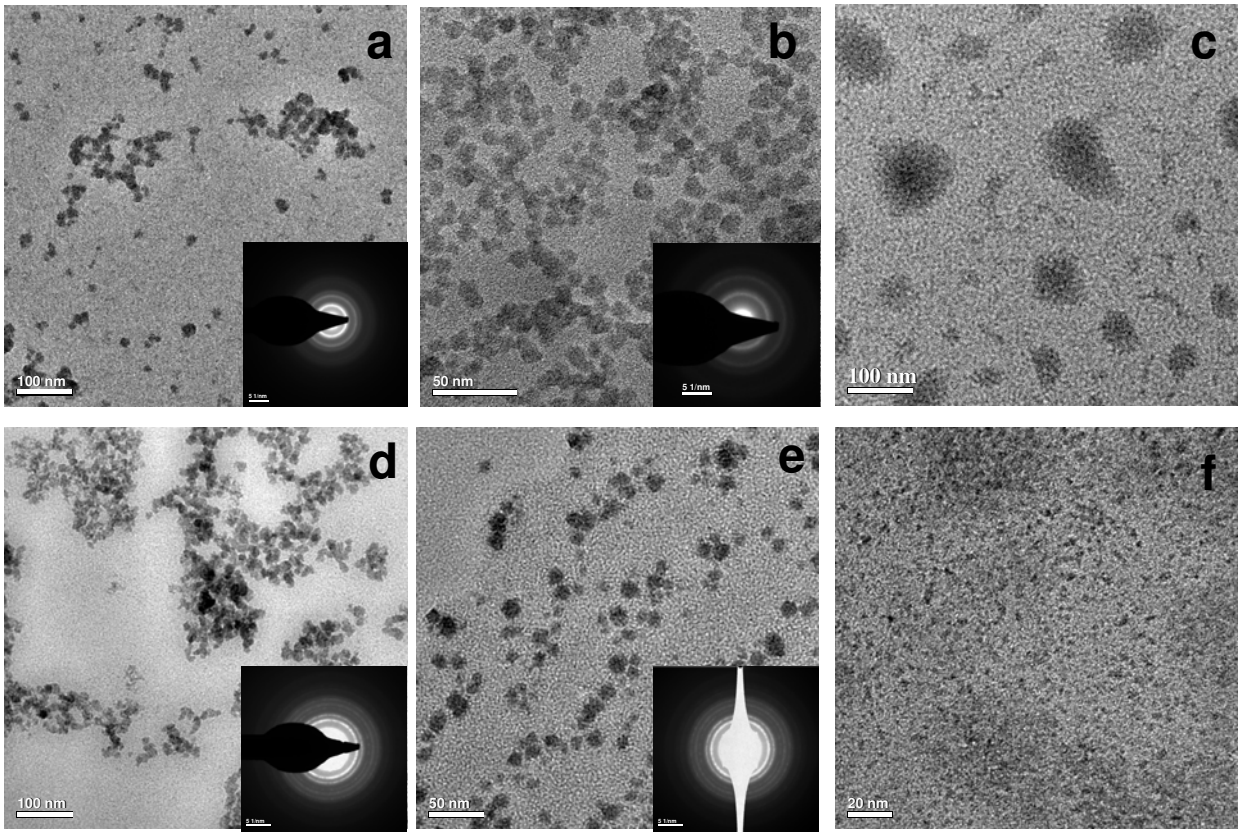

Figure 3-2: TEM micrographs for ceria synthesized in different conditions. Ceria synthesized in glucose using a) 2mM glucose/acid b) 20mM glucose/acid c) 20mM glucose/base and in dextran using d) 0.5mM dextran/acid e) 5mM dextran/acid f) 5mM dextran/base.

It can be observed directly from the figure 2 that particles synthesized in basic medium have less agglomeration as compared to the acidic medium. The individual particle size remained to be 3-5 nanometers in both the conditions while [111] remained to be the preferred plane (d=0.317nm ±2%) on the surface in both the media. It can be observed from figure 2 that there is no significant difference in the particles synthesized in acidic medium with either glucose or dextran. The observation of TEM is consistent with those reported by Si et al and appears as either short chain like or individual clusters because of the presence of polymeric/organic species. Weak agglomerates of 20-30 nm with individual particle size of 3-5 nm could be seen. The SAED pattern in the inset confirms the polycrystalline nature as well as fluorite structure of ceria nanoparticles.

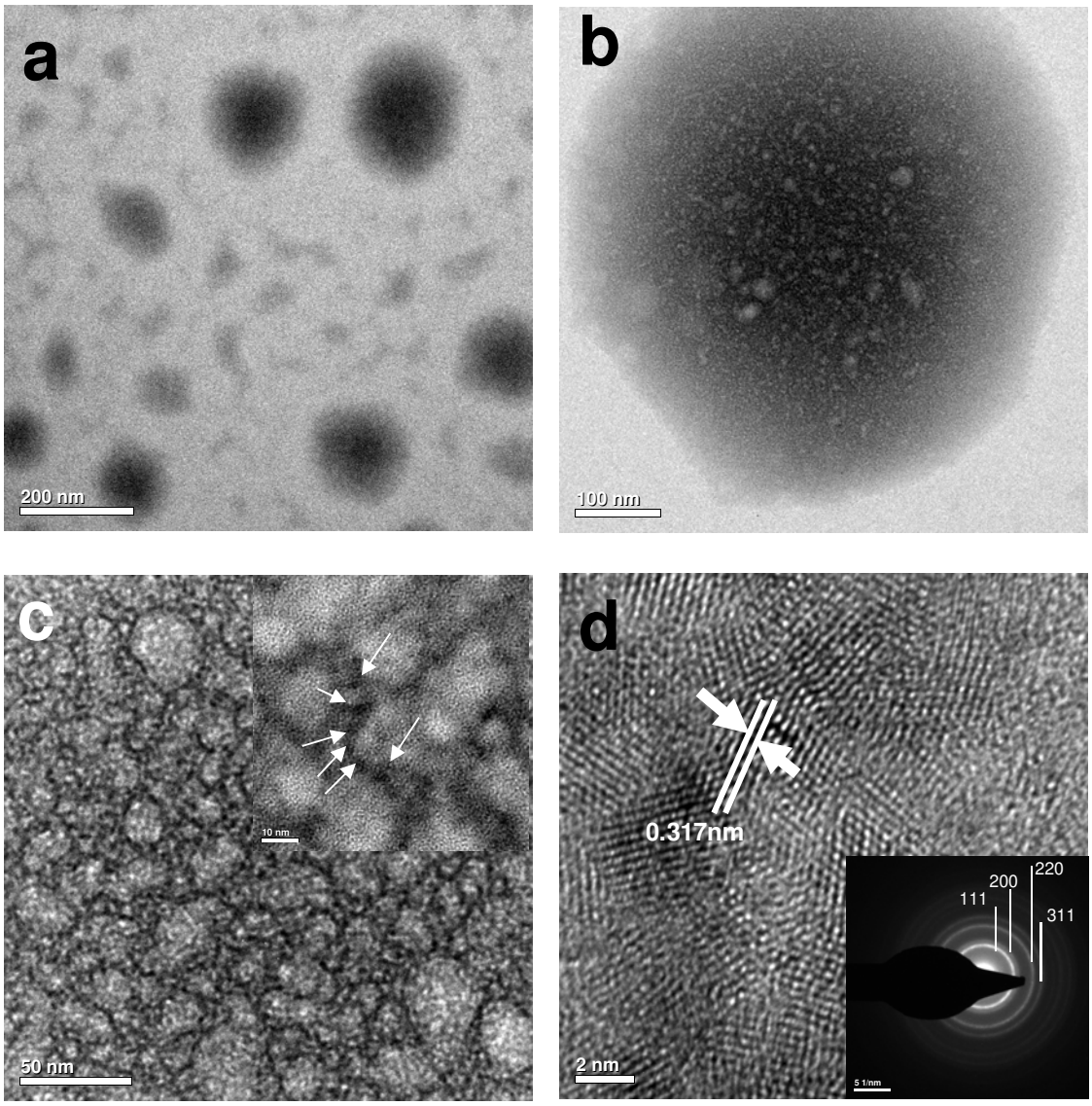

Figure 3-3: TEM images of ceria synthesized in 20mM glucose/base. a) Spherical polymeric structures b) Representative high magnification image of one of the spherical structure c) High magnification image depicts hollow nature (inset shows particle trapped in the structure) d) HRTEM image of the particles trapped (inset confirms the fluorite structure of ceria with (111) as the preferred plane at the surface).

The agglomeration was significantly reduced in basic medium. It was further observed that glucose in basic medium formed interlinked superstructures which can trap the ceria nanoparticles (figure 3). This observation confirms the hypothesis (each glucose unit can at the

least complex two cerium ions) mentioned in section 3.2. However, the actual bonding environment and the nature of the co-ordination are not clear at the moment.

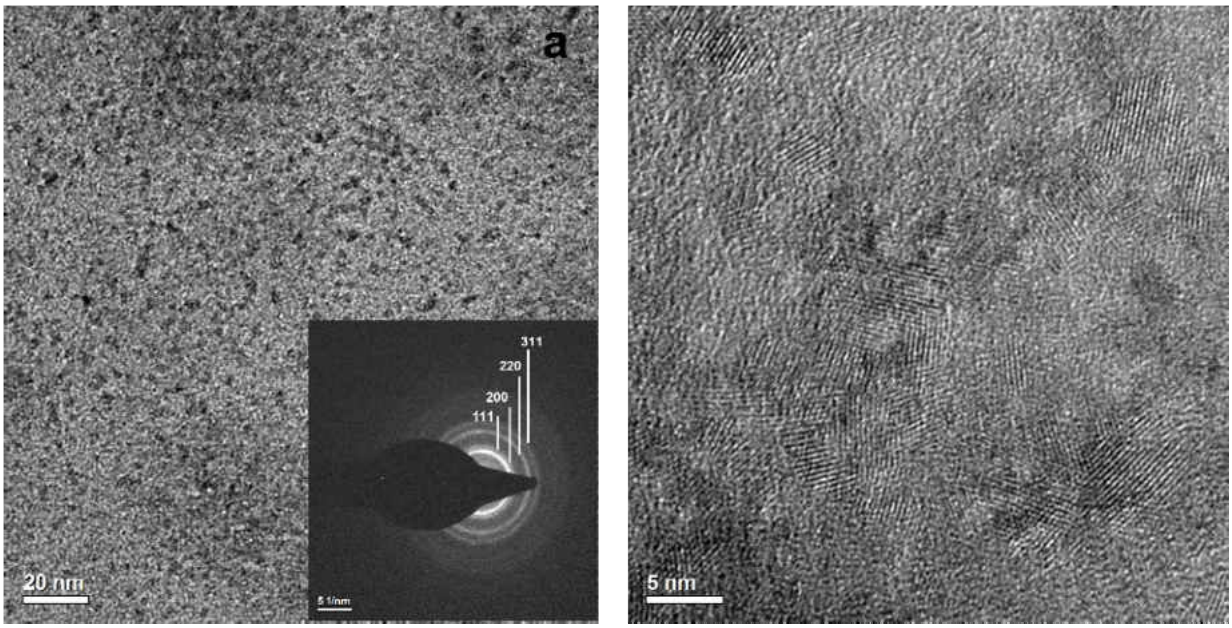

Figure 3-4: HRTEM micrograph of ceria synthesized in 5mM dextran/base. a) Low magnification image showing well dispersed 3-5nm particles (inset confirms the fluorite structure of ceria) b) High magnification image showing (111) as the preferred plane on the surface

The ability of the glucose to form hollow spherical agglomerated particles following a hydrothermal approach had been reported previously[48]. The glucose spherical structures then potentially trap the oxide nanoparticles. Inset SAED Pattern in figure 3 confirms the fluorite structure of ceria. Despite the absence of such stabilizing templates, the ceria synthesized using dextran in basic medium showed well dispersed 3-5nm particles (Figure 4). This observation directly leads to difference in the complexation behavior of glucose and dextran. Glucose being a monosaccharide has free hydroxyl groups at C_1 and C_6 positions. Cerium can complex with glucose using both C_1-C_2 hydroxyl groups[36] or through C_1 hydroxyl and ring oxygen (Scheme 1)[36]. Any of the remaining free hydroxyl groups in C_3, C_4, C_5 and C_6 can further bond available cerium ions and form a spherical assembly as observed in figure 3 (Scheme 2). Dextran, on the

other hand is anhydroglucose polymer, which mainly consists 95% ά-D-(1-6) linkages and branched α-(1-3) linkages. Due to the lack of hydroxyl groups it can form glycolic complex at C_2-C_3 and C_3-C_4 positions or simply co-ordinate with C_2-OH[47]. The steric hindrance and lack of hydroxyl groups to further complex cerium ions can be ascribed to the absence of spherical superstructures (Scheme 3)[47] as seen in glucose. This steric hindrance also helps the ceria nanoparticles to agglomerate less and keeps 3-5nm ceria nanoparticles in suspension.

3.2.5 Changes in oxidation state

UV-Visible spectrophotometry of cerium is of particular interest as it provides quantitative information about the type of oxidation state and the rate of reaction[49]. Complexation of cerium ions by saccharides as well as their oxidation kinetics has been studied and reported previously[39,47]. Of particular interest to us was the change in the oxidation state of cerium while synthesizing ceria from cerium (III) precursor salts and the retention of oxidation state in stable dispersion of functionalized ceria nanoparticles. A summary of behavior of cerium ions oxidized in different medium is depicted in figure 5 (a-d). It is known that Ce(III) absorbs in both UV and visible regions while the Ce(IV) absorbs in the visible region (380nm in cerium ammonium nitrate).). It is evident from our study that while the ceria shows active switching of oxidation states in acidic medium it is rather more stabilized in the higher oxidation state in the basic medium. One must note that the rate at which cerium shifts its oxidation state from +III to +IV upon addition of base or acid is relatively free to the nature of oxidizer and complexing media.

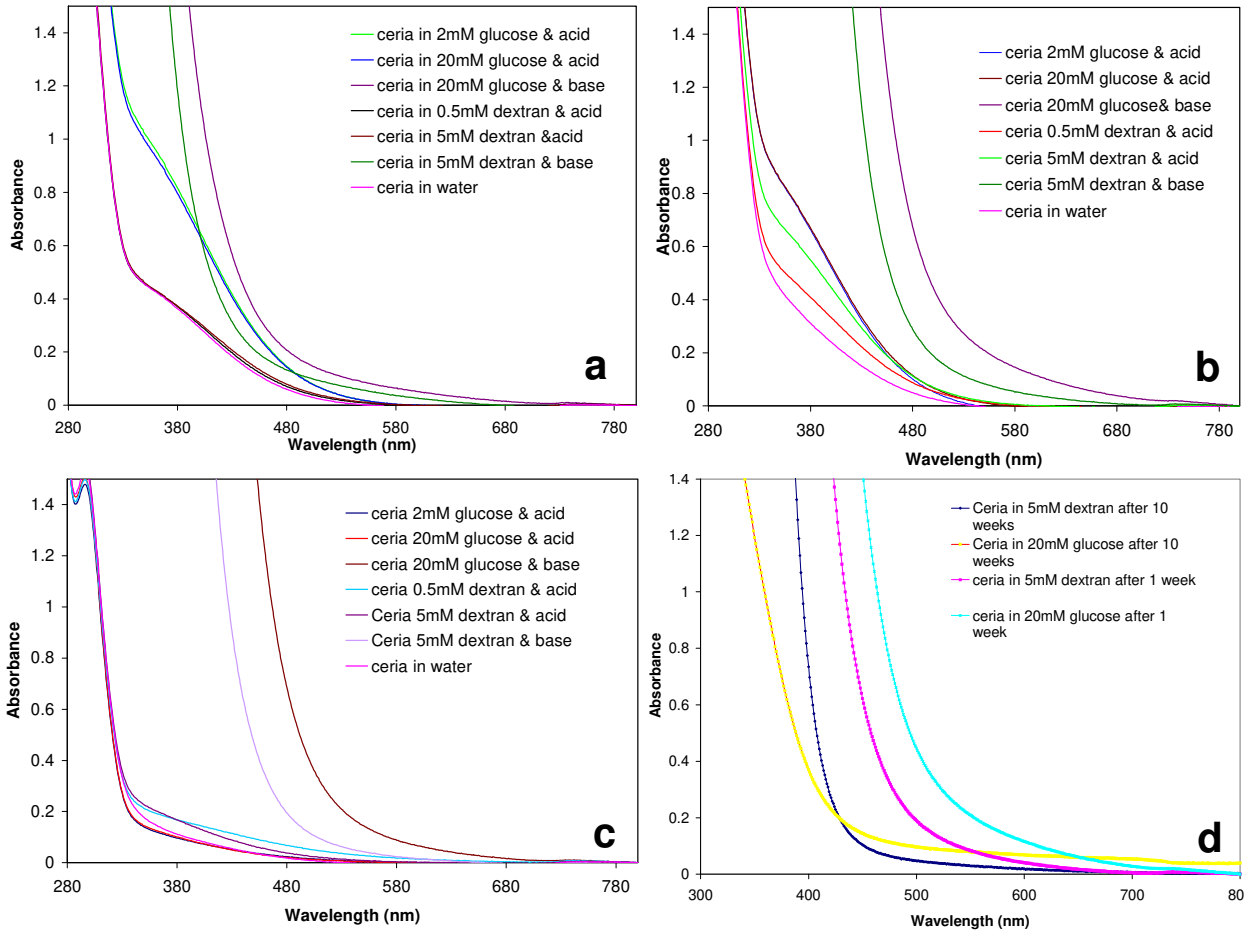

Figure 3-5: Variation in absorption values of ceria solution in different mediums a) freshly prepared b) aged for 1 week c) aged for 2 weeks (Plot shows the change in oxidation states depending upon the aging and synthesis medium) d) ceria synthesized in basic conditions in glucose and dextran (Plot shows the slow shift of cerium (IV) to cerium (III) oxidation state after 10 weeks of aging)

The difference in the initial absorbance values is ascribed to different soak time allowed before UV-Vis experiments. It is evident from figure 5c and 5d that in acidic medium most of the cerium +III have recovered after initial oxidation within 15 days while in basic medium the transition was rather slow. The switching of oxidation state in acidic environment is also observed in aqueous medium and is generally accompanied by pH change as well as slight precipitation of ceria. The extent of precipitation is substantially reduced in presence of glucose and dextran in acidic medium. Moreover the samples oxidized in basic environment were stable

in +IV oxidation state up to 2 months of study (data shown only for 15 days as a comparison with acidic and aqueous medium). While hydrogen peroxide is a strong oxidizer and it can hydrolyze the reverse of scheme I and III to generate the Ce(III), it is believed, that ammonia cannot hydrolyze the reverse reaction as efficiently. It has also been established that hydrogen peroxide produces peroxyl radical species (OOH*) in solution which are very reactive and can reduce cerium IV ions irreversibly[43,44]. Also, the basic conditions and excess of oxygen favor the higher oxidation state of ceria imparting increased stability for ceria in basic medium compared to the acidic medium. Thus the role of saccharides is limited to provide initial functionalization that prevents precipitation in basic medium and which does not, in any way, interferes with the behavior of ceria.

3.2.6 pH change with aging

Time dependent behavior of ceria suspensions was also monitored using pH change. Table 2 shows the change in pH with respect to time for various samples during the experimentation.

Table 3-B: Change in pH of ceria suspensions synthesized in various media as a function of time

Precursor	Medium	No of Days	pH
Cerium (III) nitrate	Aqueous	0 7 15	3.6 3.4 3.7
Cerium (III) nitrate	water/glucose base	0 7	7.6 6.7

		15	5.9
Cerium (III) nitrate	water / glucose acid	0 7 15	3.7 3.1 3.8
Cerium (III) nitrate	water/dextran base	0 7 15	7.7 7.6 7.5
Cerium (III) nitrate	water/dextran acid	0 7 15	3.4 3.1 3.2
Cerium (IV) ammonium nitrate	Aqueous	-	2.3
Cerium (IV) ammonium nitrate	water/glucose	-	1.1

We suspected a slow increase in acidity of ceria suspensions in glucose could correspond to the oxidation of glucose. However, a critical TLC has denied the possibility. Samples from both glucose and dextran were characterized using TLC. It was observed that both glucose and dextran in either acidic or basic conditions gave just one spot with same Rf value (0.47 glucose)

as for the pure compounds. Thus it was concluded that neither glucose nor dextran were oxidized in either acidic or basic conditions used in the present synthesis protocol.

As mentioned earlier, the revised pourbiax diagrams[40] suggest that cerium (IV) should be present in a colloidal solution as $CeO_2 \cdot 2H_2O$ above a pH of 2.0 and as precipitate above pH 3.5 (Figure 6). Though the observations were similar to as expected from the Pourbaix diagrams but, the ceria synthesized using saccharides showed delayed change of pH and hence slower precipitation. It must be noted that a small amount of very fine precipitates can be seen in all the three media (water, dextran and glucose) in acidic conditions. This agglomeration is a weak agglomeration and the fine precipitates disappear upon mild shaking. Heavy precipitation above pH 3.5 was not observed as Ce(IV) reverts back to Ce(III) in H_2O_2. This rate is slowed down in the presence of saccharides due to complexation. This is important because of the fact that the solution always has a mixture of +III and +IV oxidation state at any time until the complete solution turns back to cerium (III) which is useful in governing the redox property of ceria depending upon the environment. The nanoceria could be synthesized and suspended directly in a range of pH from 2.0 to 8.0.

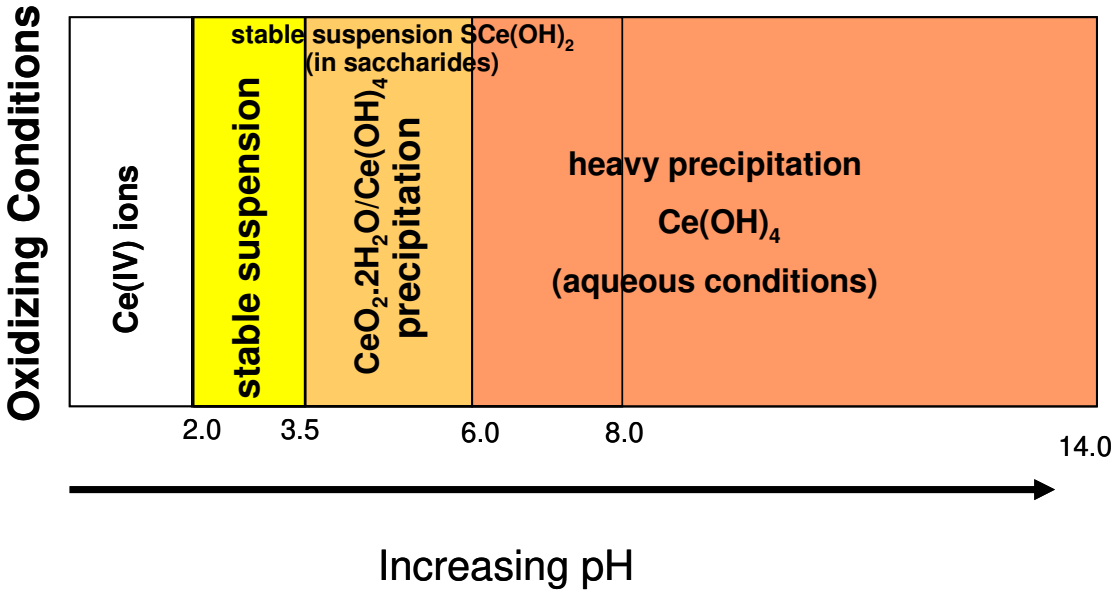

Figure 3-6: Precipitation behavior of Ce(IV) with respect to change in pH in oxidizing environment. The narrow stability range of ceria suspension can be extended up to a pH of 8.0 by the use of saccharides (dashed lines). Cerium is present as Ce(IV) ions (pH 0 – 2.0), Stable suspension $CeO_2.2H_2O$ (pH 2.0 – 3.5), precipitate as $CeO_2.2H_2O$ (pH 3.5 – 6.0), precipitate heavily as $Ce(OH)_4$ (pH 6.0 and above), stable suspension in saccharides as S-$Ce(OH)_X$ (pH 2.0 - 8.0)

In the present study ceria nanoparticles were not prepared and the goal of synthesizing the stable nanoceria directly in desired pH conditions has been successfully achieved. The absence of nanocrystalline ceria from the Ce(IV) precursor in both aqueous media (with and without saccharides) has unequivocally confirmed the need for synthesizing the nanoparticles from a Ce(III) precursor. This will also leverage more flexibility in controlling the chemistry and structure of the end product.

3.3 Summary

This study clearly demonstrates that nanoceria can be synthesized directly in mono/polysaccharides by oxidizing the species in both acidic and basic environment. Importantly, the initial complex formed between cerium and sugars does not hinder the property of ceria to switch its oxidation state based on the environment which is very important given the

role of nanoceria in biology and catalysis. It was noted that the kinetics of switching of oxidation states in solution specifically regeneration from cerium (IV) to cerium (III) oxidation state is slower in basic medium as compared to acidic medium. Moreover, from UV-Vis results it is clear that the +IV oxidation state was retained in basic medium for more than 2 months as a stable suspension which proves the tunability of nanoceria with respect to ambience and aging. Both dextran and glucose can be used efficiently to synthesize nanoceria with a enhanced stability in dextran. pH of the solution has to be maintained to avoid precipitation of cerium hydroxide as well as oxidation of saccharides and achieve stable suspensions.

3.4 Materials and methods

3.4.1 Synthesis of aqueous nanoceria:

Nanoceria was synthesized in water by simple oxidation of cerium ions using a suitable oxidizer. 0.5-0.7 gm of cerium nitrate (III) hexahydrate (Sigma Aldrich) was dissolved in 50ml of de-ionized water (18.2MΩ). The solution containing Ce(III) ions was then oxidized using (0.2ml) of hydrogen peroxide (30% w/w Sigma Aldrich) for acidic oxidation and (0.05ml) of ammonia for base mediated oxidation (30% w/w Sigma Aldrich).

3.4.2 Synthesis of glucose and dextran based nanoceria

The aqueous procedure was slightly modified to incorporate the polymers in solution. The preparation of nanoceria in these polyhydroxyl groups was done in two separate concentrations. 0.5 & 5 mM solution of dextran (Sigma Aldrich) (M.W 1000) and 2 & 20mM solution of D-glucose (Sigma Aldrich) were prepared. Cerium nitrate (III) hexahydrate was then dissolved in these solutions and stirred to allow complete complexation to take place. Solution was then oxidized using hydrogen peroxide (acidic) and ammonia (basic). A scheme of various experimental conditions is shown in figure 1.

3.4.3 UV-VIS spectroscopy

Solutions were characterized using UV-VIS spectrophotometer (Cary One, Varian). The spectra were recorded for fresh, 1 week and 15 days aged samples and compared for analysis. In order to minimize the oxidation of glucose and dextran, minimum amount of oxidizers/acid/base were added to maintain the pH. Continuous spectra were recorded for 20mM glucose, 5mM dextran and pure water based samples to monitor the rate of change of oxidation state of cerium from (III) to (IV) in both acidic and basic media.

3.4.4 Transmission electron microscopy (TEM)

High resolution TEM (HRTEM) images were taken using Philips TECNAI G^2 microscope, for the particles aged in solution for 1 week to confirm the size, morphology and crystallinity of the particles. Samples for analysis were prepared by dropping the solution on carbon coated copper grid and were dried in vacuum.

3.4.5 Thin layer chromatography (TLC)

Glucose and dextran were identified by thin layer chromatography[41] to ascertain the complexation proceeded without oxidation. Silica gel plates were used with ethyl acetate-acetic acid-methanol-water (60:15:15:10) as the solvent for identification of glucose. Chromatographic development for dextran was carried out using nitromethane:1-propanol: water (2:5:1.5) as the eluent[42] and ethanolic solution of alpha-naphthol in sulfuric acid was used for identification in both the cases.

3.4.6 Dynamic light scattering (DLS):

Particle size and zeta potential measurements were carried out using light scattering measurements from Zeta Sizer Nano (Malvern Instruments). This instrument uses a 633 nm wavelength laser to measure the particle size which does not interfere with the absorption wavelength of either saccharides or nanoceria. Samples were subjected to centrifugation at

7500RPM for 10 minutes and the suspension was used for measurements (no precipitation was observed during the centrifugation).

3.5 References

1 Chen, J.; Patil, S.; Seal, S.; McGinnis, J. F. *Nature Nanotechnology* **2006**, *1*, 142-150.

2 Das, M.; Patil, S.; Bhargava, N.; Kanga, J.-F.; Riedela, L. M.; Seal, S.; Hickman, J. J. *Biomaterials* **2006**, *Accepted*.

3 Tarnuzzer, R. W.; Colon, J.; Patil, S.; Seal, S. *Nano Lett.* **2005**, *5*, 2573-2577.

4 Korsvik, C.; Patil, S.; Seal, S.; Self, W. T. *Chemical Communications* **2007**, *accepted*.

5 Lashtabeg, A.; Skinner, S. J. *Journal of Materials Chemistry* **2006**, *16*, 3161.

6 Sayle, T. X. T.; Parker, S. C.; Sayle, D. C. *Physical Chemistry Chemical Physics* **2005**, *7*, 2936.

7 Patil, S.; Kuiry, S. C.; Seal, S. *Proceedings Of The Royal Society Of London Series A-Mathematical Physical And Engineering Sciences* **2004**, *460*, 3569-3587.

8 Feng, X.; Sayle, D. C.; Wang, Z. L.; Paras, M. S.; Santora, B.; Sutorik, A. C.; Sayle, T. X. T.; Yang, Y.; Ding, Y.; Wang, X.; Her, Y.-S. *Science* **2006**, *312*, 1504-1508.

9 Fu, Q.; Saltsburg, H.; Flytzani-Stephanopoulos, M. *Science* **2003**, *301*, 935-938.

10 Andersson, D. A.; Simak, S. I.; Skorodumova, N. V.; Abrikosov, I. A.; Johansson, B. *PNAS* **2006**, *103*, 3518-3521.

11 Deshpande, S.; Patil, S.; Kuchibhatla, S. V. N. T.; Seal, S. *Applied Physics Letters* **2005**, *87*, 133113.

12 Nel, A.; Xia, T.; Madler, L.; Li, N. *Science* **2006**, *311*, 622-627.

13 Karakoti, A. S.; Hench, L. L.; Seal, S. *JOM* **2006**, *58*, 77-82.

14 Kuiry, S. C.; Patil, S. D.; Deshpande, S.; Seal, S. *J. Phys. Chem. B* **2005**, *109*, 6936-6939.

15 Kuchibhatla, V. S.; Karakoti, A. S.; Seal, S. *Nanotechnology* **2007**, *Accepted*.

16 Qi, R. J.; Zhu, Y. J.; Cheng, G. F.; Huang, Y. H. *Nanotechnology* **2005**, *16*, 2502-2506.

17 Hu, C. G.; Zhang, Z. W.; Liu, H.; Gao, P. X.; Wang, Z. L. *Nanotechnology* **2006**, *17*, 5983-5987.

18 Sathyamurthy, S.; Leonard, K. J.; Dabestani, R. T.; Paranthaman, M. P. *Nanotechnology* **2005**, *16*, 1960-1964.

19 Sun, C. W.; Sun, J.; Xiao, G. L.; Zhang, H. R.; Qiu, X. P.; Li, H.; Chen, L. Q. *Journal Of Physical Chemistry B* **2006**, *110*, 13445-13452.

20 Zhang, F.; Jin, Q.; Chan, S. W. *Journal Of Applied Physics* **2004**, *95*, 4319-4326.

21 Berret, J. F.; Sehgal, A.; Morvan, M.; Sandre, O.; Vacher, A.; Airiau, M. *Journal Of Colloid And Interface Science* **2006**, *303*, 315-318.

22 Spalla, O.; Cabane, B. *Colloid And Polymer Science* **1993**, *271*, 357-371.

23 Spalla, O.; Nabavi, M.; Minter, J.; Cabane, B. *Colloid And Polymer Science* **1996**, *274*, 555-567.

24 Nabavi, M.; Spalla, O.; Cabane, B. *Journal Of Colloid And Interface Science* **1993**, *160*, 459-471.

25 Si, R.; Zhang, Y. W.; You, L. P.; Yan, C. R. *Journal Of Physical Chemistry B* **2006**, *110*, 5994-6000.

26 Mehvar, R. *Journal Of Controlled Release* **2000**, *69*, 1-25.

27 Pardoe, H.; Chua-anusorn, W.; St Pierre, T. G.; Dobson, J. *Journal Of Magnetism And Magnetic Materials* **2001**, *225*, 41-46.

28 Tao, K.; Dou, H. J.; Sun, K. *Colloids And Surfaces A-Physicochemical And Engineering Aspects* **2006**, *290*, 70-76.

29 Bergen, J. M.; Von Recum, H. A.; Goodman, T. T.; Massey, A. P.; Pun, S. H. *Macromolecular Bioscience* **2006**, *6*, 506-516.

30 Maia, J.; Ferreira, L.; Carvalho, R.; Ramos, M. A.; Gil, M. H. *Polymer* **2005**, *46*, 9604-9614.

31 Uekawa, N.; Ueta, M.; Wu, Y. J.; Kakegawa, K. *Journal Of Materials Research* **2004**, *19*, 1087-1092.

32 Israeli, Y.; Morel, J.-P.; Morel-Desrosiers, N. *Carbohydrate Research* **1994**, *263*, 25.

33 Angyal, S. J.; Craig, D. C. *Carbohydrate Research* **1993**, *241*, 1.

34 Geetha, K.; Raghavan, M. S. S.; Kulshreshtha, S. K.; Sasikala, R.; Rao, C. P. *Carbohydrate Research* **1995**, *271*, 163.

35 L. A. Gugliemelli, W. M. D. C. R. R. C. L. S. *Journal of Polymer Science Part B: Polymer Letters* **1972**, *10*, 415-421.

36 Charles R. Pottenger, D. C. J. *Journal of Polymer Science Part A-1: Polymer Chemistry* **1970**, *8*, 301-318.

37 Kajimura, A.; Sumaoka, J.; Komiyama, M. *Carbohydrate Research* **1998**, *309*, 345.

38 Kabir ud, D.; Ali, M. S.; Khan, Z. *Colloid And Polymer Science* **2005**, *284*, 10-18.

39 Virtanen, P. O. I.; Lindroos, R.; Oikarinen, E.; Vaskuri, J. *Carbohydrate Research* **1987**, *167*, 29.

40 Hayes, S. A.; Yu, P.; O'Keefe, T. J.; O'Keefe, M. J.; Stoffer, J. O. *Journal Of The Electrochemical Society* **2002**, *149*, C623-C630.

41 Fried, B.; Sherma, J. *Thin-Layer Chromatography: Techniques and Applications*; 2nd ed.; Marcel Dekker Inc.: New York, 1986, 281-294.

42 Wang, Y.; Suzuki, A.; Tanaka, T.; Kumura, H.; Shimazaki, K. *Journal Of Dairy Science* **2004**, *87*, 1627-1633.

43 Sigler, P. B.; Masters, B. J. *J. Am. Chem. Soc.* **1957**, *79*, 6353-6357.

44 Medalia, A.; Byrne, B. *Anal. Chem.* **1951**, *23*, 453-456.

45 Libby, W. F. *J. Phys. Chem.* **1952**, *56*, 863-868.

46 Czapski, G.; Bielski, B. H. J.; Sutin, N. *J. Phys. Chem.* **1963**, *67*, 201-203.

47 Samal, R. K.; Satrusallya, S. C.; Sahoo, P. K.; Ray, S. S.; Nayak, S. N. *Colloid And Polymer Science* **1984**, *262*, 939-947.

48 Titirici, M. M.; Antonietti, M.; Thomas, A. *Chem. Mater.* **2006**, *18*, 3808-3812.

49 Tsunekawa, S.; Fukuda, T.; Kasuya, A. *Journal of Applied Physics* **2000**, *87*, 1318.

4 PEGYLATED CERIUM OXIDE NANOPARTICLES AS TUNABLE REDOX ACTIVE RADICAL SCAVENGERS

4.1 Introduction

Cerium oxide nanoparticles (CNPs) have shown tremendous potential for their use in various applications such as water gas shift catalysis, chemical mechanical planarization (CMP) and solid oxide fuel cells (SOFC)[1]. Recently, CNPs have been demonstrated to protect biological tissues against radiation induced damage, scavenging of superoxide anions, prevention of laser induced retinal damage, reduction of spinal injury, pH dependent antioxidant properties, prevention of cardiovascular myopathy, as tool for immunoassays and other inflammatory diseases[2a-2j]. In most of the biomedical applications it is speculated that nanoceria is a regenerative radical scavenger with the ability to regenerate the active Ce^{3+} oxidation state for radical scavenging which separates it from other nanomaterials based antioxidant systems such as hydroxylated and water soluble C-60 and SWCNTs[2k,2l]. Thus far there are no reports to control the regeneration of Ce^{3+} oxidation state which is the most important parameter in the application of CNPs as a reliable and regenerative radical scavenger. There is an imminent need to increase the potency of CNPs to achieve higher degree of protection against reactive oxygen species (ROS), to increase the residence time of CNPs in body and to control the regeneration of Ce^{3+} oxidation state. PEG has been reported to increase the residence time of nanoparticles and proteins inside cells and provide biocompatibility[3]. PEGylated counterparts of the Superoxide Dismutase (SOD) enzymes have shown improved performance over non-PEGylated enzymes[3]. Herein, we report our efforts to synthesize CNPs directly in polyethylene glycol (600 M.W) solution and determine the effect of increasing concentration of PEG (PEG vol % as 5, 10, 20, 40, 60 and 80) on the SOD mimetic properties exhibited by nanoceria. We also report how the active Ce^{3+} oxidation state can be regenerated or tuned to regenerate at faster rate. We further demonstrate the role of PEG on the redox chemistry of CNPs catalyzed by hydrogen peroxide.

4.2 Results and discussion

Several complexes of PEGs with lanthanides have been reported and characterized4. To evaluate the effect of PEG concentration on the complexation of cerium, UV-Vis spectra of the precursor salt of cerium (cerium nitrate hexahydrate) in different solutions of PEG were obtained (SI-1). It was observed that all PEG solutions show higher absorption relative to the water based solution of cerium nitrate but the observed non-specific trend could not be ascribed to a systematic decrease in the solvent polarity or dielectric constant.

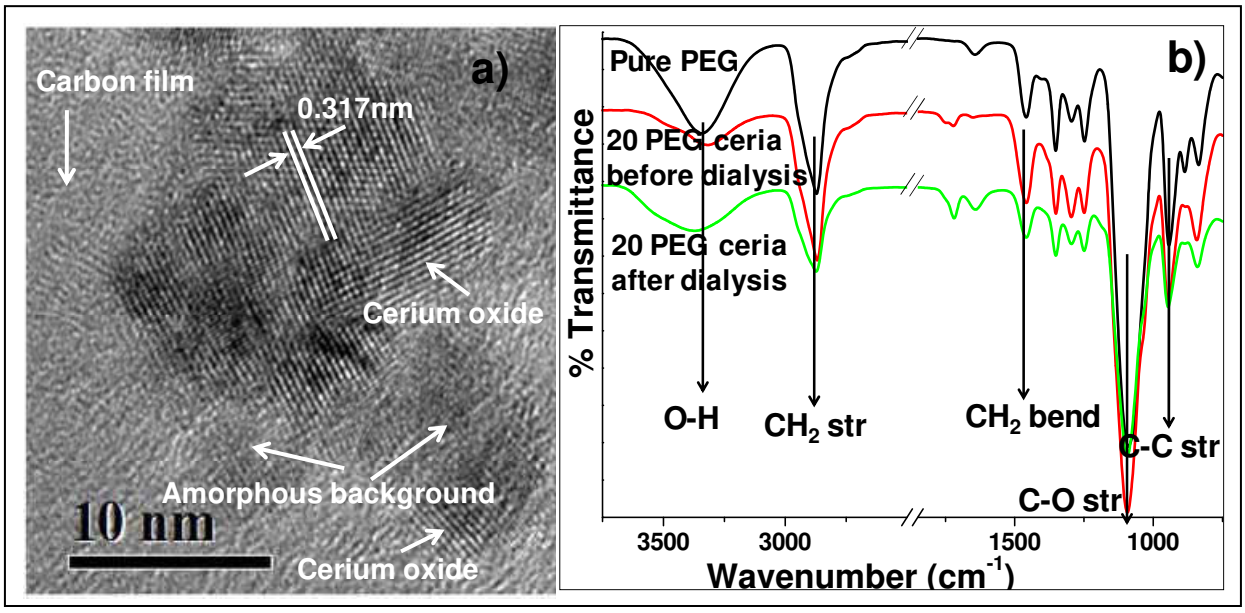

Figure 4-1: HRTEM micrograph depicting 3-5nm nanoceria crystals over amorphous polymer layer b) FTIR spectra of the PEG coated nanoparticles confirming the presence of PEG on nanoceria.

This observation can indicate the complexation of cerium ions with PEG in contrast to Uekawa et al[5] who reported a red shift upon addition of cerium nitrate in PEG however, they ruled out the charge transfer between Ce^{4+} and oxygen but ascribed the red shift in spectra to the complexation of PEG with cerium ions. The CNPs were synthesized as described in the experimental details (SI-2). High resolution transmission electron micrograph (Figure 1a) demonstrates that PEG is present as an amorphous layer on CNPs confirmed by an amorphous background around the

crystalline CNPs. To confirm further CNPs synthesized in PEG were dialyzed using a 3500 MWCO cellulose membrane and the FTIR spectrum was collected from the dried powder. Figure 1b confirms the presence of PEG on the nanoceria particles from FTIR. Only representative spectrum from 20% PEG solution is shown as all the PEG CNP samples provided similar features in the spectra.

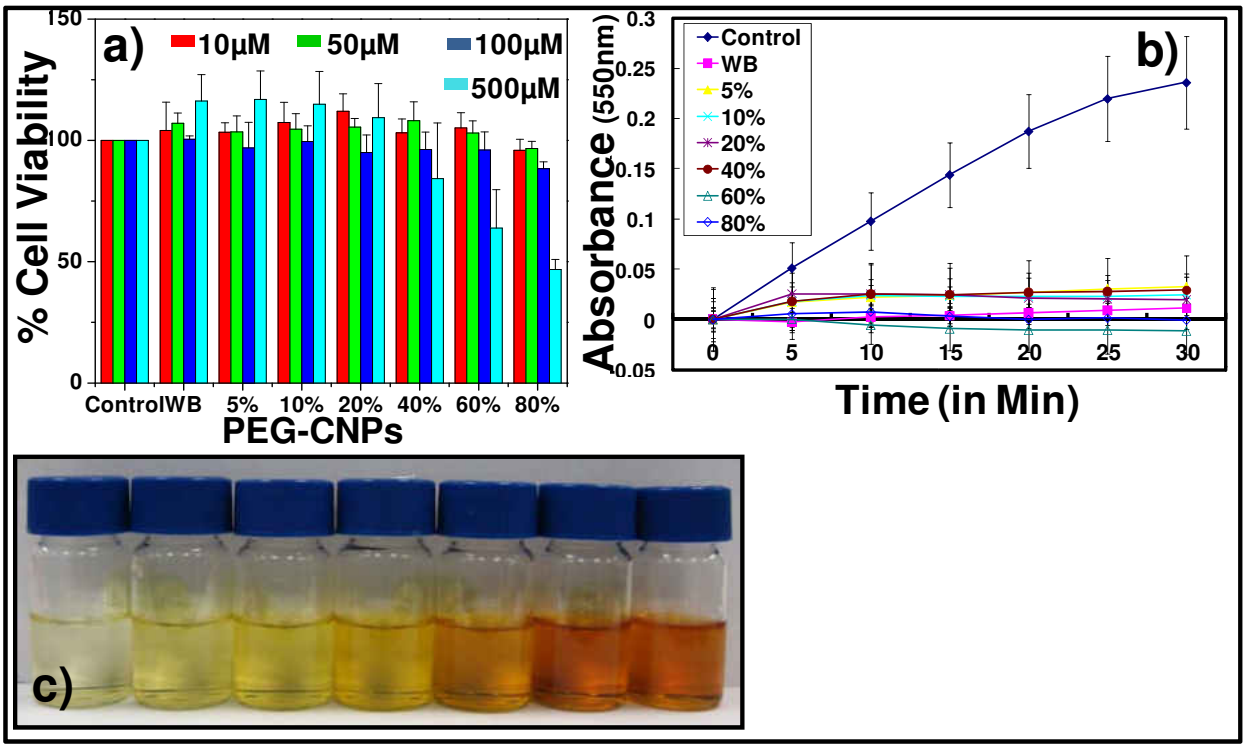

Figure 4-2: CNPs in different concentration of PEG a) MTT cell viability of CNPs for 72 hr b) superoxide dismutase (SOD) mimicking activity (y axis represents normalized absorbance) c) H_2O_2 induced oxidation of CNPs

4.2.1 Biocompatibility and SOD mimetic activity of CNPs in PEG

Cell viability analysis was performed for CNPs in PEG solution using standard MTT assay. PEG in molecular weights of 400 to 1500 daltons has been reported as benign in acute oral dose however, there are isolated reports of toxicity with increase in molecular weight and concentration[5]. It is clear from figure 2a (SI-3) that cell viability of CNPs in PEG, in a concentration as high as 100uM (for 72 hrs) was unaffected and the cells could thrive in presence

of PEG-CNPs. Our experiments reemphasize the benign nature of PEG by demonstrating excellent biocompatibility.

Significant progress has been made in past to mitigate the effect of ROS and have met with limited success in the form of CuZn SOD and their PEGylated counterparts[3]. It was shown recently that increasing the coating thickness of polymer (dextran) could reduce the activity of CNPs. In a similar study a decrease in peroxidase activity of magnetite nanoparticle was observed when the particles were coated with high molecular weight dextran or PEG molecules. To reduce the possibility of hindrance in the activity of CNPs at higher concentration of PEG (which may increase coating thickness); CNPs were synthesized specifically in low molecular weight (600 M.W) PEG and did not show significant differences in particle or agglomerate size (SI-4). As expected, the low molecular weight (figure 2b) PEG did not decrease the SOD mimicking activity of CNPs evaluated using classic SOD mimetic assay - competition with ferricytochrome C for reduction by superoxide radicals as a measure of concentration of radicals. Also, the activity was retained upon increasing the concentration of PEG over CNPs. While the activity of 60PEG based CNPs was maximum; the SOD mimicking activity did not vary much with the concentration of PEG suggesting that the SOD mimetic activity is independent of PEG concentration but may depend upon coating thickness achieved. Pure PEG controls showed no SOD mimicking activity (SI-5). The PEG coating can influence the redox characteristics of CNPs and thus could be a very potent candidate for radical scavenging in a biological setting with ability to tune the active 3+ oxidation state of cerium. We have previously demonstrated the ability of CNPs to prevent retinal degeneration using a rat model against radiation damage in the eye[2d], thus it will be very useful to synthesize CNPs in PEG solutions for its delivery as eye drops.

4.2.2 Hydrogen peroxide mediated redox cycling

Peroxide and superoxide mediated redox chemistry is central to the radical scavenging property of CNPs. Thus it is important to determine the changes in redox properties of CNPs in PEG solutions to evaluate the role of PEG coating on the redox properties of nanoceria. The regeneration ability of nanoceria sets it apart from all other ROS scavengers as it can regenerate the active Ce^{3+} oxidation state over time. At higher concentration of Ce^{3+} oxidation state, nanoceria forms a colorless colloidal solution (at 5 mM concentration) and the redox reaction can be monitored by change in characteristic UV absorbance and qualitatively through the visible changes in color. Nanoceria has been shown to protect hydrogen peroxide induced cell damage and can be used to demonstrate the regeneration of 3+ oxidation state. Thus to compare the redox chemistry of CNPs in different PEG solutions we monitored the change in oxidation state of CNPs as a function of time upon addition of equal amount of hydrogen peroxide to the CNPs samples. This redox procedure can briefly be summarized as: a) Addition of hydrogen peroxide oxidizes cerium in nanoceria from 3+ to 4+ oxidation state b) The acidic medium (pH 2.5- 3.5) around the nanoparticles favors 3+ oxidation state and thus upon aging the nanoceria undergoes surface reduction and regenerates its active 3+ oxidation state (with reduction of 4+ state) c) further addition of H_2O_2 to CNPs can repeat this cycle. Figure 2c shows the visible changes in color of the solution upon addition of equal amount of hydrogen peroxide to the CNPs prepared in various PEG solutions. The color change serves as a direct evidence of the reaction of CNPs with hydrogen peroxide. It can be noted that the color from the charge transfer intensifies and shows a red shift upon increasing the concentration of PEG from 0 – 80 volume percent. UV-Visible spectra depicts a primary peak at 298 nm corresponding to increase in Ce^{4+} species as shown in SI-6 (inset shows relative increase in absorbance with increase in PEG concentration). A secondary peak (appearing as a shoulder) was seen between 300-400 nm corresponding to the

charge transfer spectra between the oxidized cerium 4+ and the etheral oxygen (-CH_2O) from PEG. Figure 3a depicts the bathochromic shift with respect to concentration of PEG. It is clear that CNPs in 40, 60 and 80PEG solutions are red shifted as compared (maximum in absorption beyond 340 nm) to 5, 10 and 20PEG CNPs solutions.

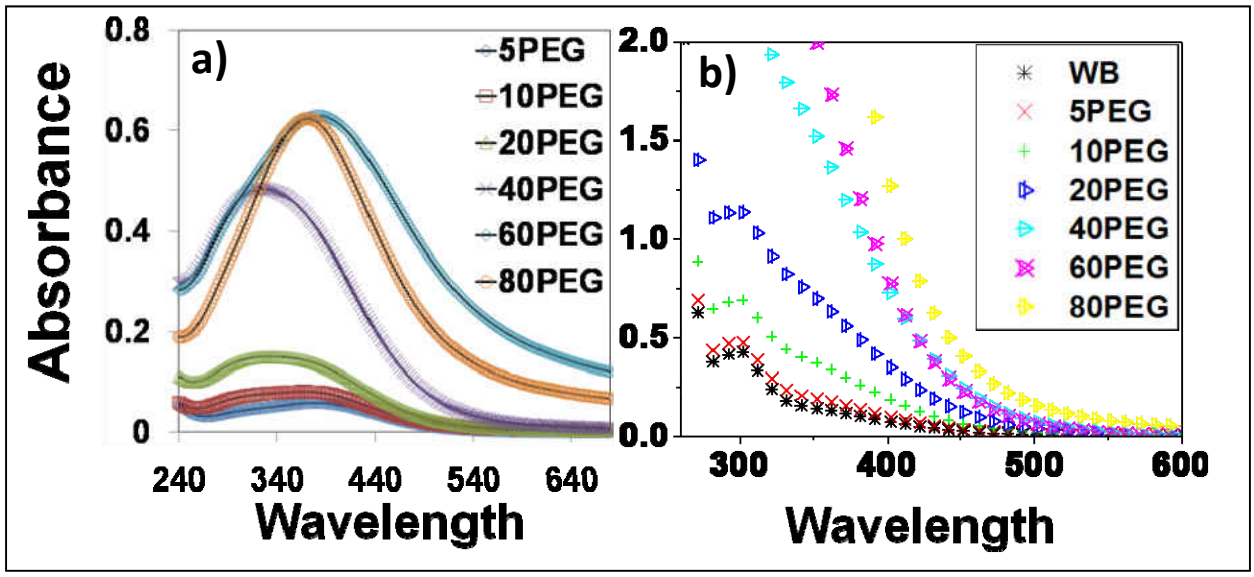

Figure 4-3: Bathochromic shift of PEG-CNPs corresponding to charge transfer species upon reaction with H_2O_2PEG-CNPs showed behavior peculiar to negative solvatochromism as the spectral values are red shifted with decrease in polarity of solvent b) UV-Vis spectra of CNPs in PEG solutions depicting reduction in amount of Ce^{4+} in different PEG solutions after 1 week.

It is known that the absorption of dyes and other absorbing species changes with polarity and dielectric constant of the solvent[8]. In general the spectra are red shifted upon increasing the polarity of the solvent while the spectra in Figure 3a are red shifted with decrease in the polarity of the solvent corresponding to negative solvatochromism phenomenon. The dielectric constant of PEG varies as 81, 77, 74, 67, 53, 39, and 25 for water, 5, 10, 20, 40, 60 and 80 PEG, respectively and the polarity of the solution is expected to decrease with similar trend. The red shift upon varying concentration of PEG suggests that two different charge transfer mechanisms occur from oxygen to cerium. The first being an internal charge transfer from oxygen to cerium

in CeO_2 (centered at 298 nm) and the second from the ethereal ($-CH_2O$) oxygen of PEG to cerium (centered around 320-400 nm). A non-specific trend in absorbance with concentration (or polarity/dielectric constant) of PEG suggests that the spectrum is not entirely solvent dependent but PEG associates to a different degree with CNPs. In addition to exhibiting different charge transfer, the regeneration of 3+ oxidation state of nanoceria in various PEG concentrations was monitored over time. Figure 3b depicts the UV-Vis spectra of CNPs in various PEG after 1 week of aging which shows disappearance of Ce^{4+} oxidation state. It can be noted that the regeneration of Ce^{3+} state of nanoceria is also a function of PEG concentration and is possibly induced by the stability of charge transfer complex. Investigations on the specific mechanism are under way and the possibilities have been described in SI-7. The UV-Vis spectra clearly depict that CNPs can be tuned to regenerate 3+ oxidation state faster or slower depending upon the requirement. A faster regeneration of 3+ oxidation state can reduce the time lag for nanoceria to be active repeatedly for radical scavenging. In addition to this the CNPs in PEG can have different amount of cerium in 4+ oxidation state depending upon aging time. This is particularly important as cerium 4+ oxidation state in CNPs can mimic the activity of enzyme catalase (data not published). The behavior of 20PEG solution upon aging for 28 days is shown in SI-8. It can be observed that the oxidation state of CNPs changes dynamically with time and by 21^{st} day the 3+ oxidation state (absorption max – 252 nm) was completely regenerated.

4.3 Materials and methods

4.3.1 Synthesis of PEGylated nanoparticles

CNPs were prepared in water and in different concentrations of PEG (600 molecular weight) solution. To evaluate the effect of PEG during synthesis of CNP and to determine what effect(s) the presence of PEG presence has on activity of CNPs the concentration was varied from 0 (vol%) PEG to 80 (vol %) PEG in water. Cerium nitrate hexahydrate (Sigma Aldrich) was

dissolved in PEG solution and allowed to digest for one hour. The pH of the solution was adjusted between 2.5 to 3.5 by the addition of 1N nitric acid (Sigma Aldrich). The solution was then oxidized using stoichiometric amounts of hydrogen peroxide (30 wt % Sigma Aldrich) to produced CNPs from cerium ions. At this point the samples were then aged for one month at room temperature and the solutions were monitored continuously for one month to maintain the pH below 3.5. The final solutions can be dialyzed to remove the excess acid and nitrates in the suspension. The CNPs with predominant Ce^{3+} are ready to use after aging of solution. The samples are labeled as WB (water based), 5PEG, 10PEG, 20PEG, 40PEG, 60PEG and 80PEG representing the increasing concentration of PEG volume percent (in water).

4.3.2 Fourier transform infra red spectroscopy (FTIR)

The coating of the CNPs with PEG was confirmed by FTIR. The samples were dialyzed against a 3500 (MW) cellulose membrane to remove excess and uncoordinated PEG from CNPs along with other ions. The sample was characterized before and after the dialysis using attenuated total reflectance (ATR) mode from the samples dried on KBr. Representative data from 20PEG is reported.

4.3.3 UV-Visible spectrophotometry

The UV-visible measurements spectral data was obtained using Varian Lambda 750 UV-VIS NIR instrument with a diffuse reflectance detector. All samples were characterized against a control PEG solution at the same concentration The UV-visible measurements were recorded from fresh and one day aged samples and after every seven days. UV-visible spectra were recorded for unoxidized cerium nitrate solution in PEG to account for the bonding of cerium ion with the PEG.

4.3.4 High resolution transmission electron microscopy (HRTEM):

High resolution transmission electron micrographs were obtained using FEI Tecnai F-30 microscope operated at 300 KV with a point-to-point resolution of 0.2 nm. The samples were prepared by depositing a drop of CNPs in PEG solution on a holy carbon coated copper grid. The TEM grids were dried overnight in vacuum before imaging. The Selected Area Electron Diffraction (SAED) patterns were recorded to confirm the crystal structure of CNPs.

4.3.5 SOD mimetic assay:

Xanthine oxidase and catalase were obtained from Sigma-Aldrich. Hydrogen peroxide and cytochrome C were purchase from Acros Organics (Geel, Belgium). Tris was obtained from MP Biomedicals (Solon, Ohio).

Reduction of Ferricytochrome C was used to measure the SOD mimetic activity of nanoceria (2c)(). Each assay was performed at room temperature for 30 min in a 96 well plate with a total volume of 100 μL.

All reactions were buffered with 50 mM Tris buffer (pH 7.5) and the rate of ferricytochrome C reduction was measured by following an increase in absorbance at 550 nm using a Spectramax 190 UV-Visible spectrophotometer (Molecular Devices, Sunnyvale, CA). Concentration of nanoceria was fixed at 2.5 μM for analysis of superoxide scavenging properties. All experiments were performed with 2000 units of catalase to eliminate any residual hydrogen peroxide that may react either with nanoceria or ferricytochrome C.

4.3.6 Cell culture:

For cultivation in a defined medium, a normal human keratinocyte (HaCat) cells (kind gift of Dr. Norbert Fusenig, German Cancer Research Center) were transitioned from defined keratinocyte medium (DKM, Invitrogen, Carlsbad, CA) supplemented with 10 % FBS to FBS deficient DKM

by 50% stepwise decrease in FBS concentration (5% FBS in DKM first passage, 2.5% FBS in DKM second passage and so forth). This gradual decrease in FBS conditioning allowed HaCat cells to grow optimally in DKM without serum, as direct transition to FBS deficient DKM resulted in cell death. HaCat cells were cultured in DKM with 10 µg/mL streptomycin and 10 IU/mL penicillin (Mediatech, Herndon, VA). The cultures were incubated at 37 ºC in a humidified 5% CO_2 atmosphere.

4.3.7 Cell viability assay

In order to determine the toxicity of PEG coated CNPs we utilized a normal human keratinocyte (HaCat) cell culture model in a defined keratinocyte medium (DKM, see above). In a typical experiment, 2,500 cells were seeded per well in a 96-well plate. Cells were allowed to adhere to well plate surface for 24hrs and PEG CNPs having concentration 10, 50, 100 and 500 µM in different percentage of PEG were added to and the cells were incubated for 24, 48 and 72 hrs. A tetrazolium dye, 3-[4,5-dimethylthiazol-2-yl]-2,5-diphenyltetrazolium bromide (MTT) was added (1.2 mM) and cells were subsequently incubated at 37 ºC in 5% CO_2 ion dark for 4h. To solubilize the dye, 100 µL of cell lysis solution (10% SDS, 5 mM HCL) was added to each well and the plate was incubated overnight at 37 ºC. Absorbance of the soluble dye was recorded at 570 nm using a SpectraMax 190 spectrophotometer (Molecular Devices). Cell viability was determined by dividing the absorbance of treated samples with untreated controls and reported as a percentage with error being the standard deviation from triplicate wells.

4.4 Summary

This confirms the hypothesis that coating of CNPs with PEG did not interfere with their redox property. Further, synthesizing CNPs in PEG have additional advantages of tuning the

regeneration kinetics. The regeneration of 3+ oxidation state of nanoceria was a function of PEG concentration thereby providing tunable CNPs with reversible oxidation state switching. CNPs synthesized in 5-40PEG showed a fast reversal of oxidation state and will be used in future investigations. CNPs synthesized in PEG offer a promising alternative to PEG-SOD as ROS scavengers and future studies will focus on in-vitro and in-vivo models. The specific interaction and degree of association of PEG with inorganic NPs will also be a focus of future studies.

4.5 References

1 a) Fu, Q.; Saltsburg, H.; Flytzani-Stephanopoulos, M. *Science* 2003, *301*, 935-938 b) Stambouli, A. B.; Traversa, E. *Ren. Sus. Ener. Rev.* 2002, *6*, 433 c) Andersson, D. A.; Simak, S. I.; Skorodumova, N. V.; Abrikosov, I. A.; Johansson, B. *PNAs 103*, 3518-3521

2 a) Tarnuzzer, R. W.; Colon, J.; Patil, S.; Seal, S. *Nano Lett* 2005, *5*, 2573 b) Heckert, E. G.; Karakoti, A. S.; Seal, S.; Self, W. T. *Biomat* 2008, *29*, 2705 c) Korsvik, C.; Patil, S.; Seal, S.; Self, W. T. *Chem Comm (Camb)* 2007, 1056 d) Chen, J.; Patil, S.; Seal, S.; McGinnis, J. F. *Nat Nano* 2006, *1*, 142 e) Das, M.; Patil, S.; Bhargava, N.; Kang, J. F.; Riedel, L. M.; Seal, S.; Hickman, J. J. *Biomat* 2007, *28*, 1918 f) Niu, J.; Azfer, A.; Rogers, L. M.; Wang, X.; Kolattukudy, P. E. *Cardiovasc Res* 2007, *73*, 549 g) Rzigalinski, B. A.; Meehan, K.; Davis, R. M.; Xu, Y.; Miles, W. C.; Cohen, C. A. *Nanomed* 2006, *1*, 399 h) Tsai, Y. Y.; Oca-Cossio, J.; Agering, K.; Simpson, N. E.; Atkinson, M. A.; Wasserfall, C. H.; Constantinidis, I.; Sigmund, W. *Nanomed* 2007, *2*, 325 (i) Atul Asati, S. S. C. K. S. N. J. M. P. *Angew Chem Int Ed* 2009 *48*, 2308 j) Perez, J. M.; Asati, A.; Nath, S.; Kaittanis, C. *Small* 2008, *4*, 552 k) Gharbi N.; Pressac M.; Hadchouel M.; Szwarc H.; Wilson S.R; Moussa F, Nano Lett, 2005, 5, 2578 l) Lucente-Schultz R. M.; Moore V.C.; Leonard A.D; Price K.B.; Kosynkin D.V; Lu M.; Partha R.; Conyers R.L.; Tour J.M., JACS, 2009, 131, 3934

3 a) Veronese, F. M.; Caliceti, P.; Schiavon, O.; Sergi, M. *Adv. Drug Del. Rev* 2002, *54*, 587 b) Yague, C.; Moros, M.; Grazu, V.; Arruebo, M.; Santamaria, J. *Chem Eng* 2008, *137*, 45 c) Williams, S. R.; Lepene, B. S.; Thatcher, C. D.; Long, T. E. *Biomacromol.* 2009, *10*, 155 d) Alcantar, N. A.; Aydil, E. S.; Israelachvili, J. N. *J Biomed Mat Res* 2000, *51*, 343 e) Chen, J.; Spear, S. K.; Huddleston, J. G.; Rogers, R. D. *Green Chem* 2005, *7*, 64

4 Rogers, R. D.; Zhang, J. H.; Bauer, C. B., J *Al. & Com.*1997, 249, 41

5 a) Uekawa, N.; Ueta, M.; Wu, Y. J.; Kakegawa, K. *Chemistry Letters* 2002, 854 b) Uekawa, N.; Ueta, M.; Wu, Y. J.; Kakegawa, K. *J of Mat Res* 2004, *19*, 1087

6 Shefel, VO, Indirect Food additives and Polymers, Migration and Toxicology. Lewis 2000, 1114

7 Gao, L. Z.; Zhuang, J.; Nie, L.; Zhang, J. B.; Zhang, Y.; Gu, N.; Wang, T. H.; Feng, J.; Yang, D. L.; Perrett, S.; Yan, X. *Nat Nanotech* 2007, *2*, 577

8 Bhattacharya, SC, Ray P, Moulik, SP, *J Photochem & Photobio*, 1995, 88, 139

4.6 Supporting Information

4.6.1 UV-Vis spectra of cerium nitrate in various concentration of PEG

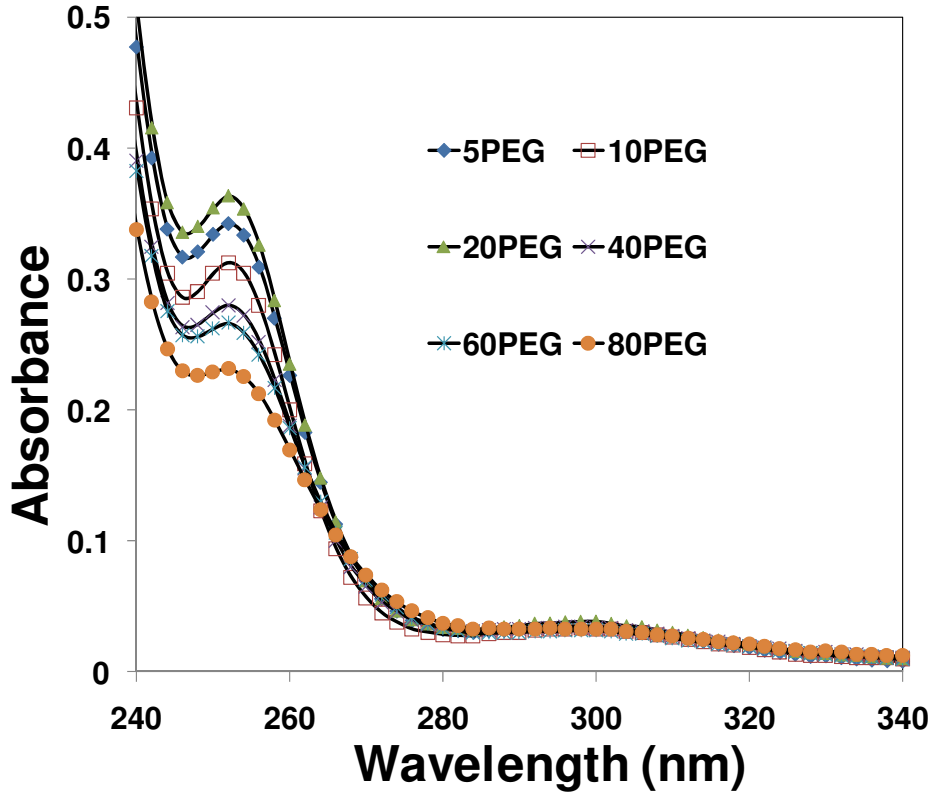

SI-1 UV visible spectra of cerium nitrate solution in various concentration of PEG. Increasing the concentration of PEG significantly alters the absorbance value at characteristic edge of Ce^{3+} (252nm) in nitrate. A non-specific change in absorbance value corresponds to association of PEG with cerium ions thereby either stabilizing or destabilizing the Ce^{3+} characteristic absorbance value

4.6.2 MTT cell viability

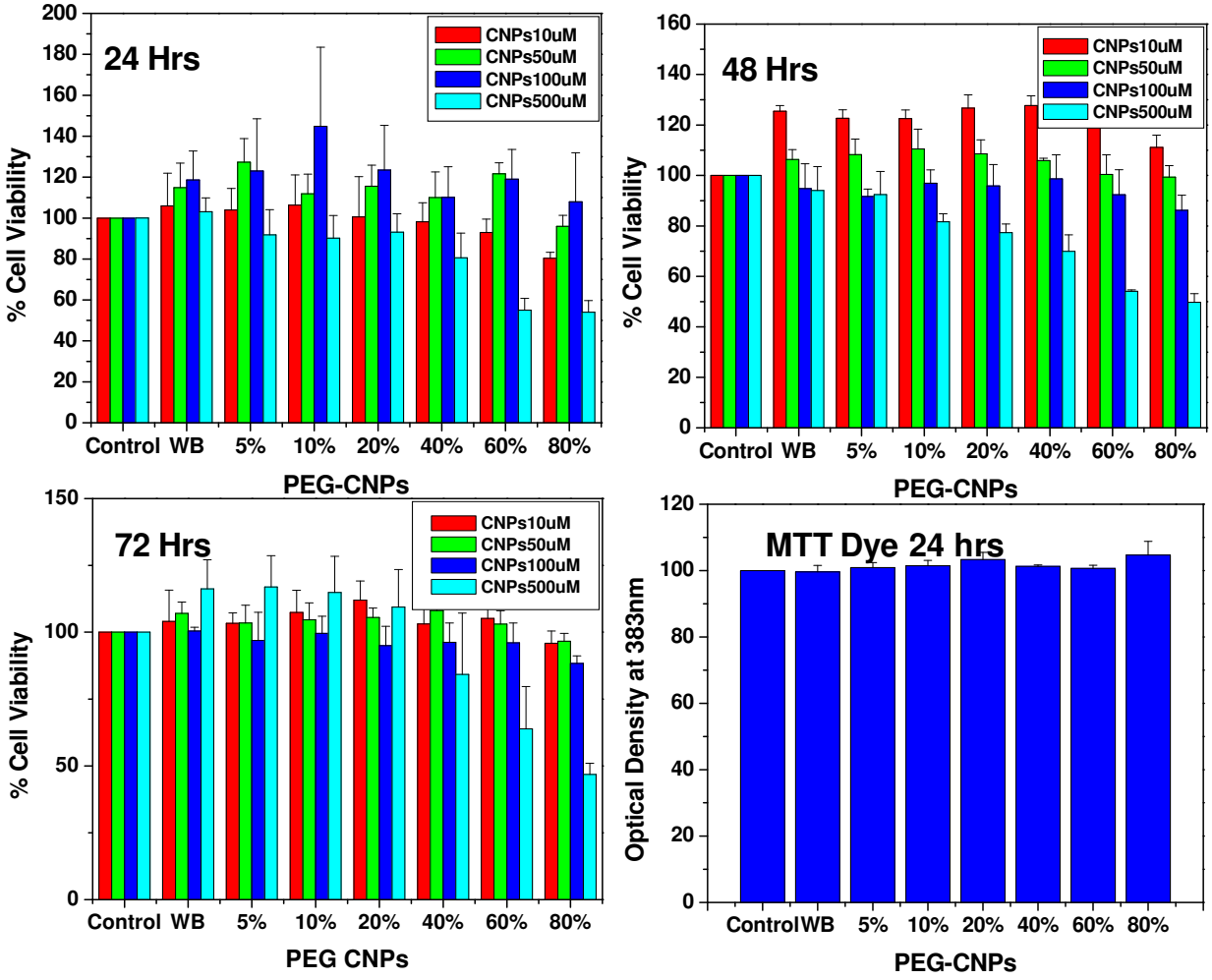

SI-3: The MTT cell viability analysis of PEG-CNPs shows concentration dependent toxicity at very high dose of 500uM for high concentration PEG. The time dependent analysis shows that the PEG-CNPs do not show any adverse toxicity in cells for a) 24 hours b) 48 hours and c) 72 hours for low concentration of PEG in PEG-CNPs. Slight toxicity can be seen for very high concentration of PEG upon exposure for 72 hours. The stability of MTT dye against the PEG-CNPs was determined by measuring the optical density (OD) of the dye at its characteristic absorbance at 383 nm. The measured OD of the MTT dye at 383 nm did not show any

significant changes. Thus it can be ascertained that MTT dye does not react with PEG –CNPs and is stable against any degradation or loss of activity due to adsorption.

4.6.3 Transmission electron micrographs of nanoceria in various PEG

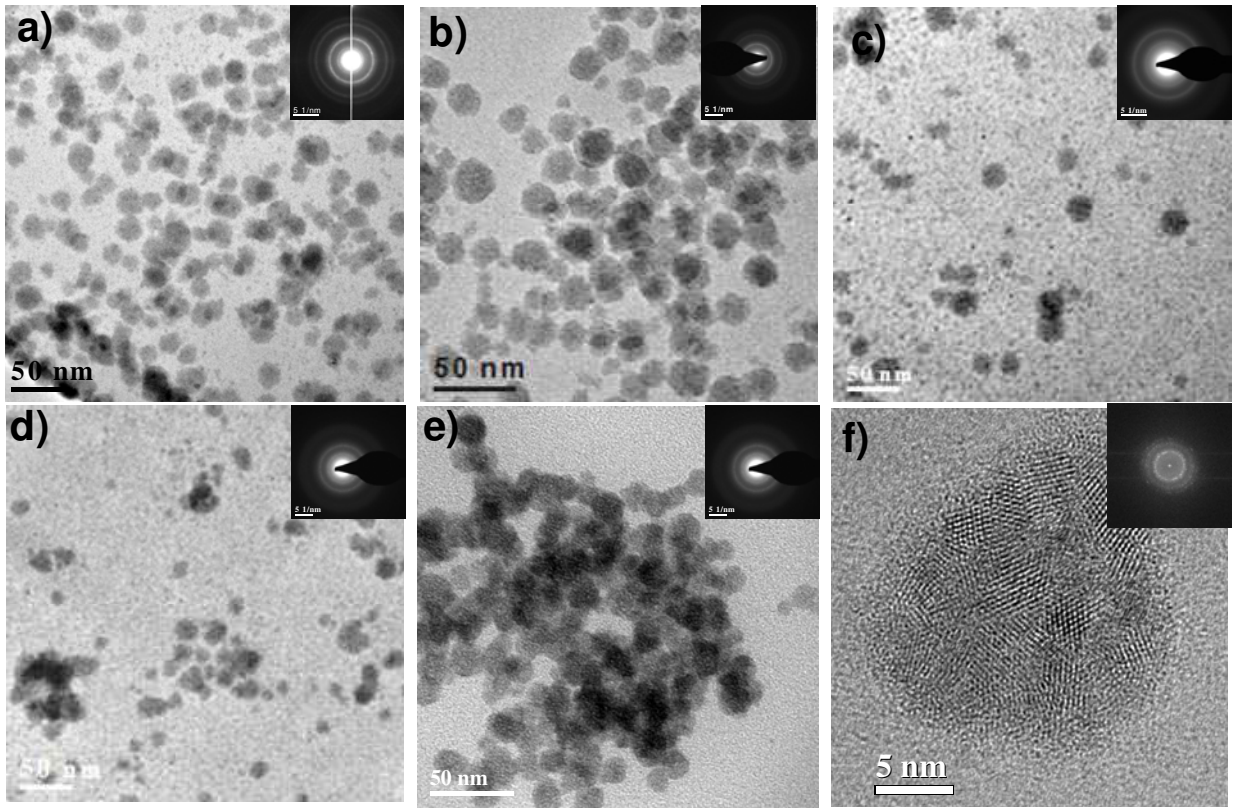

SI-4 High Resolution Transmission Electron Micrographs (HRTEM) of CNPS in a) 20PEG b) 40PEG c) 60PEG d) 80PEG e) Water (Corresponding SAED patterns as inset) f) High magnification image demonstrating the individual particle size of 3-5nm from 20PEG sample (Corresponding FFT pattern as inset).

4.6.4 SOD control for various PEG

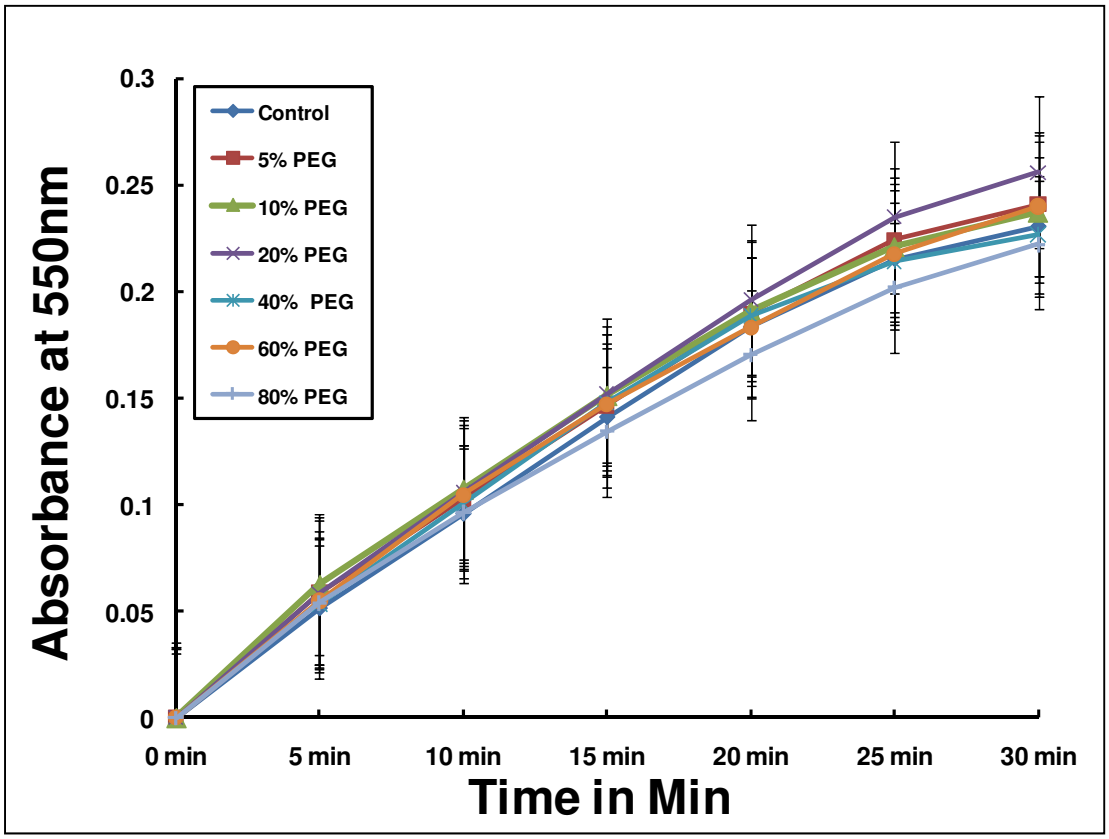

SI - 5: SOD mimicking activity of only PEG solutions depicting that PEG alone does not possess any SOD mimicking activity (y axis represents normalized absorbance).

4.6.5 *UV-Visible spectra of nanoceria in various PEG after addition of H_2O_2*

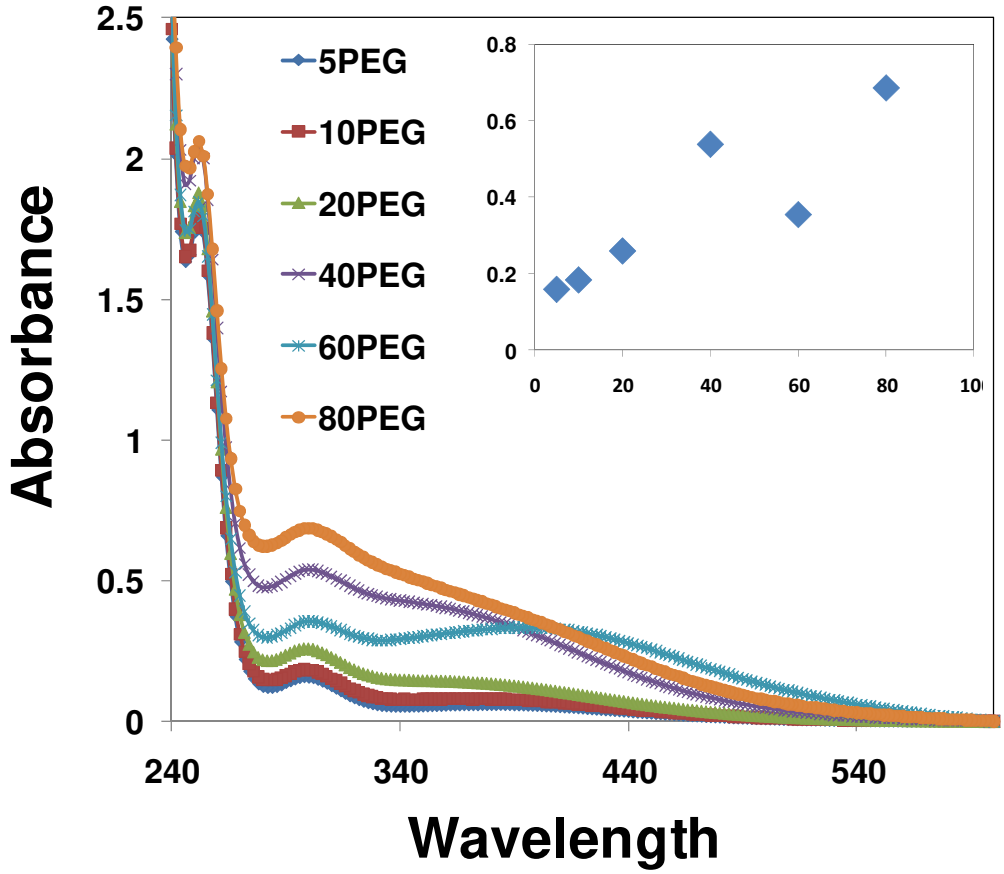

SI-6: The change in absorbance of nanoceria particles (5mM) in various concentration of PEG (5-80 vol%) after addition of same amount of hydrogen peroxide (Inset shows the relative increase in absorbance value at 298nm corresponding to increase in characteristic absorption of Ce^{4+}). Significant red shift corresponding to the formation of a charge transfer complex between 300 and 400nm could also be observed

4.6.6 Reaction of H_2O_2 with nanoceria

SI-7: Despite a number of attempts and benevolent users the mechanism of regeneration of cerium oxide nanoparticles is not yet known. Several publications over a period of several years can be found in the literature [J. W. Gryder and R. W. Dodson, ibid., **1951**, 73, 2890, The Journal of physical chemistry **1952**, 2266, Journal of the American Chemical Society, **1956**, 78, 1540, Journal of The American Chemical Society, **1957**, 79, 6353, The Journal of physical chemistry **1963**, 67, 201, Journal of European Ceramic Society, **1999**, 19, 1925, Applied Surface Science **2006**, 253, 1770, Journal of The Electrochemical Society, **2006**, 153, C74, Chemistry of Materials **2007**, 19, 2321] in this topic alone however, none of the article could solve the complete redox chemistry and/or were not related to nanoparticles. While the switching between various oxidation states of cerium has been described to a certain extent previously but, all the mechanisms were ascribed to cerium ions and occurred at very low pH(below 1.0). Recent literature has been more thorough in the interaction of cerium with hydrogen peroxide. Scholes et al (Chemistry of Materials, **2007**, 19, 2321) could show that the oxidation of Ce (III) to Ce(IV) occurs through formation of an intermediate compound, cerium oxy peroxo complex $CeO_2(OH)_2$ while Djuricic et al (Journal of European Ceramic Society, **1999**, 19, 1925) described this compound as $Ce(OH)_{4-x}(OOH)_x$ based on the thermogravimetric analysis. Even though both the work started with cerium ions and report the formation of complex after addition of hydrogen peroxide to cerium ions, we have observed the formation of this compound upon addition of hydrogen peroxide to grounded cerium oxide nanoparticles (below 20 nm) and aqueous suspension of CNPs. Scholes et al described that the peroxo complex forms in alkaline medium as

$$Ce(III) + H_2O_2 + OH^- \rightarrow CeO_2(OH)_2 \rightarrow CeO_2 + 1/2O_2 + H_2O$$

However we hypothesize that the oxidation of Ce(III) to Ce(IV) in nanoparticles from hydrogen peroxide occurs through a fenton type reaction which is sufficient to produce the required amount of hydroxyl ions to form the cerium peroxo complex. The aging of this complex in the aqueous acidic medium instead of aging in air decomposes the complex and regenerates the reduced oxidation state through internal redistribution of charge. The equations can be written as:

$CeO_{2-x} + H_2O_2 \rightarrow CeO_2 + 2OH^-$

$CeO_2 + 2OH^- \rightarrow CeO_2(OH)_2$

$CeO_2(OH)_2 \rightarrow CeO_2 + 1/2O_2 + H_2O$ (in air)

$2Ce^{IV}O_2(OH)_2 + 2H^+(aq) \rightarrow 2CeO_{2-x} + 3H_2O + (½ + x)O_2$ (in aqueous medium)

The participation of hydroxyl group in the regenerative process through the formation of a complex is strongly supported by the fact that a charge transfer complex forms between the PEG and the ceria nanoparticles in the presence of hydrogen peroxide. The is serves as a direct evidence of the involvement of PEG in the regenerative process and also affirms the findings of Scholes et al with respect to the formation of a cerium peroxo complex. We truly believe that the faster regeneration kinetics of nanoceria in PEG is linked to the ability of the terminal hydroxyl groups of PEG to take part in the cerium peroxo complex.

The evidence of faster regeneration of trivalent oxidation state in PEG hints at different mechanism being operative in aqueous medium under acidic conditions than in aerobic decomposition.

4.6.7 UV-Vis spectra of aged nanoceria

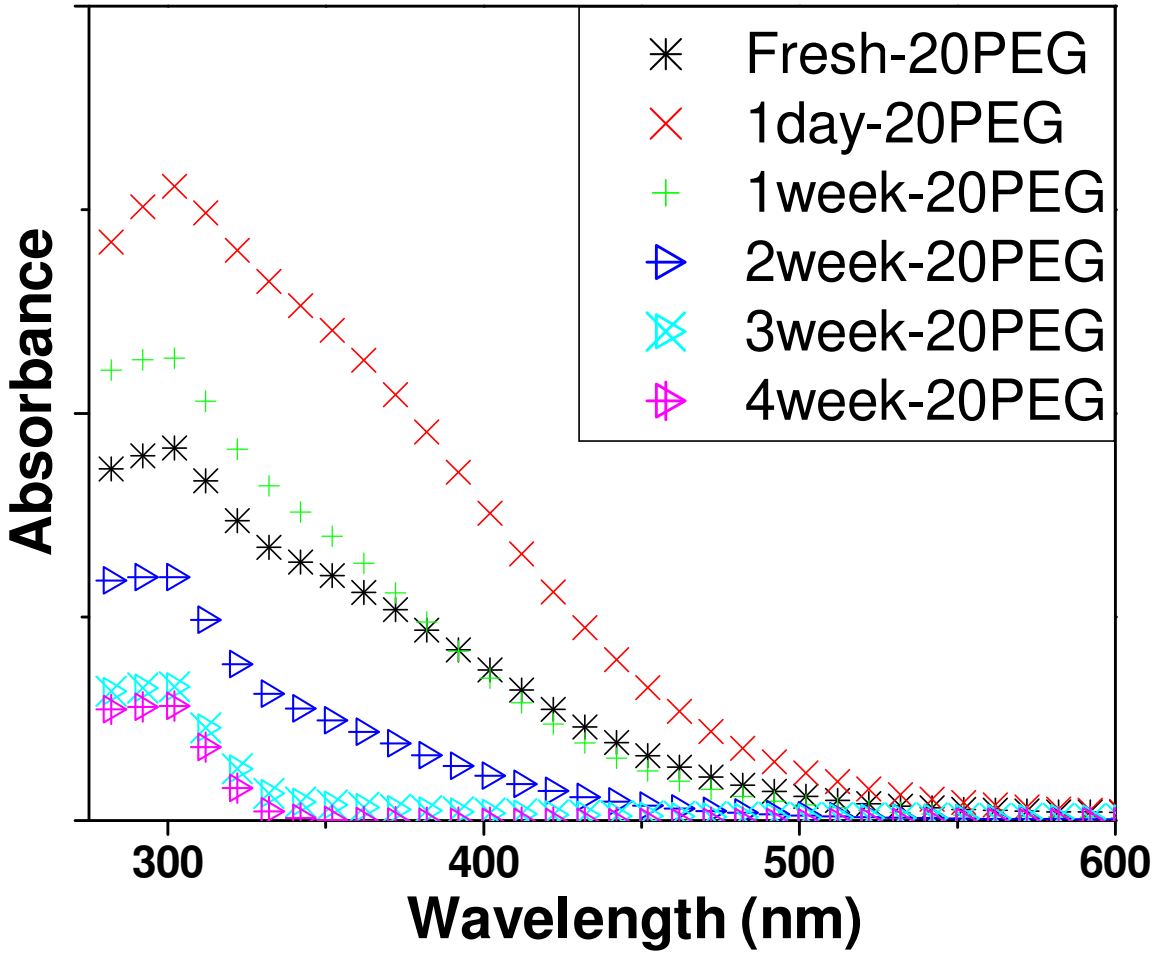

SI-8: UV-visible spectra of CNPs synthesized in 20PEG solution and aged for 4 weeks. It is observed that upon addition of hydrogen peroxide, the concentration of Ce^{4+} increases and reaches a maximum in 1 day. The aging of solution in acidic media causes reversal of oxidation state followed by a decrease in Ce^{4+} concentration and CNPs regenerates its predominant 3+ oxidation state within 3 weeks.

5 SYNTHESIS DEPENDENT CORE LEVEL BINDING ENERGY SHIFT IN THE OXIDATION STATE OF PLATINUM COATED ON CERIA-TITANIA CONTROLS THE ACTIVITY OF METHANOL DECOMPOSITION

5.1 Introduction

The development of alternative sources of energy has driven the research in energy sector for more than a decade. Promising alternatives have been proposed in form of polymer electrolyte membrane fuel cells that require hydrogen rich gas streams. Alcohols such as methanol and ethanol are currently being targeted as the hydrocarbon sources for production of hydrogen required in these fuel cells. Among several methods looked into the generation of hydrogen from methanol such as decomposition (MD) [1-4], steam reforming (SRM) [4-12], combined steam reforming (CSR) [4] and partial oxidation (POM) [13-18] of alcohols, the decomposition of methanol at elevated temperatures by noble metals supported on reducible and non-reducible oxide can be visualized as one of the simplest processes. The decomposition of methanol at elevated temperature over noble metals proceeds through the scission of C-H bonds and C-O bonds and is supposed to be less energy intensive and selective as compared to ethanol where a C-C scission is also required. However, this presumably simple decomposition can undergo various reactions (equation 1-4) depending upon the catalyst and the temperature of decomposition.

$$CH_3OH \rightarrow CO + 2H_2 \quad (1)$$

$$CO + 3H_2 \rightarrow CH_4 + H_2O \quad (2)$$

$$2CH_3OH \rightarrow CH_3OCH_3 + H_2O \quad (3)$$

$$CO + H_2O \leftrightarrow CO_2 + H_2 \quad (4)$$

Use of noble metals decreases the temperature of decomposition and increases the percentage decomposition of methanol obtained at specific temperature but suffers from poisoning effect of carbon monoxide produced as a byproduct of the reaction. Metal oxide as supports for noble metal catalysts have been researched thoroughly where the synergistic effect between the metal and the metal oxide have been shown to help lower the decomposition temperature of the oxide, improve the selectivity and minimize or completely remove carbon monoxide or water based poisoning of the supported catalysts [1, 2, 19-22]. Both reducible (alumina and zirconia) and non-reducible oxides (ceria and titania) have been studied as supports for decomposition of methanol using either Pd, Pt or Rh as the catalyst [22]. For the current system we have chosen ceria modified titania as the support oxide because of the improved catalytic performance of this mixed oxide as compared to ceria and titania only systems. In addition, the oxidation state of cerium in ceria modified titania is found to be trivalent thus forming a mixture of reducible (titania) and non-reducible (ceria) surface oxide. It was reported that for platinum, the decomposition of methanol proceeds via the cleavage of C-H bond to produce CH_2OH and that this scission is much more favorable than the scission of O-H bond due to the existence of a very high reversible barrier. The reaction proceeds through a second C-H bond scission followed by a quasi simultaneous scission of the C-H/O-H bond to form CO [2]. With respect to the activity of the metals, specifically platinum, it has been debated whether the pure metallic state or the oxidized form of platinum is more active in improving the performance and rate of catalysis [23-25]. It was shown that the reconstruction of Pt (110) structure into the oxide form results in improved oxidation catalysis of carbon monoxide [26]. DFT analysis by Pederson et al [27] confirmed this observation with respect to Pt (110) surface and it was also found that α-PtO_2 (0001) hexagonal basal planes remain inert for CO oxidation. In another

theoretical study it was found that α-PtO_2 forms on Pt (111) surface while PtO type stoichiometry is favored on Pt (100) surfaces. Although both PtO and PtO_2 were catalytically inefficient, the authors found Pt_3O_4 which formed at higher oxygen coverage, as more catalytically active [28, 29]. Hammer and Li [30] found a triple phase boundary of gas/metal/metal oxide to be much more active for the oxidation of carbon monoxide at Pt(111)/CO and α-PtO_2 phase boundary. Croy et al [20] reported that the oxidation state ($Pt^{\delta+}$) and particle size of platinum play more important role for methanol decomposition than the reducibility of the support. Xu et al [23] emphasized the fact that the oxidation ability of the Pt clusters is dependent upon the size of the clusters and can exhibit disparate activity as well as interaction with the support oxide using DFT calculations.
Herein we present further evidence that the activity of the platinum towards methanol decomposition is primarily affected by its oxidation state. We show that the synthesis method chosen for coating platinum particles over mixed oxide support can play a major role in determining the final oxidation state of the platinum. We compared the two most common methods of coating platinum, impregnation of platinum salt followed by thermal reduction and chemical reduction using sodium borohydride, over the oxide support. We show that the catalytic properties are a function of the synthesis and the oxidation state of platinum at fixed (3-5 nm) particle size over ceria titania mixed oxides and the poisoning of the catalyst is observed at higher metallic state of platinum.

5.2 Results and Discussion

5.2.1 Physical characteristics of the support and metal decorated catalysts

Metal oxides as catalyst support have been recognized as important components in the design and synthesis of modern catalyst systems. The mixed oxide system of ceria and titania was used as the supporting oxide. The co-precipitation based synthesis of the mixed oxide results in

synthesis of 5-7 nm crystallite of titania after calcination at 600°C as shown in figure 1 a and c. The SAED pattern in figure 1b matches with the anatase phase of the titania confirming the polycrystalline nature of the oxide. The XRD did not show any indication of the cerium oxide or mixed phase of ceria titanates upon calcination at 600°C which is consistent with the literature [32-39].

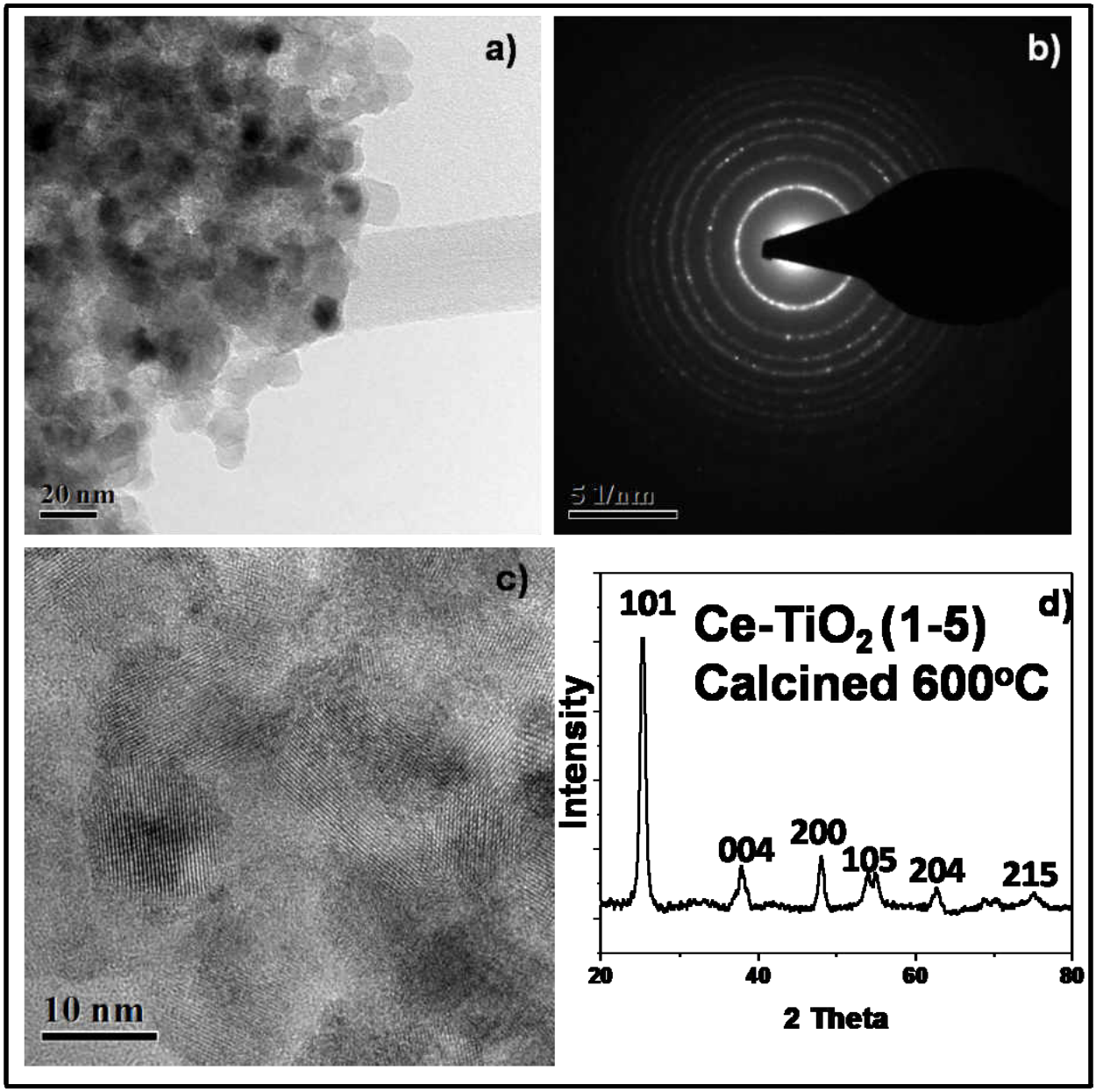

Figure 5-1 High resolution transmission electron micrographs (HRTEM) of mixed metal oxide (ceria –titania) after calcination at 600oC a) low magnification image depicting agglomeration tendency b) SAED pattern of titania confirming the polycrystalline nature of sample c) high magnification image confirming the individual particle of 7-10 nm d) The crystal structure of the mixed oxide was confirmed by X-ray diffraction which showed anatase as the only crystalline phase.

It has been shown that the presence of ceria helps to delay the onset of the rutile as well as anatase phase in titania and also helps to increase the temperature range over which anatase exists as stable phase [35, 36].

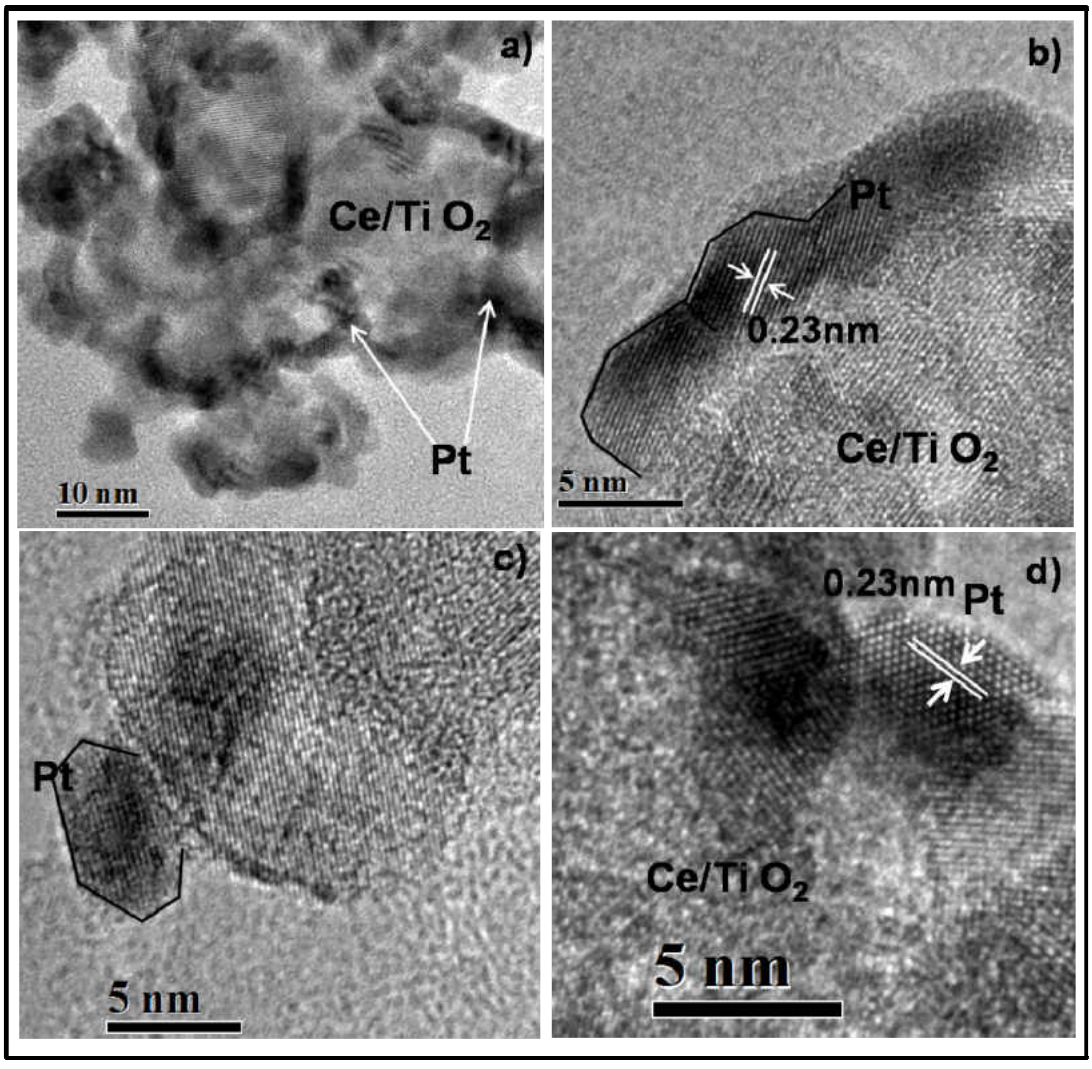

Figure 5-2 Transmission electron micrographs of sample PTCR shows 2-4 nm platinum nanoparticles formed upon chemical reduction of platinum chloride a) low magnification b) high

magnification clusters of three nanoparticles c) faceted geometry of the platinum nanoparticles high magnification image confirming the interplanar spacing of Pt.

It has also been hypothesized that cerium oxide is present as an extremely diffuse phase over the grain boundaries which also helps in preventing the coarsening of the particles at elevated temperatures and the onset of rutile phase [35, 36]. Recently, in a theoretical investigation, superior catalytic activity of $M/CeO_2/TiO_2$ system in water gas shift catalysis was reported [40]. No indications of ceria being doped in the titania lattice was observed as confirmed by the absence of any shift in the XRD pattern of the ceria titania with respect to only titania (not shown). The high magnification image in figure 1C shows lattice fringes of the titanium oxide nanoparticles along with few amorphous particles this could indicate that there are particles out of the plane of focus or that the is a presence of partially amorphous titania or ceria sample. The BET surface area of the as synthesized powders was 410 ± 3 m^2/g and reduced to 83 ± 4 m^2/gm upon calcination at 600 ^oC for 3 hours.

The coating of metal oxides with 1% platinum did not modify the particle size of the mixed oxides. Coarsening of particle size of platinum was reported previously on the cerium oxide supports [22]. Such coarsening was not observed in present experiments however it is possible that the relatively lower atomic concentration of the cerium is not sufficient enough to cause the coarsening of the Pt nanoparticles. Figure 2 a-d shows the TEM images of the 1% Pt coated ceria titania synthesized by the chemical reduction of platinum (PTCT) after adsorption. The Pt nanoparticles were distributed as 3-5 nm particles which are larger than the sizes reported by Croy et al [20, 22]. The Pt nanoparticles formed after chemical reduction appears elliptical and/or faceted. The particle size of the mixed oxide did not change after the process of reduction making it difficult to identify the Pt nanoparticle dispersed in ceria titania matrix. Surprisingly the particle size of the Pt nanoparticles synthesized from the chemical reduction followed by

calcination was in the similar range of 3-5 nm. Figure 3a-d shows the size of the platinum nanoparticles synthesized by the chemical reduction (PTCR) method and calcined at 500^{o}C for 2 hours. However the geometry of the nanoparticles is more spherical as compared to the non-calcined nanoparticles which suggest volume redistribution in the Pt nanoparticles during the process of calcination.

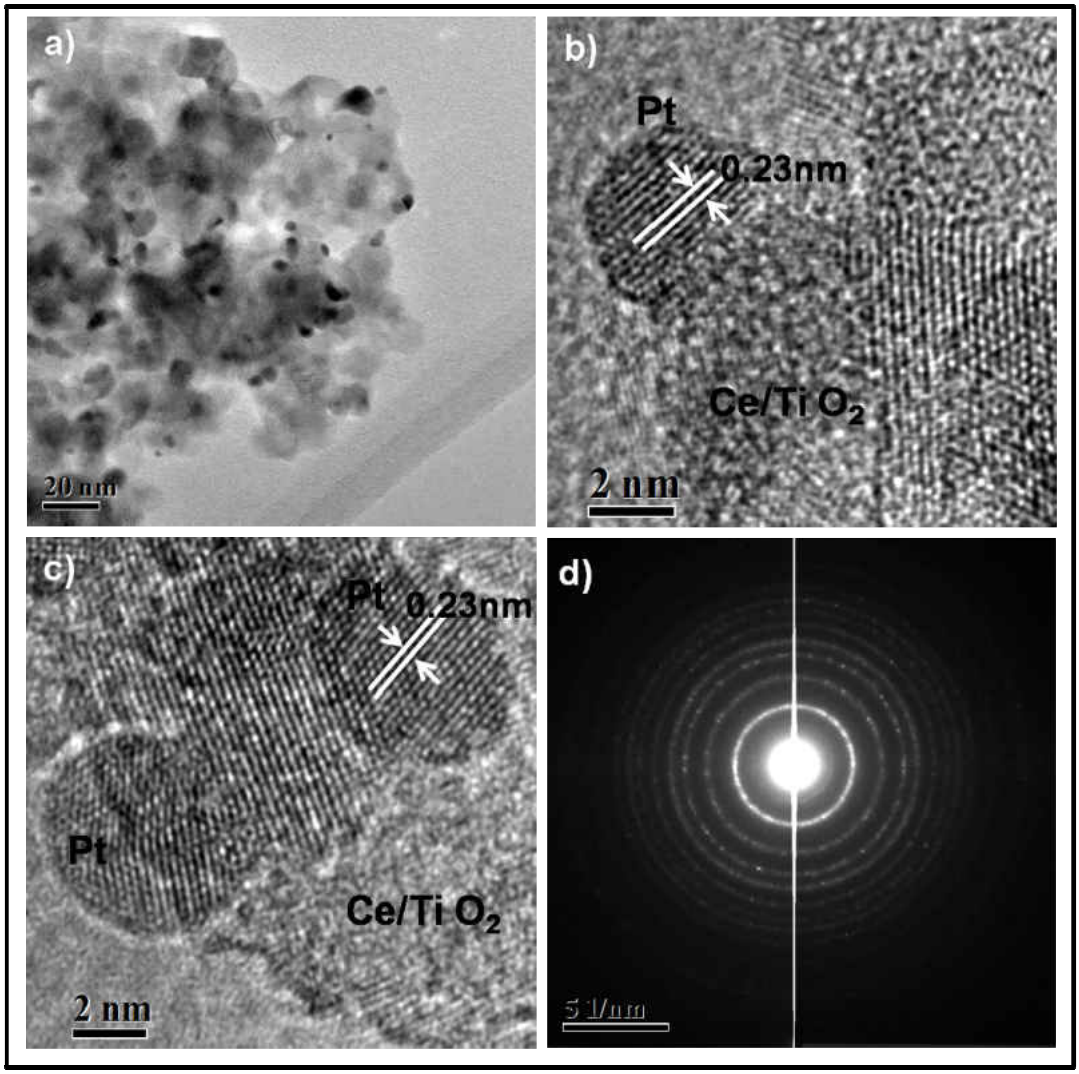

Figure 5-3 Transmission electron micrographs of sample PTCR-T shows that the particle size of platinum does not change upon calcination at 500C over ceria titania mixed oxide support a) low magnification image b) high magnification image c) spherical geometry of the platinum nanoparticles d) selected area electron diffraction confirming the polycrystalline nature of the mixed oxide.

The particle size and shape of the Pt nanoparticles synthesized by thermal reduction (figure 4 a-c) were identical to the calcined sample. The highly dispersed nature of Pt nanoparticles on the surface of oxide prevented further agglomeration during the calcination however, the possibility of support effect in pinning the coarsening of nanoparticles cannot be ruled out.

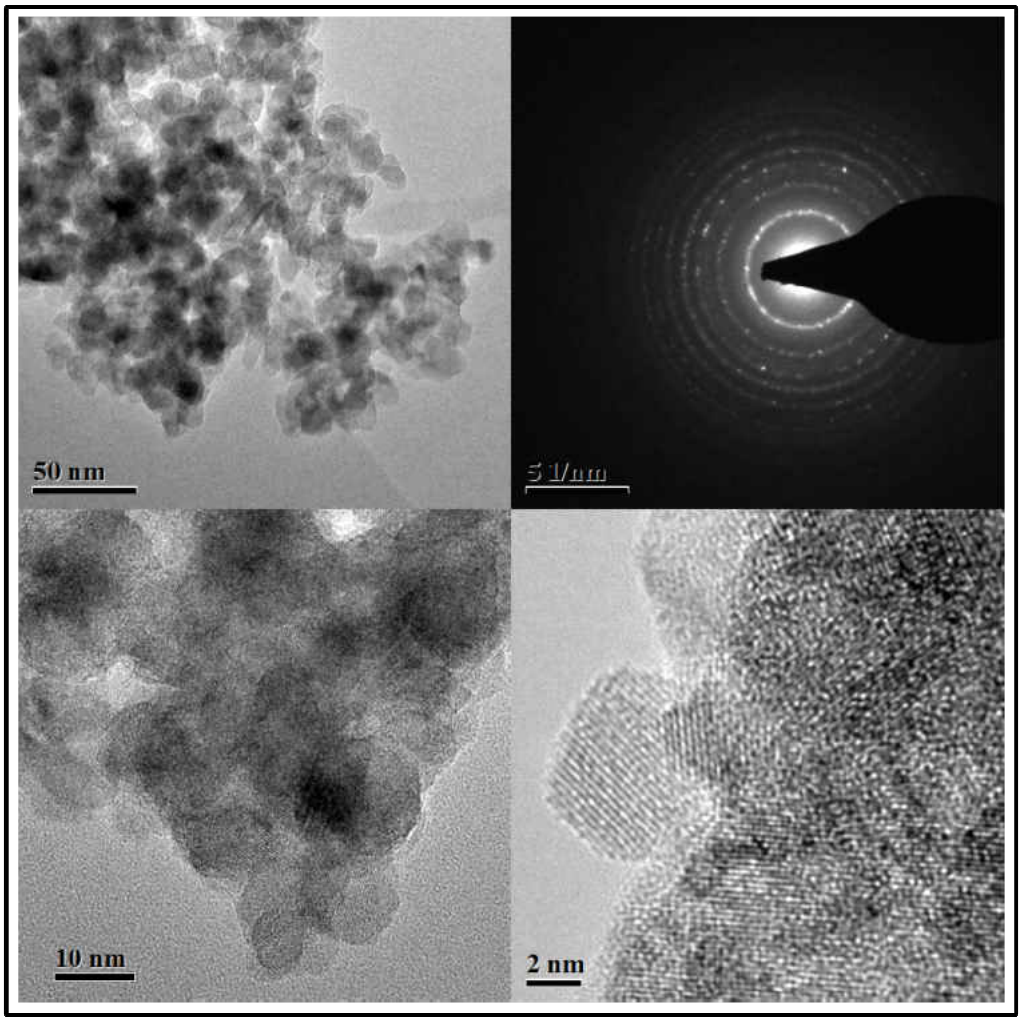

Figure 5-4 Transmission electron micrographs of sample PTCT over ceria titania mixed oxide support a) low magnification image b) selected area electron diffraction confirming the polycrystalline nature of the mixed oxide c) high magnification image depicting that the particle size of the base oxide is unaltered d) high magnification image depicting 5 nm platinum (111) nanoparticles.

Surprisingly, no indication of a top oxide coating was evidenced by the TEM even though the samples showed a high degree of oxidized platinum (as discussed in following sections). The

surface area of Pt modified nanoparticles did not show any significant change as compared to the base value of 84 m^2/g for 600°C calcined sample which can be attributed to the fact that the particle size of as-synthesized powders is 5-7 nm and the modification by 1% coating of 3-5 nm platinum nanoparticles would not produce a significant change.

5.2.2 Activity and selectivity of the catalysts

The activity of different catalysts at various temperatures is plotted in figure 5a. It was observed that the catalyst prepared by thermal decomposition of platinum over the mixed oxide catalyst (PTCT) outperformed the catalysts prepared by the chemical reduction of the metal. The onset temperatures of the PTCT and PTCR were around 175 – 200°C while the onset temperature of the PTCR-T sample was around 200 - 225°C.

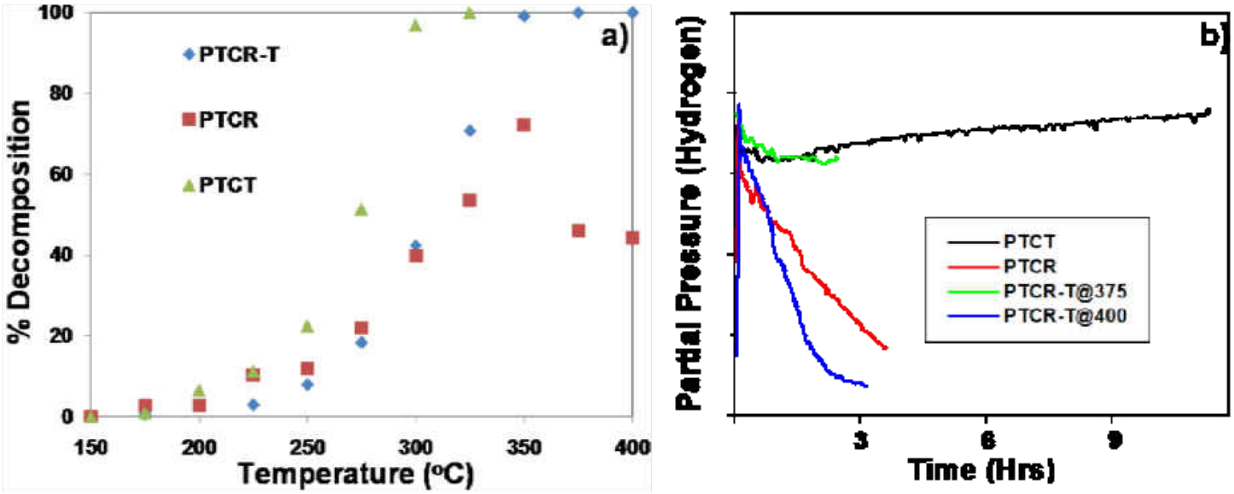

Figure 5-5 a) The activity of Pt modified ceria titania catalysts for decomposition of methanol at various temperatures b) the poisoning behavior of the catalysts is depicted by change in the partial pressure of hydrogen as a function of time. The catalyst PCTT displayed no signs of toxicity even after 11 hours while the samples prepared by chemical reduction of Platinum (PCTR and PCTR-T) displayed very fast poisoning behavior.

The decomposition of methanol in all the samples proceeded with production of only CO and hydrogen. No additional gases such as methane or carbon dioxide were detected in the mass spectrometer for the temperatures range covered in this study. It has been shown that the

catalytic decomposition of methanol over Pt supported on ceria or plain ceria (no noble metal catalyst) produces carbon dioxide as one of the byproducts [1, 22]. As the crystalline features corresponding to cerium oxide were not identified in the as synthesized catalyst, it can be assumed that the support oxide effect was mainly influenced by the presence of titanium oxide and not cerium oxide thus eliminating the production of carbon dioxide. The activity of the catalysts increased with increase in temperature. Even though the sample PTCR showed some activity in the lower temperature, the activity did not improve significantly with temperature as this catalyst reached only 50% efficiency at 325^{o}C. The catalyst (PTCR) failed to reach 100% conversion even upon increasing the temperature up to 400^{o}C and demonstrated heavy poisoning as shown in figure 5b. It was observed that at this temperature trace amounts of water was also produced and that the production of water significantly and rapidly poisons the catalyst in presence of carbon monoxide. The calcination of this sample at 500^{o}C improved the performance of the catalyst (PTCR-T) showing classical S- shaped kinetics with increase in decomposition of methanol at as the temperature was increased with conversion efficiency in excess of 90% at 350^{o}C and 375^{o}C. The catalyst PTCR-T showed 100% conversion at 400^{o}C however, at this temperature the catalyst poisoning was very rapid similar to the poisoning observed for uncalcined sample (PTCR). Interestingly the catalyst PTCR-T showed very slow poisoning at 375^{o}C for at least 3 hours but the conversion efficiency at this temperature was around 95%. As soon at the temperature was increased to 400^{o}C the poisoning of the catalyst poisoning occurred within a few minutes (Figure 4b) of increasing the temperature to 400^{o}C. It was also noted that even though the calcination of PTCR sample improved the overall conversion efficiency, it reduced the activity of the catalyst in the lower temperature range. This also suggests an increase in the energy barrier for decomposition of methanol by the PTCR-T sample which resulted in

increasing the onset temperature for methanol decomposition. In contrast, the PTCT catalyst demonstrated excellent catalytic behavior as the decomposition of methanol increased rapidly with increase in temperature.

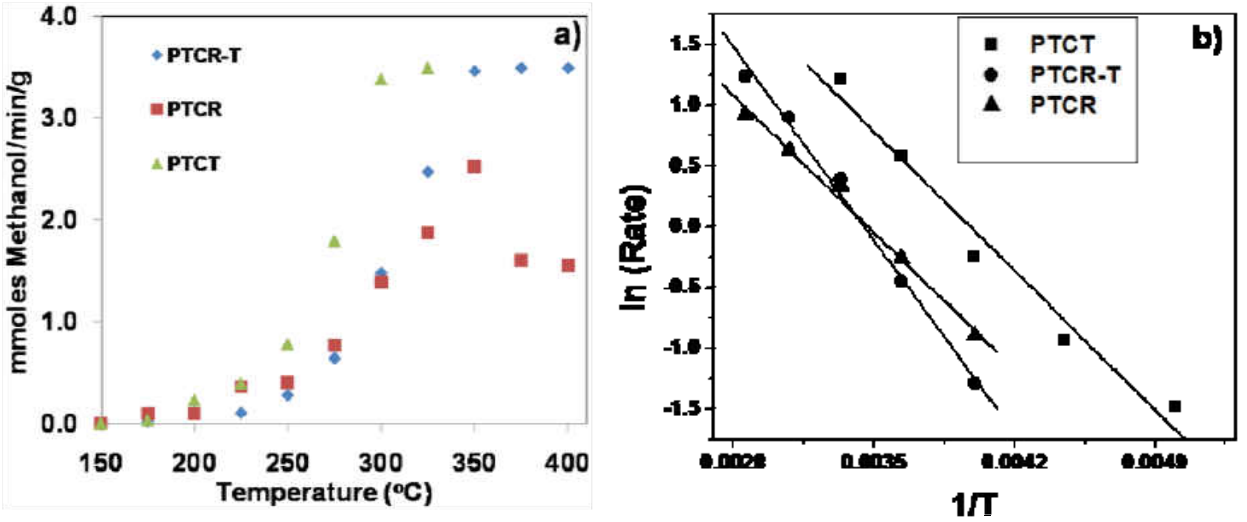

Figure 5-6 The rate of decomposition of methanol of various catalyst at various temperatures shows both PCTT and PCTR-T decomposed 100% of methanol (3.5mmol/min/g of catalyst) flowing through the reactor b) the Arrhenius plots for the decomposition of methanol as a function of temperature. For Arrhenius plots the temperature range for PTCT was chosen as 175°C to 300°C while for PTCR and PTCR-T the temperature range under study was from 275°C to 350°C.

The complete conversion of 3.5mmoles of methanol/ minute/g of the catalyst was achieved at 300°C. It was observed that the temperature for 100% conversion of methanol was higher than the values reported in literature [1, 4, 20, 22, 41-49] but our rate of flow of methanol is significantly higher with respect to the catalyst loading and the amount of noble metal on the supported oxides which could result in reduced activity of the catalyst at lower temperatures. The catalyst loading of 50mg in present study is lower than the mostly reported data in the literature (100-300mg) but have significantly higher conversion rate of methanol [20, 22, 41-43, 46-49].

The rate of conversion of methanol for various catalysts is depicted in Figure 6a and it can be observed that both the catalysts PTCR and PTCT decomposed methanol at a very high rate of

3.5mmoles of methanol/minute/g of the catalyst. Arrhenius plots were constructed by plotting the natural log of rate of decomposition of methanol against (1/T) and are depicted in figure 5b. It must be mentioned that the values of ln (R) for PTCR and PTCR-T was plotted only in the range of 250^{o}C to 350^{o}C and the values were neglected in the lower temperature range to obtain the best fit. The values activation energies were calculated from the plot and are 13.06 KJ/mol, 13.67 KJ/mol and 19.21 KJ/mol for PTCT, PTCR and PTCR-T. As expected from the decomposition plots the activation energy is lowest for PTCT followed by PTCR and highest for PTCR-T suggesting that the decomposition of methanol is favored on thermally prepared noble metal catalyst on mixed oxide support.

5.2.3 Chemical oxidation state of platinum and oxide support

The x-ray photoelectron spectroscopy was used to ascertain the relative changes in the oxidation state of the Pt, Ce and Ti. The modification of support oxides with platinum did not change the characteristics of the support oxide material. Figure 5 shows the XPS spectra of cerium 3*d*, titanium 3*p*, carbon 1*s* and chlorine 2*p* level. It can be observed that the XPS spectra do not show any significant differences between the samples coated with platinum. No trace of residual chlorine was observed in the XPS peak indicating the complete removal of chlorine during organometallic decomposition to the metal. A high resolution scan was required to observe the Ce 3*d* spectra which demonstrated that cerium is predominantly present in trivalent oxidation state by the absence of characteristic 917eV satellite peak for Ce^{4+}. It has been shown previously that at low atomic concentration of cerium in a mixture of ceria-titania, cerium is predominantly present in trivalent oxidation state. The presence of reduced cerium on the surface changes the behavior of support oxide from reducible to partially non-reducible. The XPS spectra of platinum 4*f* level depicts different percentage of Pt(0) for different treatment of platinum. The thermally reduced platinum (PTCT) showed the highest mixture of mixed oxidation states of platinum with

Pt(2) as the predominant oxidation state. The position of the Pt(0) peak was shifted to higher binding energy for PTCT relative to the pure metallic platinum while the Pt(0) peak for PTCR and PTCR-T was shifted to lower binding energy relative to pure metallic titanium.

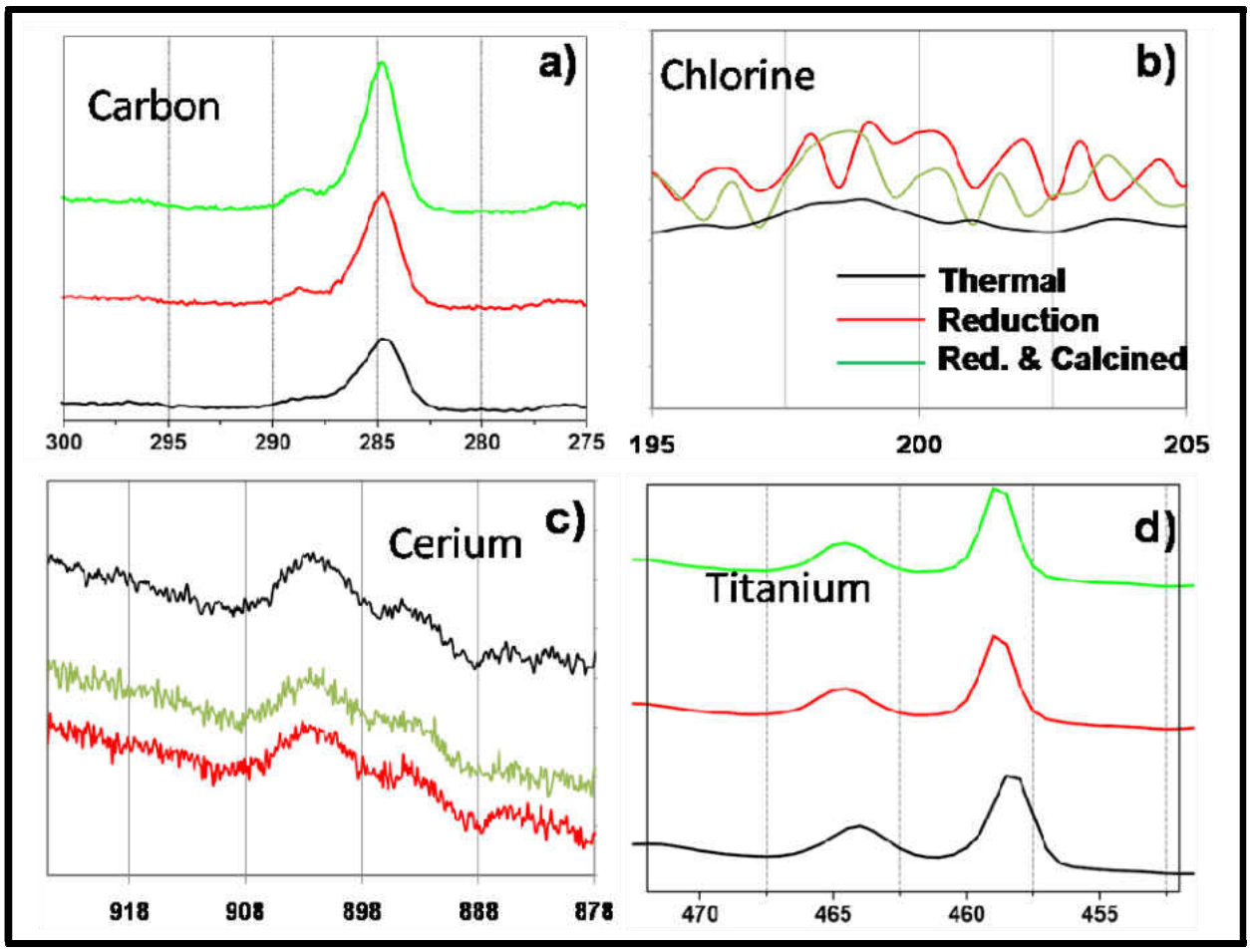

Figure 5-7 X-ray photoelectron spectroscopy plots confirming the presence and absence of various chemical species on the ceria tiania surface before and after coating the surfaces with platinum a) carbon 1s peak for peak referencing b) chlorine if present could not be detected in the XPS depicting the complete reduction of the hexachloroplatinum to platinum nanoparticles c) cerium 3d shows the absence of characteristic 917eV satellite peak confirming that cerium is predominantly present in reduced trivalent oxidation state d) titanium 3p level shows no change after various treatment of catalyst

This shift towards the lower binding energy is consistent with the previous report [20]. Such large shift towards lower binding energy of Pt 4f core level peak was also reported by Dauscher et al [50] under reducing conditions over ceria titania mixed oxide surface. It was observed that

under various annealing treatment of platinum supported over bulk ceria-titania mixed oxide, the Pt 4*f* peak showed various shift and was shifted to values as low as 70.3 eV upon annealing in hydrogen gas at 450^{o}C.

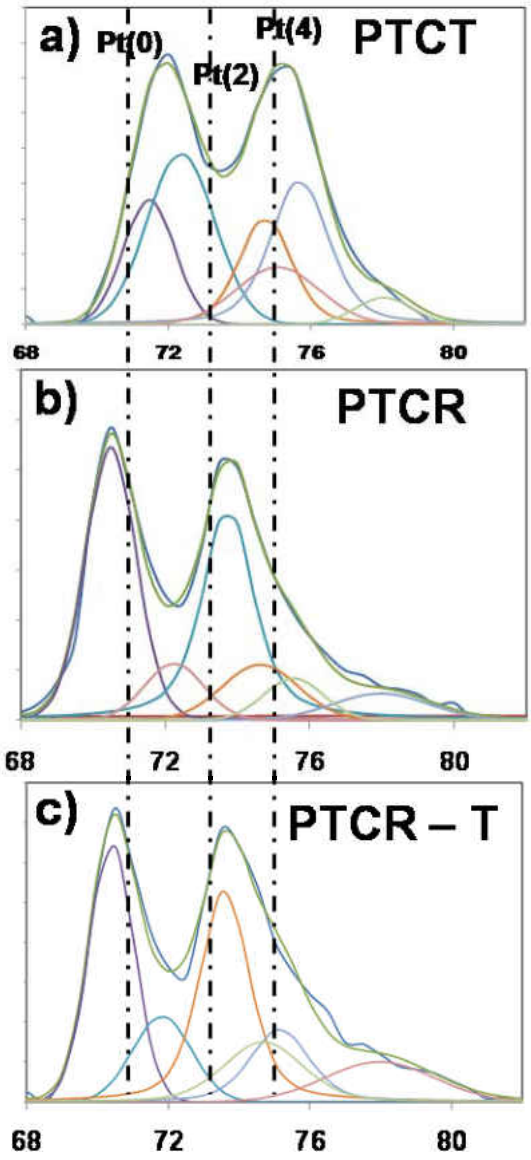

Figure 5-8 The XPS spectra for platinum after reduction over the ceria titania supports following the peak fit assignments a) PTCT shows mixed oxidation states with Pt(2) as the major component b) PTCR sample shows Pt (0) as the major component c) the calcination of the sample PCTR marginally increases the concentration of mixed oxidation states.

The shift towards lower binding energy suggests a charge transfer from the oxide support to the metal under the reducing atmosphere thereby facilitating the removal of the binding electron from platinum. In contrast the shift in the Pt (0) peak towards higher binding energy in PTCT can be attributed to a limited interaction between the metal and the support during the reduction process. This shift is only 0.2eV and the marginal shift is under the limit of experimental and instrumental accuracy. The fact that the metallic platinum peak was not shifted towards lower binding energy in the case of thermally reduced platinum also suggests that the catalysts will behave differently towards methanol oxidation. It is unclear whether the faceting of nanoparticles as observed in thermal reduction process or the slow decomposition of platinum as opposed to the fast chemical reduction is responsible for opposite shift in the core level binding energy of metallic.

The calcination of PTCR sample resulted in increasing the relative amount of oxidized platinum and also resulted in improving the catalytic efficiency of the catalyst. It can be noted from figure 6b and 6c that both the Pt(2) and Pt(4) peaks were also shifted to lower binding energy as compared to pure PtO and PtO_2. While the calcination at 500^oC increases the relative percentage of oxidized platinum it did not induce any shift in the position of the Pt 4*f* peaks as compared to the non-calcined sample. In contrast Pt (2) was the predominant form of platinum in the sample prepared by thermal reduction of platinum.

A comparison of the activity of catalysts towards methanol decomposition with the results from the XPS spectra suggests that the oxidized form of platinum is more active for the decomposition of methanol over mixed ceria titania as the supports. This observation adds to the controversy in the open literature about the role of the oxidation state of platinum towards its catalytic activity. The fact that we could produce similar sized Pt particles over the same support with different

oxidation state is very important contribution and may be used as an experimental evidence for higher activity of oxidized platinum at least in the decomposition of methanol. The oxidized form of platinum was also important to avoid the poisoning of the catalyst as the thermally calcined material did not show poisoning for more than 11 hours at a rate of 3.5mmoles of methanol/min/g of the catalyst, a high rate of decomposition. Despite the size being the same, it should also be noted that the thermally calcined catalysts did not show any faceting probably due to 500^{o}C calcination. The contribution of facets in affecting the catalytic performance cannot be ignored and will be a topic of future investigations. The spherical geometry is the most stable configuration and may expose the most stable planes as opposed to the faceted geometry which may expose more reactive planes. This could explain the higher activity of chemically reduced catalyst (PTCR) in the low temperature regime however the catalytic performance was hampered at elevated temperature possibly due to partial poisoning of the catalyst. The role of support was not the main focus of the study as the support was kept same for different preparation of platinum coated nanoparticles. The effect of different coating procedure on the chemical and physical properties of support oxide was inconclusive as the support did not show any significant changes in the XPS spectra. Thus all the changes in the catalytic performance can be related to the changes in the chemical state of platinum.

5.2.4 In-situ diffuse reflectance spectroscopy

FTIR analysis was performed on all the samples to identify any difference in the mechanism of decomposition of methanol which may have resulted in lowering the activity PTCR and poisoning of PTCR-T samples. General observations were consistent with the observations of Wachs et al [16, 51-53]. It was surprising that no apparent difference was found between the samples except that there were no signs of immediate breakdown of methanol at 150^{o}C for PTCR and PTCR-T samples after stopping the flow of methanol. The spectra are not shown for

the brevity of manuscript; however, the peaks from the sample PTCT is being discussed and shown with respect to changes in temperature in figure 9.

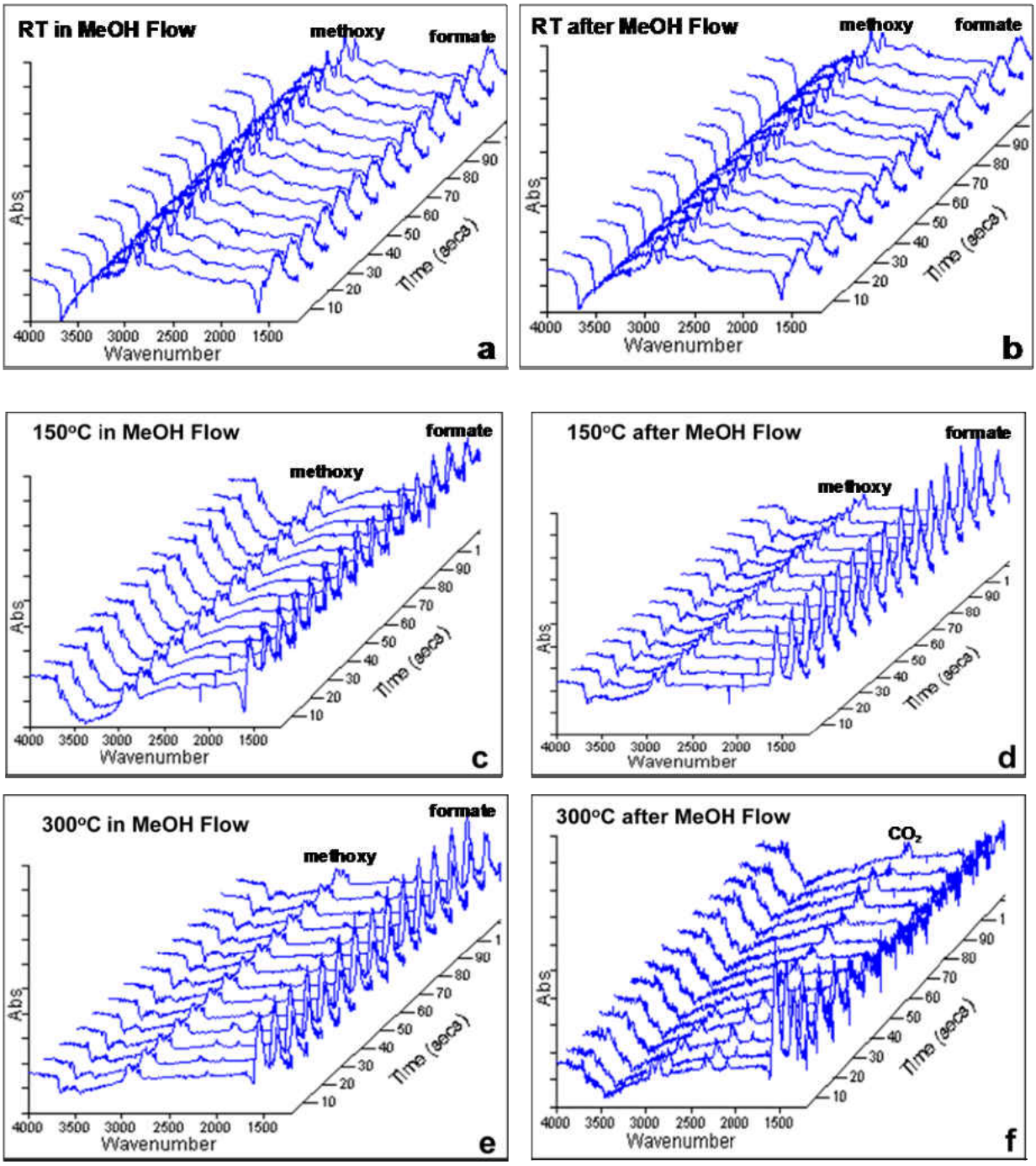

Figure 5-9 In-situ diffuse reflectance spectroscopy spectra of various in methanol flow and after the flow of methanol at different temperatures a, b) at room temperature (RT) c,d) at 150°C e,f) at 300°C shows the behavior of methanol decomposition over the surface of catalyst. The peaks

in the region 2950 to 2810 cm^{-1} correspond to the C-H sym and asym stretch mode from the OCH_3 group of methanol while peaks in region 1570 – 1300 cm^{-1} shows presence of O-C-O stretch from formate.

At room temperature the peaks corresponding to only physical adsorption of methanol can be observed at 2952 and 2841 cm^{-1} for C-H stretching mode of the methoxy group. The methanol is not desorbed from the surface upon stopping the methanol flow and the absorption peaks correspond only to physisorbed methanol during and after the methanol flow at room temperature. Upon increasing the temperature to 150^{o}C the peaks from the physisorbed methanol disappeared and the peaks corresponding to the chemisorbed methanol arise from the C-H stretch of the methoxy group at 2935 and 2830 cm^{-1}. The peaks from the bending mode were not very apparent however the formate peak at 1572 and 1385 cm^{-1} was visible. These formate peaks are at higher wavelength than the normal formate peaks possibly due to the support interactions. The C-H stretch from the formate also appeared at 2880 and 2961 cm^{-1} suggesting that the stepwise dehydrogenation of methanol is the preferred mechanism of decomposition of methanol. For efficient catalysis it is imperative that the reactants must be adsorbed on the catalyst surface leading to the formation of products which should be readily desorbed from the surface. The relative stability and energy for adsorption should be an intermediate value such that the reaction proceeds in the forward direction and the products are desorbed from the surface with relative ease. From figure 9 c, d it is clear that both the species are coexistent on the surface however; these are strongly adsorbed on the surface as even after stopping the flow of the methanol the C-H stretching peaks from methoxy and the O-C-O stretching peaks form the formate were present (for the duration of measurement). Thus even though the decomposition of methanol may take place at 150^{o}C the yield will be low as the catalyst is supersaturated. Upon increasing the temperature to 300^{o}C the peaks due to formate adsorption shifted to lower values than at 150^{o}C and appeared at 1564 and 1383 cm-1. At this temperature both the reactants and the products

were readily desorbed from the surface and the formate as well as methoxy peaks disappeared within few seconds of stopping the flow of methanol. This shows that at 300^{o}C the relative stability of the reactants and products on the surface of nanoparticles is low enough to allow immediate desorption of products. Such an observation also hints at lower poisoning of the PTCT catalyst at 300^{o}C and the complete decomposition of methanol.

5.3 Summary

It was shown that synthesis of the Pt modified catalysts play a very important role in determining the final oxidation state of platinum on the mixed oxide support. It was found that oxidized form of platinum showed superior catalytic performance without any hints of poisoning for decomposition of methanol at relatively higher rate of 3.5 mmoles/min/g of the catalyst. The complete conversion for Pt modified ceria titania (PTCT) in which Pt was present in both oxidized and reduced form was obtained at 300^{o}C while the catalyst containing predominantly reduced form of platinum (PTCR) could not decompose methanol completely even upon increasing the temperature to 400^{o}C. The catalytic performance improved upon calcination of the chemically reduced and coated platinum over ceria titania supports (PTCR-T) however, the barrier for catalytic transformation increased as indicated by relatively lower conversions in the 200-300^{o}C temperature regime and the high activation energy value. The modification of Pt nanoparticles from a faceted structure to spherical morphology could be one of the reasons for higher activation energy. In contrast the presence of oxidized form of platinum (may be at the surface) resulted in improvement in catalyst performance and showed complete conversion at 400^{o}C but demonstrated a heavy poisoning of the catalyst. The observations are consistent with portions of literature that have shown the relatively superior performance of oxidized form of platinum. The main mechanism for decomposition was found to be dehydrogenation of methanol and was confirmed using DRIFTS. Such a behavior could be a characteristic of the ceria titania

support and future investigations will be aimed at developing a general theory based on the catalysis behavior of the platinum coated supports over a range of reducible and non-reducible supports.

5.4 Experimental details

5.4.1 Synthesis of mixed oxides

Ceria titania (1-5 wt%) mixed oxide was prepared by co-precipitation technique using cerium sulfate and titanium (III) sulfate as precursors. Stoichiometric amounts of titanium sulfate was mixed with cerium sulfate and diluted to a final volume of 50 mL. 1M ammonium hydroxide solution was added drop wise with continuous stirring to this solution and the pH of the solution was gradually increased to 10.0. The remaining suspension was stirred overnight to ensure complete hydrolysis of cerium and titanium ions. The precipitate was then filtered and the filtrate was treated with 30% ammonium hydroxide solution to check if any titanium and cerium ions were left non-hydrolyzed. The collected precipitate was washed repeatedly until the pH of the DI water after washing was neutral. The final powder was dried and calcined at 600^{o}C for 3 hours.

5.4.2 Platinum coating by wet impregnation

120mg of ceria titania mixed oxide was dispersed in 50 mL of deionized water (18.2MΩ). Stoichiometric amount of hexachloro platinic acid was dissolved to yield 0.5wt% Pt on the mixed oxide. The solution was stirred continuously and the water was boiled off. This process ensures the coating of platinum ions on the surface of the oxide support. The powder was collected and heated at 500^{o}C for 3hrs to obtain metallic platinum and decompose excess chlorine. The final powder was finely grounded and labeled as PTCT to represent Platinum coated on ceria titania by thermal decomposition.

5.4.3 Platinum coating by chemical reduction

The chemical reduction and simultaneous coating of platinum was obtained using a previously established procedure [31]. Briefly, 120 mg of ceria titania was suspended in 50 mL of deionized water (18.2MΩ). Stoichiometric amount of hexacloro platinic acid was dissolved to yield 0.5wt% Pt on the mixed oxide. The solution was stirred under argon atmosphere and 10mL of freshly prepared (0.1mg/mL) solution of sodium borohydride was added to the suspension. The reduction of platinum ions to metallic platinum could be observed immediately by a change (to black) in the color of the suspension. The suspension was stirred for 2 hours, filtered using 20 nm alumina filter (ANODISC - 47, 0.1μm) and washed several times with excess deionized water to get rid of excess chlorine. The powder sample was dried at 100^{o}C and labeled as PTCR. To compare the effect of thermal treatment on the oxidation state of platinum another sample was prepared using same conditions and was calcined at 500^{o}C for 3 hrs. This sample was labeled as PTCR-T.

5.4.4 Catalytic activity – decomposition of methanol

The decomposition of methanol was studied using an in-house built catalytic reactor. The scheme of the reactor is presented in the supporting information. The catalytic reactor was coupled to a mass spectrometer (QIC-20, Hiden Analytical). Methanol was bubbled (using Ar as the carrier gas) through the catalytic reactor containing Pt coated mixed oxide support on glass wool. The Ar flow rate was maintained at 20 SCCM and the methanol flow rate through the reactor was calibrated before use. 50 mg of sample was loaded interspersed in 4 layers of glass wool. The temperature was varied from 125^{o}C to 400^{o}C in 25^{o}C increments and the pressure was noted until it stabilized. The relative pressure of the gases was noted from the mass spectrometer.

5.4.5 In-situ diffuse reflectance infra red spectroscopy (DRIFTS)

DRIFTS was used to study the nature of reactants and products on the surface of the catalyst using HARRICK reaction cell chamber. The scheme of the DRIFTS set up is presented in supporting information. Methanol was flown through a bubbler using Argon as the carrier gas at 40 SCCM. The dry Pt coated mixed oxide powder was mixed with KBr and packed in the sample cell holder. The sample in the reaction cell was heated at 150 and 300^{o}C and the adsorption and formation of various products was monitored using FTIR Spectrum One (Perkin Elmer). Time base software was used to record measurements at every 10 seconds for a total of 2 minutes at a resolution of 4 cm^{-1}. The spectra were recorded during and after the methanol flow through the cell to qualitatively record the rate at which the adsorbed species are desorbed from the surface of the catalyst. As the methanol flow was turned off, the connection to the vacuum was also turned off during the collection of spectra to reduce the physical surface desorption at elevated temperatures. A new sample was used at each temperature under study and allowed to run in vacuum at the fixed temperature overnight to allow degassing and stabilization of catalyst in the reaction cell. Different catalysts at defined temperatures (room temperature, 150^{o}C and 300^{o}C) were used as a baseline so that the peaks corresponding to only adsorption of methanol are observed.

5.4.6 High resolution transmission electron microscopy (HRTEM)

The size and the distribution of the Pt coated on mixed oxide supports were characterized by HRTEM (Philips, Tecnai) operated at 300 KV with a point to point resolution of 0.2 nm. Samples were prepared by placing a drop of suspension of Pt coated nanoparticles in acetone over the holey carbon coated copper grids. The TEM grids were dried overnight in a vacuum dessicator before imaging.

5.4.7 X-ray photoelectron spectroscopy (XPS)

XPS measurements were done using 5400 PHI ESCA spectrometer using Mg Kά as source of x-rays operating at a power of 300 W. The base pressure during the measurements was below 10^{-9} torr. Pt coated powder samples were mounted on a carbon tape for XPS analysis. The charging shift was calibrated with the binding energy of Carbon (1s) as a baseline. The instrument was calibrated prior to running samples using Gold as the standard. The peaks were deconvoluted using Peakfit software by assigning peaks for Pt(0), Pt(2) and Pt(4). The fitting of the peaks by assigning just Pt(2) or Pt(0) resulted in extremely large FWHM and thus at least three peaks corresponding to the three oxidation states of Pt was assigned. For comparison between different samples the FWHM was kept constant from sample to sample for Pt(0) and Pt(2) as 1.65 and 1.9 while the FWHM for Pt(4) was left floating and the distance between the peaks from Pt $4f_{5/2}$ and $4f_{7/2}$ was fixed at 3.3eV.

5.4.8 X-ray diffraction (XRD)

Powder XRD (Rigaku D-Max B) was recorded using Cu Kά radiation in the 2 theta range of 20-80. The powder samples were calcined at 600^{o}C for 3 hours to determine the phase and crystallinity of the mixed oxide. The equipment was calibrated using standard quartz sample.

5.4.9 Surface area analysis

Surface area was measured using BET sorptometer (Nova 4200, Quantachrome) using nitrogen physisorption. The surface area was measured for the mixed oxides sample both before and after coating with platinum and did not show significant difference in the surface area values.

5.5 References

1 S. Imamura, T. Hagashihara, Y. Saito, H. Aritani, H. Kanai, Y. Matsumura, and N. Tsuda, Catalysis Today 50 (1999) 369-380.

2 J. Greeley, and M. Mavrikakis, Journal of the American Chemical Society 126 (2004) 3910-3919.

3 S.A. Vilekar, I. Fishtik, and R. Datta, Journal of Catalysis 252 (2007) 258-270.

4 G. Avgouropoulos, J. Papavasiliou, and T. Ioannides, Chemical Engineering Journal 154 (2009) 274-280.

5 J.H. Jang, Y. Xu, D.H. Chun, M. Demura, D.M. Wee, and T. Hirano, Catalysis Letters 134 258-263.

6 S.H. Ahn, O.J. Kwon, I. Choi, and J.J. Kim, Catalysis Communications 10 (2009) 2018-2022.

7 S. Esposito, M. Turco, G. Bagnasco, C. Cammarano, P. Pernice, and A. Aronne, Applied Catalysis a-General 372 48-57.

8 S. Kudo, T. Maki, K. Miura, and K. Mae, Carbon 48 1186-1195.

9 H. Lorenz, S. Turner, O.I. Lebedev, G. Van Tendeloo, B. Klotzer, C. Rameshan, K. Pfaller, and S. Penner, Applied Catalysis a-General 374 180-188.

10 Y. Matsumura, and H. Ishibe, Journal of Catalysis 268 (2009) 282-289.

11 R. Tesser, M. Di Serio, and E. Santacesaria, Chemical Engineering Journal 154 (2009) 69-75.

12 P.P.C. Udani, P. Gunawardana, H.C. Lee, and D.H. Kim, International Journal of Hydrogen Energy 34 (2009) 7648-7655.

13 A. Kuzume, Y. Mochiduki, T. Tsuchida, and M. Ito, Physical Chemistry Chemical Physics 10 (2008) 2175-2179.

14 M.V. Ganduglia-Pirovano, C. Popa, J. Sauer, H. Abbott, A. Uhl, M. Baron, D. Stacchiola, O. Bondarchuk, S. Shaikhutdinov, and H.J. Freund, Journal of the American Chemical Society 132 2345-2349.

15 H.Q. Guo, D.B. Li, D. Jiang, W.H. Li, and Y.H. Sun, Catalysis Letters 135 48-56.

16 G.S. Li, D.H. Hu, G.G. Xia, and Z.C. Zhang, Topics in Catalysis 53 40-48.

17 D.R. Rolison, Science 299 (2003) 1698-1701.

18 A. Wittstock, V. Zielasek, J. Biener, C.M. Friend, and M. Baumer, Science 327 319-322.

19 D.L. Coffing, and J.L. Wile, Journal of Chemical Education 70 (1993) 585-586.

20 J.R. Croy, S. Mostafa, H. Heinrich, and B.R. Cuenya, Catalysis Letters 131 (2009) 21-32.

21 J.R. Croy, S. Mostafa, L. Hickman, H. Heinrich, and B.R. Cuenya, Applied Catalysis a-General 350 (2008) 207-216.

22 J.R. Croy, S. Mostafa, J. Liu, Y.H. Sohn, H. Heinrich, and B.R. Cuenya, Catalysis Letters 119 (2007) 209-216.

23 Y. Xu, W.A. Shelton, and W.F. Schneider, Journal of Physical Chemistry A 110 (2006) 5839-5846.

24 W.X. Li, Journal of Physics-Condensed Matter 20 (2008).

25 W.X. Li, L. Osterlund, E.K. Vestergaard, R.T. Vang, J. Matthiesen, T.M. Pedersen, E. Laegsgaard, B. Hammer, and F. Besenbacher, Physical Review Letters 93 (2004).

26 E.M.C. Alayon, J. Singh, M. Nachtegaal, M. Harfouche, and J.A. van Bokhoven, Journal of Catalysis 263 (2009) 228-238

27 T.M. Pedersen, W.X. Li, and B. Hammer, Physical Chemistry Chemical Physics 8 (2006) 1566-1574.

28 Y. Xu, W.A. Shelton, and W.F. Schneider, Journal of Physical Chemistry B 110 (2006) 16591-16599.

29 N. Seriani, W. Pompe, and L.C. Ciacchi, Journal of Physical Chemistry B 110 (2006) 14860-14869.

30 W. Li, and B. Hammer, Chemical Physics Letters 409 (2005) 1-7.

31 C.A. Linkous, G.J. Carter, D.B. Locuson, A.J. Ouellette, D.K. Slattery, and L.A. Smitha, Environmental Science & Technology 34 (2000) 4754-4758.

32 F.B. Li, X.Z. Li, M.F. Hou, K.W. Cheah, and W.C.H. Choy, Applied Catalysis A-General 285 (2005) 181-189.

33 B.M. Reddy, A. Khan, Y. Yamada, T. Kobayashi, S. Loridant, and J.C. Volta, Journal Of Physical Chemistry B 107 (2003) 5162-5167.

34 J. Rynkowski, J. Farbotko, R. Touroude, and L. Hilaire, Applied Catalysis A-General 203 (2000) 335-348.

35 Z.M. Shi, W.G. Yu, and X. Bayar, Scripta Materialia 50 (2004) 885-889.

36 A.K. Sinha, and K. Suzuki, Journal Of Physical Chemistry B 109 (2005) 1708-1714.

37 C.S. Wright, R.I. Walton, D. Thompsett, and J. Fisher, Inorganic Chemistry 43 (2004) 2189-2196.

38 A.W. Xu, Y. Gao, and H.Q. Liu, Journal Of Catalysis 207 (2002) 151-157.

39 H.Q. Zhu, Z.F. Qin, W.J. Shan, W.J. Shen, and J.G. Wang, Journal Of Catalysis 225 (2004) 267-277.

40 J. Graciani, J.J. Plata, J.F. Sanz, P. Liu, and J.A. Rodriguez, The Journal of Chemical Physics 132 104703-104708.

41 G. Avgouropoulos, Catalysis Communications 10 (2009) 682-686.

42 D.H. Chun, Y. Xu, M. Demura, K. Kishida, D.M. Wee, and T. Hirano, Journal of Catalysis 243 (2006) 99-107.

43 A.Y. Kapran, L.M. Alekseenko, and S.N. Orlik, Theoretical and Experimental Chemistry 45 (2009) 338-342.

44 S.D. Lin, T.C. Hsiao, and L.C. Chen, Applied Catalysis a-General 360 (2009) 226-231.

45 Z.M. Ni, J.H. Mao, G.X. Pan, Q. Xu, and X.N. Li, Acta Physico-Chimica Sinica 25 (2009) 876-882.

46 T. Tsoncheva, L. Ivanova, C. Minchev, and M. Froba, Journal of Colloid and Interface Science 333 (2009) 277-284.

47 T. Tsoncheva, J. Rosenholm, C.V. Teixeira, M. Dimitrov, M. Linden, and C. Minchev, Microporous and Mesoporous Materials 89 (2006) 209-218.

48 H.R. Wang, Y.Q. Chen, Q.L. Zhang, Q.C. Zhu, M.C. Gong, and M. Zhao, Journal of Natural Gas Chemistry 18 (2009) 211-216.

49 J. Zhou, and D.R. Mullins, Journal of Physical Chemistry B 110 (2006) 15994-16002.

50 A. Dauscher, L. Hilaire, F. Lenormand, W. Muller, G. Maire, and A. Vasquez, Surface and Interface Analysis 16 (1990) 341-346.

51 M. Badlani, and I.E. Wachs, Catalysis Letters 75 (2001) 137-149.

52 L.J. Burcham, L.E. Briand, and I.E. Wachs, Langmuir 17 (2001) 6164-6174.

53 I.E. Wachs, J.M. Jehng, and W. Ueda, Journal of Physical Chemistry B 109 (2005) 2275-2284.

6 Summary

The current thesis described the role of local environment on tuning the physicochemical properties (such as optical properties, self-assembly, colloidal stability and reactivity) of oxide nanoparticles. It was shown that the exposed surface of nanoparticles in contact with the immediate environment (solid, liquid or gas) can affect its properties. The salient features of this thesis are:

1. Demonstration of the effect of environment on the physical as well as chemical properties of nanomaterials. Specifically the shift in the optical properties of cerium oxide as a function of increase in concentration of non-bonding *f* electrons in causing the red or blue shift dependent upon the environment.
2. This thesis demonstrates the one step synthesis of cerium oxide nanoparticles to extend its stability in a wider range of pH without interfering with their bio-catalytic activity.
3. It shows that polymeric coatings can also play an active role on the surface by involving in the formation of meta stable complexes that can tune the activity of nanomaterials particular to the environment they interact with.
4. This thesis demonstrates the interfacial electron transfer between solid state cerium oxide nanoparticles with superoxide and peroxide radicals/species present in aqueous state and their mediation through the surface adsorbed species.
5. It emphasizes the importance of synthesis in tuning the catalytic performance of surface modified noble metal supported on oxides. It also demonstrates that the oxidation state of platinum coated over the surface of mixed oxides can be tailored by varying the reducing environment. This thesis provided an experimental evidence for the better catalytic ability

of platinum in its oxide form as compared to metallic platinum for decomposition of methanol

The thesis essentially emphasizes that the properties of nanomaterials are a function of their surface and thus careful engineering of surfaces can be utilized to limit, perturb, react, influence and stabilize nanoparticles as a function of the medium.

This is the pre-peer reviewed version of the following article: Self Assembly of Cerium Oxide Nanostructures in Ice Moulds, Small 2008, Volume 4, Number 8, page 1210-1216. Full text of the article can be found at: http://www3.interscience.wiley.com/journal/120846928/abstract

7 APPENDIX – A: SELF-ASSEMBLY OF CERIUM OXIDE NANOSTRUCTURES IN ICE MOULDS

7.1 Introduction

The following chapter is a joint work of two graduate students and has been used as a part of the thesis by Dr. Satyanarayana Kuchibhatla in his PhD thesis "Probing and tuning the size, morphology, chemistry and structure of nanoscale cerium oxide". Since this work has already been a part of one thesis, it is not included in the main chapters of the thesis but as an appendix to avoid any possible conflict or plagiarism. Author wanted to include this chapter as an appendix as fair amount of time and work has been dedicated to this work during the graduate study and that author is also the equal contribution author of the published manuscript. The 5 main chapters of the thesis stand alone and this appendix just describes the effect of environment on the self assembly properties of cerium oxide nanoparticles.

Nature epitomizes 'self-assembly' –living cells arranged in a myriad of complex forms and structures, acting as one particularly complex example. The challenge of synthesizing hierarchically ordered and complex structures with molecular level recognition is another example of a natural process that cannot yet be duplicated in the laboratory. Fundamental research in understanding such self-assembly of molecules has led to new strategies for synthesizing functional nanomaterials[1, 2]. Several nanomaterial structures, facilitated via self-assembly, have already been demonstrated by various researchers[3-13]. Among the multitudes of morphologies and configurations, one dimensional nanostructures (ODNS) have received significant attention from researchers, owing to their potential use in new generation electronics, photocatalysis, sensors, and biomedical applications[7].

Here, we demonstrate the self-assembly and time dependant evolution of ceria nanoparticles into ultra-long polycrystalline ceria nanorods (length *ca.* 3 – 3.5 micron, diameter ca. 30 nm) simply

by freezing, and subsequent aging an aqueous solution containing nanoparticles. The mechanism we propose is effectively a natural form of templated self-assembly. Over time particles trapped in voids (which form in ice) gradually evolve into polycrystalline nanorods by localized oriented attachment of ceria nanoparticles [14-16].

Current emphasis of research on the one dimensional nanostructures has lead to several synthetic strategies for synthesis of nanorods, nanowires and nanotubes. These include processes such as physical and chemical templating, wetting and dewetting, laser based processing, electrochemical etching and electrospinning etc[7]. Among these possible strategies, self-assembly of nanoparticles in aqueous or non-aqueous solutions has become one of the preferred means of obtaining ODNS. Oriented attachment and anisotropic growth of nanoparticles in solution[17, 18] are fundamental components of the self-assembly of crystalline and polycrystalline nanoparticles in solution. Researchers have also used a variety of means to either inhibit or enhance aggregation or particle growth including the use of surface coatings[19]. Of relevance to the current work, Mao et. al[20] have examined the impact of thiol group to assist the ordering of quantum dots at low and high temperature after periods of up to 24 hours. The use of the surfactant and less than 24 hour time contrasts with many of the effects reported in the current study which involve uncoated surfaces and are not apparent for times less than several days.

We have recently reported the synthesis of polycrystalline ceria octahedral superstructures by self-assembly through oriented agglomeration in both water and poly(ethylene glycol)[21]. These contrast with the spherical (high index planes stabilized), single crystal ceria nanoparticles synthesized by Feng et al[22] in a high temperature gas phase reaction. Clearly, agglomeration kinetics and behavior of ceria nanoparticles will change with environmental conditions. Motivated by this, we have studied their aging characteristics under different conditions,

including altering the solution environment and temperature. We have observed the evolution of ceria nanorods supported by the ice templates under freezing conditions. In addition to the formation of nanorods we also observe the formation of polyhedral superstructures, which appear during the freezing process (similar to those which appear during the room temperature aging of aqueous solutions). Because advances in molecular dynamics (MD)-based simulation are beginning to enable self-assembly[3, 23-25] to be modelled theoretically, we have applied MD calculations to examine the dimensionally constrained aggregation process.

7.2 Results and discussion

In the present work, a seeding solution of ceria nanoparticles was synthesized using a simple water based method by oxidizing the Ce(III) precursor salt to Ce(IV) . Several 3-5 nm crystallites nucleate and start to agglomerate within a short time frame (Figure 7-1a). The solution containing ceria crystallites was subjected to sub-zero temperatures (-18^{o} C) and aged for different time scales.

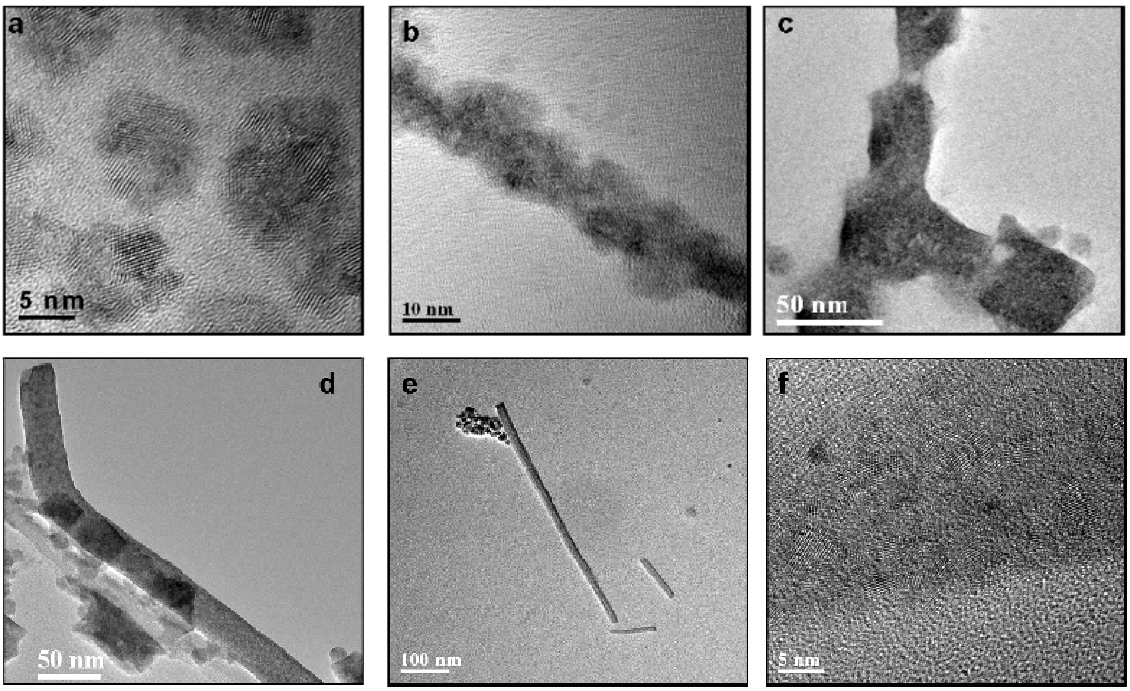

Figure 7-1: TEM images taken from frozen ceria solution (after melting) a) Immediately after the formation of ceria nanoparticles (10-15 nm agglomerate contains of 3-5 nm ceria nanocrystals), and after freezing and subsequent aging for b) 1 day - the zigzag alignment nanoparticles into a one dimensional self assembled structure is apparent c) 1 week – initial ceria nanocrystals agglomerated in ice structure anisotropically to form long ceria nanorods d) 1 week-aged samples showing complete ceria nanorods e) 2 weeks – a long ceria nanorod (aspect ratio 1:20) formed after aging in ice f) 2 weeks - a high magnification image of the ceria nanorod of figure 7-1e showing polycrystalline nature of ceria nanorods with 3-5 nm nanocrystallites. These 3-5 nm nanocrystallites are retained and serve as the building blocks for the formation of nanorods.

Crystalline ceria nanoparticles agglomerate in an oriented fashion within 1 day of aging and result in rod type structures together with large faceted agglomerates (octahedral superstructures) (Figure 7-1b, SI-1). Both the superstructures and the nanorods were constituted of truncated octahedral building blocks of ceria nanoparticles[23]. The observation of octahedral superstructure within one day of aging in ice directly contrasts the time dependent evolution of nanoparticles into polycrystalline superstructures[21]. Subsequent aging for one week facilitated long polycrystalline nanorods (Figure 7-1c, 7-1d, SI-2). Retention of the initial 3-5 nm particle size, with predominant {111} surfaces, is observed even in the highly dense and polycrystalline ceria

nanorods about 40 nm in diameter (SI-2). Further aging of the nanoparticles in ice (2 weeks) resulted in the formation of ultra-long ceria nanorods (Figure 7-1e, 1f, SI-3a,).

We propose simultaneous occurrence of two different processes during the freezing of ice, leading to the formation of nanorods along with observed octahedral superstructures. While the formation of octahedral superstructures occurs in the concentrated solution during the process of freezing, the formation of nanorods occurs in the nano-pores due confined geometry. Ishiguro et al [26] proved through both experimental and modeling studies that the "ice structure cannot accommodate foreign molecules other than water", this results in the well known "solute rejection" phenomenon. This process is very well acknowledged by the metallurgical engineering literature for alloy solidification and zone refining kind of phenomena, where the progress of solidification front results in the rejection of impurity particles into the liquid phase. In the case of dilute ceria suspensions, as the freezing front proceeds from top to bottom, the ceria nanoparticles will be expelled into the water phase. This leads to a significant increase in concentration of nanoparticles in the unfrozen sol, followed by aggregation and kinetically driven octahedral morphology evolution. The higher concentration of solute ceria particles and the increasing pressure exerted by the ice front on the water phase results in the chemico-physical process mentioned above. It is well known that the ice front will be porous with some capillaries present at the ice – water interface. The nanoparticle suspension will be absorbed into these channels due to pressure differences. Significantly higher concentration of nanoparticles results in their entrapment in these channels as the solidification continues. A somewhat similar process was shown for brines where high concentration of unfrozen brine solutions filledthe channels formed during the freezing of a brine solution[27].

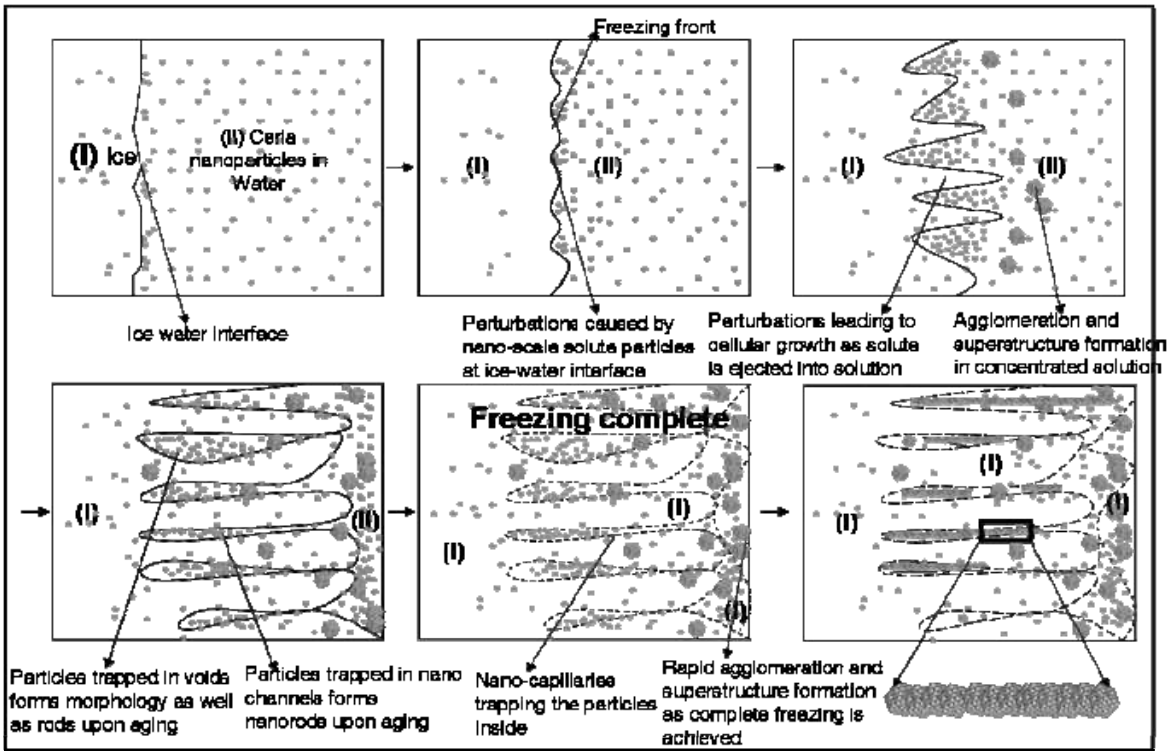

Figure 7-2: A systematic motion of the freezing front producing nano-voids and nano- capillaries during solidification of ice from water. The perturbations caused by the solute particle (ceria nanoparticles in the present case) are assumed to be same as during the solidification of a binary alloy. However, the nanoparticles cause nano-level perturbations during the ice growth forming nano-channels in which solute particles can be trapped. Such a phenomenon is also observed during freezing of polar ice in which brine channels are formed (the brine channels are microscopic in dimension due to high concentration of salt and large size of secondary particles[25]). The rapid agglomeration of the solute which is not trapped and ejected in the remaining solution forms octahedral superstructure.

The formation of nanorods is assisted by the physical structure of ice. At -18 ^{o}C under atmospheric pressure, ice conforms to the "Ice I" structural polymorph[28] and microstructural features, including nano and micro channels, evolve to accommodate the stress and expansion during solidification[29]. These channels, with nanometer diameters and a few microns in length, serve as nano-capillaries (hard templates) and the water, supersaturated with ceria nanoparticles, is forced into the capillary, driven by capillary forces emanating from the freezing front[30, 31]. The initially oriented particles are locked in the capillary under the ice pressure and undergo uni-dimensional oriented agglomeration to form ceria nanorods. It was observed that a very dilute

solution and nanometer size of the particles are central to the formation of channels or capillaries. The perturbation, caused by nanoparticles at the ice-supercooled liquid interface causes channel formation as depicted in figure 7-2 (and SI-4). Ceria nanoparticles trapped in such nanochannels transform into nanorods with predominant {111} terminated surfaces. Specifically, particles trapped in long, nanochannels form the nanorods while those trapped in voids or wide capillaries or in the last portion of the frozen water will form octahedral superstructures. A schematic, depicting such morphological evolution, is presented in figure 7-3a and 7-3b.

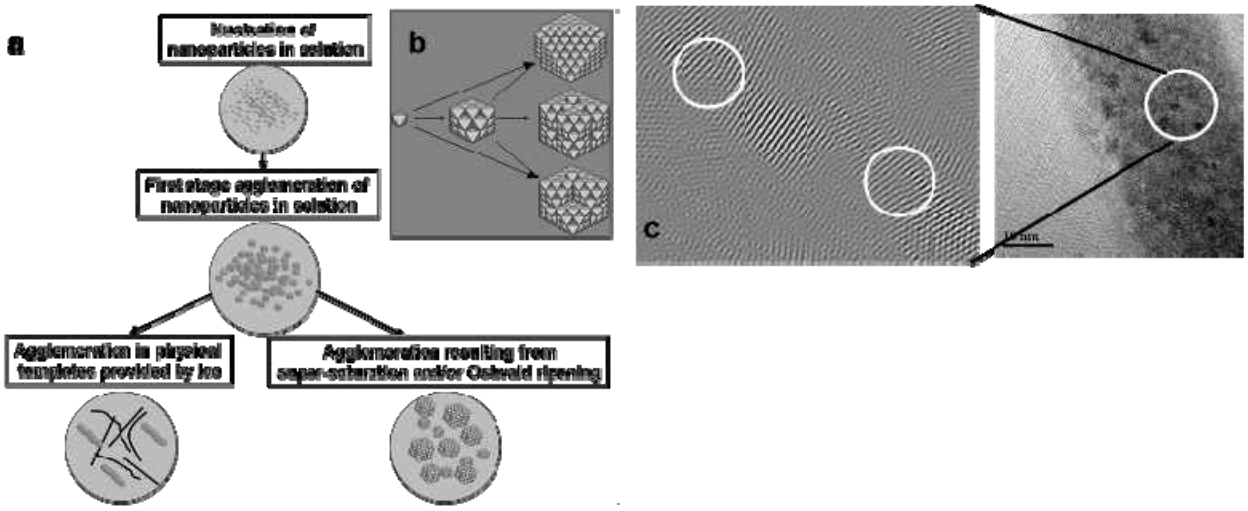

Figure 7-3: Schematic of the evolution of nanorods and octahedral morphology of ceria nanoparticles during freezing and subsequent aging. Initial seeds of ceria nanoparticles having a truncated octahedral geometry grow in an oriented agglomeration to form truncated octahedrons during the initial stages. Upon further aging the particles trapped in ice capillaries form nanorods, while those remaining in solution during the forward motion of the freezing front agglomerate as octahedrons; b) building blocks of octahedral superstructure and nanorods; it can be seen that the initial building block can attach via face to face or edge to edge type of attachment of different nanocrystals; c) Image generated by selected masking and inverse FFT of a high magnification image of ceria nanorods showing dislocations (circles) formed during orientation and self-assembly

Once trapped inside the channels and surrounded by ice, the mobility of ceria nanoparticles is restricted to essentially one dimension. However, the very high surface energy of the

nanoparticles drives the intra – agglomerate rotation to achieve partial oriented attachment at two, three particle interfaces[17, 18]. Such orientation proceeds by incorporation of defects such as dislocations along the interfaces of nanoparticles as shown in figure 7-3c. The white circles indicate the interfacial dislocations formed during the oriented agglomeration. Both the formation of octahedral morphologies and nanorods involve rotation and orientation of the nanoparticles to facilitate low energy configurations via coherent/semi-coherent interfaces. This can be visualized as an imperfect attachment as described in an earlier observation with titania nanoparticles[17, 18]. Higher activation energies and Brownian motion etc. are required for a full crystal rotation or recrystallization to facilitate complete coherence and formation of single crystals. However, in a time limited aggregation under freezing conditions, complete rotation is not achieved and screw/edge dislocations form at the interface between three or more orienting particles (SI-5). As three or more particles align, elastic deformation results in partial coherence together with the evolution of screw dislocations[18]. The formation of screw dislocations is also predicted by our theoretical investigation and is discussed later and shown in SI-6. Upon aging, the mis-orientation and associated dislocations are finally annihilated resulting in energetically stable interfaces.

A comparison of oriented attachment was made using the particle encounter complex (K_{os})[32] model, following equation 1.

$$K_{os} = \frac{4000 \prod N_{av} h^3}{3} \exp(-V_T(h)/kT), \qquad (1)$$

where N_{av} is Avogadro's number, V_T is the total interaction energy between two spherical particles, h is the separation distance between the particles, k is the Boltzmann constant, and T is the temperature. The K_{os} value for ceria nanoparticles indicates a tendency to agglomerate at

ambient temperatures even in a low concentration solution SI-7. It is expected that with the onset of ice nucleation and crystallization, the pH increases to a high (acidic) indeterminate value [33]. Yang et al [11] suggested that oriented agglomeration at high particle concentration was possible only at high acidity or high alkalinity. These conditions are satisfied when the ceria nanoparticles reach a stage of supersaturation while migrating into the aqueous region during freezing process which also increases the acidity in the remaining unfrozen solution. As the freezing front traverses through the system, the supersaturation in the liquid region forces the nanoparticles to agglomerate quickly into octahedral superstructures, driven primarily by the kinetics of the system rather than the thermodynamics. It is evident from our analysis that the formation of such superstructures is complete as soon as the freezing is complete. Conversely, several days of aging is required to facilitate superstructures at room temperature. Nanoparticles trapped in ice channels agglomerate in a similar fashion via localized oriented assembly to form nanorods.

The observation of polycrystalline nanorods under freezing conditions enlightens another side of oriented agglomeration, in which anisotropic self-assembly does not progress through a stage of amorphisation and complete reorientation to form single crystalline structures. The very low thermal energy during freezing and aging at -18 ^{o}C is responsible for maintaining it's polycrystalline nature while the one dimensional confinement caused by channels in ice results in attachment of different polycrystalline particles. The role of ice as a physical template along with the importance of freezing rate was further investigated by subjecting the initial ceria seed solution to direct quenching in liquid nitrogen. During quenching under liquid-nitrogen environment, the total solution was frozen in 50 seconds. This extreme freezing rate does not allow the phenomena of freeze fractionation (solute rejection etc). It is also important to note that there is a fundamental difference in the freezing process when the vials are left in a "freezer" at -

18 ^{o}C and when they are gradually immersed into the liquid nitrogen. While the freezing front proceeds from top to bottom and the capillary phenomena occur in the former case, the same are not feasible in the latter. Hence, the nanoparticles are trapped as is at random positions and thus we have not observed significant differences between as synthesized particles and those frozen in liquid N_2 (i.e. octahedral superstructures were also not observed, SI-8). On the other hand, aging of ceria nanoparticles solution at 2-3 ^{o}C for 2 weeks resulted in formation of faceted agglomerated nanoparticles [SI-8]. The absence of nanorods from the unfrozen solution suggests that templating effect of ice is required for synthesis of nanorods.

Whitesides et al[1] have proposed the 'ground rules' for the self-assembly of basic building blocks as the ease to attain equilibrium between aggregated and non-aggregated states or to adjust their position relative to one another once in an aggregate. While the latter seems to happen in the formation of nanorods under the influence of capillary pressure, morphological evolution within the time frame of freezing reflects the tendency of {111} terminated ceria nanoparticles, to assemble even under fast kinetic conditions. This kind of process has very important and broad implications in establishing the self -assembly mechanism in ceria nanoparticles as the morphology appears within a very short time frame. This also suggests that the total time to achieve morphologically stable equilibrium conditions is very short in the case of ceria nanoparticles, or the morphology can be achieved despite quenching the equilibrium conditions. This phenomenon could be unique to the fluorite structure of ceria nanoparticles. The most interesting part of the present nanorod formation is the evolution of longer nanorods (up to 3.5 micron long) with time (aging under ice) which proves the dynamic nature of self-assembly in static ice templates. It can be observed directly from SI-9 that the zigzag attachment of ceria nanoparticles through {111} planes occur within 1 day of aging at -18 ^{o}C. A strong evidence of

oriented attachment is observed from the FFT pattern as shown in SI-9, which indicates preferential attachment of planes instead of random aggregation of nanoparticles.

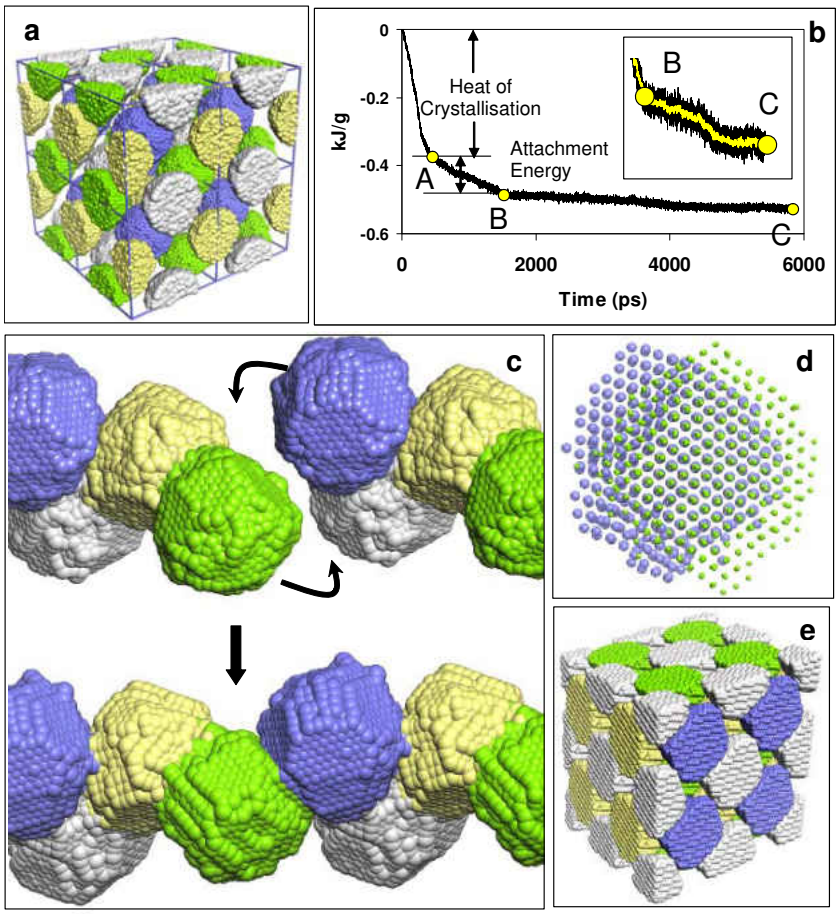

Figure 7-4: Results from MD simulation of self-assembly of nanorods and octahedral superstructure: Atom positions comprising the CeO_2 nanostructures. (a) Starting configuration comprising CeO_2 nanoparticles placed equally spaced into a simulation box a 2×2×2 supercell is shown; (b) configurational energy, calculated as a function of time; (c) structure of a chain/nanorod comprising CeO_2 nanocrystals. Top: after 300 ps of MD simulation. The arrows indicate the trajectory followed by the blue and green nanoparticles as they attach themselves to one another; bottom: after 1500 ps showing the attached configuration; (d) view showing the epitaxy between the nanoparticles attached at {111} surfaces; (e) close packed structure comprising CeO_2 nanocrystals (which corresponds to figure 3b). Cerium is colored to help visualize the individual CeO_2 nanocrystal secondary building units.

Mao et al[20] have systematically studied the synthesis of variously aggregated quantum dots at low and high temperatures. It was reported that the anisotropy at low temperature arises due to the templating effect of the thiol groups and may produce spherically aggregated structures at

even lower temperatures. However the study was limited to 24 hrs of freezing and templating effect of ice was not considered. Synthesis of fibrous and layered sheets of composites exploiting the 'physics of ice formation' was demonstrated recently[29].

As evident from most of the existing literature and from the work quoted above, often the researchers have confined to complicated surfactant mediated assembly and high temperature routes for producing the 1-D nanostructures. We found interesting differences and similarities between Mao et al.'s work and our study. Mao et al have confined their studies to just 24 hrs and reported some intermediate meta-stable structures at sub-zero temperatures. In the present work, we have continued the aging treatment up to several days and proposed a possible mechanism of nanostructure assembly in the ice molds. Based on the present work, we believe that the long term aging study on the nanoparticles is central to our success in obtaining the 1-d, 3-d assemblies. If applied to other systems, the long term aging studies might reveal various exciting features in other nanomaterial systems.

In the present study, we have successfully exploited the physico-chemical processes happening during and after the freezing of ceria nanoparticle sols to mold one-dimensional nanorods (30 nm diameter) and three-dimensional superstructures. This is a first step in using ice moulds to direct the self-assembly of nanoparticles into different shapes, sizes and assemblages. Aforementioned observations are also validated with the help of MD simulations as discussed below.

To assist understanding the impact of constrained geometry on oriented aggregation, we have used molecular dynamics (MD) to simulate nanoparticle self-assembly. Specifically, we explored agglomeration constrained in one and three dimensions, which led to models of chains/nanorods and octahedral superstructures, respectively. The simulation code and potential models have been described previously in reference 3. To facilitate one-dimensional agglomeration,

amorphous/molten CeO_2 nanoparticles, each comprising 6144 atoms and about 5 nm in diameter, were positioned equally spaced, within a cubic simulation cell box 13nm in size, fig. 7-4(a). Each simulation cell comprised four nanoparticles. Constant volume MD simulation was applied to the system for 6800 ps at 3200 K. The high temperature accelerates the dynamical simulation such that the crystallisation and aggregation are complete within the (small) timescale of the simulation. The simulations revealed attractive forces acting between neighboring amorphous/molten nanoparticles. Accordingly, under the MD simulation, the nanoparticles started to move closer to one another and started to crystallize. Specifically, nucleating seeds spontaneously evolved within the nanoparticles facilitating their crystallisation. The resulting nanocrystal morphologies comprised {111} octahedra with the sharp corners truncated by {100} in accord with the experiment. Once crystalline, the nanoparticles continued to be attractive towards one another.

The configurational energy of the system (Fig. 7-4b) was calculated as a function of time. The first 300 ps of time is associated with a steep gradient and reflects, in part, the crystallization of the nanoparticles. The energy difference between the start of the simulation, where all the nanoparticles are amorphous, and fully crystalline nanoparticles, is loosely associated with the heat of crystallization. After 300 ps, the nanoparticles have already aggregated together forming part of a chain, fig. 4(c). During the next 1200 ps, fig. 4(b), point A to point B, two nanoparticles (green and blue, fig 7-4(c)) attach themselves to one another via {111} surfaces; a plan view of the epitaxy between the two nanoparticles is shown in fig. 7-4(d). The attachment energy can be determined as the energy difference between point A and point B, fig 4(b). A movie showing the attachment is available as supporting information SI-10. As the MD proceeds, the energy continues to reduce reflecting annealing conditions. This may include, for example, surface

relaxation, rotation of the nanoparticles to facilitate a better fit, annealing out of dislocations etc. An illustration is shown in supporting information SI-6 in which a screw dislocation anneals out and facilitates coherent matching between the atomic planes of two attached CeO_2 nanoparticles. We also modeled a three dimensional aggregation of {111}-terminated ceria nanoparticles, which form a close packed octahedral structure as shown in figure 7-4e (SI-11a).

Our simulations, where we simulate the self-assembly *directly*, predict that when the system is constrained in one-dimension (modeling the reduced dimensionality of the ice cavities), the ceria nanoparticles attach via {111} faces resulting in a 'zigzag' structure of the nanorod, fig. 7-4(c); rather than, for example, a parallel chain via attachment of {110}. Clearly, random 'zigzag' attachment would not facilitate a linear chain. However, the constraining influence of the ice mold forces nanorod evolution. By simulating self-assembly dynamically, similar to experiment, the models derived are metastable and do not represent thermodynamically the lowest energy structures. Accordingly, after attachment, the nanoparticles (attempt to) rotate to improve the epitaxy and area of coherence. We also observe from the simulations that once attached, the translational and rotational degrees of freedom for the individual nanocrystals are reduced and therefore optimum attachment (thermodynamic) is difficult to attain. We note that the atomistic model of the nanorod/chain, figure 7-4(c), can be used to help describe and understand the observed structure, figure 1b, which is the 1-day old sample. During prolonged aging, the ice becomes harder and denser and will impose high localized pressure upon the chain within the ice-mold. Accordingly, we performed MD simulations on the chain under 0.1 - 0.5 GPa pressure. The animations of the simulation revealed that the nanocrystals reorient and pack tighter together. In contrast, when we do not constrain the nanocrystals to one-dimension (unconstrained) the resulting (kinetically driven) models are three-dimensional, fig. 7-4(e). A

more detailed description of the three dimensional geometry of the superstructures is provided in SI -11(b) and was found to retain their nanocrystal identity upon rearrangement giving rise to polycrystalline superstructures.

7.3 Summary

In this manuscript, we have shown that a natural phenomena such as the structural formation of ice can architecturally sculpt 1-D ceria nanostructures. MD simulations confirm that the type of morphology evolution observed for the ceria nanostructures can be driven by the dimensional constraints. The long term aging studies on nanoparticles in various conditions possibly suggest new and environment friendly (green) approaches for directing the self-assembly of nanostructures. While much has been learned from various resources of nature, harnessing the use of ice as tool to self assemble nanomaterials should be explored further. By altering freezing rates, initial particle concentration, and aging temperature, it should be possible to use these processes and changes in ice structures to sculpt desirable nanostructures comprising nanoparticle building blocks. Clearly, water/ice environments are pivotal to the natural world and its evolution. Understanding and controlling the behaviour of ceria nanoparticles in such environments, as we have done here, is a first step to facilitate future advances spanning, for example, nanofluidics to nano-bio applications [34].

7.4 Materials and methods

Stoichiometric amounts of cerium nitrate (III) hexahydrate (Sigma-Aldrich) were dissolved in deionized water (18.2 MΩ) and 20% PEG (600 MW. from Sigma-Aldrich) + DI water mixtures. This solution was then oxidized using hydrogen peroxide (30% w/w Sigma Aldrich) to form the ceria nanoparticles. Vials containing 15 ml of the solution were stored at 2-3 ^{o}C and another set was frozen in a laboratory chemical freezer. For fast freezing another set of vials containing solution were immersed directly in liquid nitrogen at a rate of 10 mm/sec. The solution freezes

instantaneously upon immersion in the liquid nitrogen. Thus the rate of propagation of solid front can be taken as 10 mm/sec.

7.5 References and notes

1 G. M. Whitesides, B. Grzybowski, *Science* 2002, *295*, 2418.

2 R. F. Service, *Science* 2005, *309*, 95.

3 D. C. Sayle, X. D. Feng, Y. Ding, Z. L. Wang, T. X. T. Sayle, *Journal Of The American Chemical Society* 2007, *129*, 7924.

4 P. D. Yang, T. Deng, D. Y. Zhao, P. Y. Feng, D. Pine, B. F. Chmelka, G. M. Whitesides, G. D. Stucky, *Science* 1998, *282*, 2244.

5 A. Striolo, *Small* 2007, *3*, 628.

6 E. W. Edwards, D. Y. Wang, H. Mohwald, *Macromolecular Chemistry And Physics* 2007, *208*, 439.

7 S. Kuchibhatla, A. S. Karakoti, D. Bera, S. Seal, *Progress In Materials Science* 2007, *52*, 699.

8 A. S. Karakoti, S. Kuchibhatla, S. B. K, S. Seal, *Journal of Physical Chemistry C* 2007, *In press*.

9 H. W. Duan, D. A. Wang, D. G. Kurth, H. Mohwald, *Angewandte Chemie-International Edition* 2004, *43*, 5639.

10 H. Z. Zhang, B. Gilbert, F. Huang, J. F. Banfield, *Nature* 2003, *424*, 1025.

11 M. Yang, G. S. Pang, J. X. Li, L. F. Jiang, S. H. Feng, *European Journal Of Inorganic Chemistry* 2006, 3818.

12 S. C. Kuiry, S. D. Patil, S. Deshpande, S. Seal, *Journal Of Physical Chemistry B* 2005, *109*, 6936.

13 L. Y. Kuo, P. Shen, *Materials Science And Engineering A-Structural Materials Properties Microstructure And Processing* 2000, *277*, 258.

14 N. Bjerrum, *Science* 1952, *115*, 385.

15 M. G. Worster, J. S. Wettlaufer, *Journal Of Physical Chemistry B* 1997, *101*, 6132.

16 A. K. Soper, *Science* 2002, *297*, 1288.

17 R. L. Penn, G. Oskam, T. J. Strathmann, P. C. Searson, A. T. Stone, D. R. Veblen, *Journal Of Physical Chemistry B* 2001, *105*, 2177.

18 R. L. Penn, J. F. Banfield, *Science* 1998, *281*, 969.

19 E. C. Scher, L. Manna, A. P. Alivisatos, *Philosophical Transactions: Mathematical, Physical and Engineering Sciences* 2003, *361*, 241.

20 C. B. Mao, J. F. Qi, A. M. Belcher, *Advanced Functional Materials* 2003, *13*, 648.

21 S. Kuchibhatla, A. S. Karakoti, S. Seal, *Nanotechnology* 2007, *18*.

22 X. D. Feng, D. C. Sayle, Z. L. Wang, M. S. Paras, B. Santora, A. C. Sutorik, T. X. T. Sayle, Y. Yang, Y. Ding, X. D. Wang, Y. S. Her, *Science* 2006, *312*, 1504.

23 T. X. T. Sayle, S. C. Parker, D. C. Sayle, *Chemical Communications* 2004, 2438.

24 P. Martin, S. C. Parker, D. C. Sayle, G. W. Watson, *Nano Letters* 2007, *7*, 543.

25 D. C. Sayle, B. C. Mangili, J. Klinowski, T. X. T. Sayle, *Journal Of The American Chemical Society* 2006, *128*, 15283.

26 H. Ishiguro, B. Rubinsky, *Cryobiology* 1994, *31*, 483.

27 S. Panday, M. Y. Corapcioglu, *Water Resources Research* 1991, *27*, 99.

28 http://www.uwgb.edu/dutchs/PETROLGY/Ice%20Structure.HTM.

29 S. Deville, E. Saiz, R. K. Nalla, A. P. Tomsia, *Science* 2006, *311*, 515.

30 P. O. Scheie, *American Journal Of Physics* 1989, *57*, 279.

31 M. Bougamont, S. Tulaczyk, I. Joughin, *Journal of Geophysical Research* 2003, *108*, 2222.

32 R. L. Penn, *Journal Of Physical Chemistry B* 2004, *108*, 12707.

33 F. Franks, *European Journal Of Pharmaceutics And Biopharmaceutics* 1998, *45*, 221.

34 J. P. Chen, S. Patil, S. Seal, J. F. McGinnis, *Nature Nanotechnology* 2006, *1*, 142.

7.6 Supporting information

7.6.1 Transmission electron micrograph of one day aged nanoceria in ice

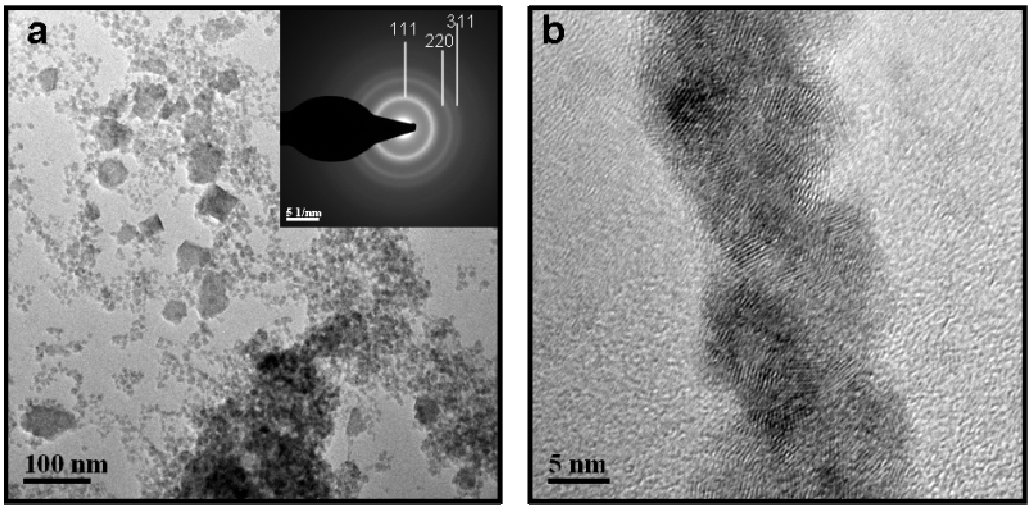

SI 1: TEM images from one day aged frozen solution of ceria a) Image shows ceria nanoparticles with small and large agglomerates (inset electron diffraction confirming the fluorite structure of ceria; also one can see truncated morphology of agglomerating nanoparticles which is usually observed upon controlled ageing) b) Particles orienting together and agglomerating in anisotropic way to give oriented agglomeration.

7.6.2 TEM images of 1 week aged nanoceria in ice

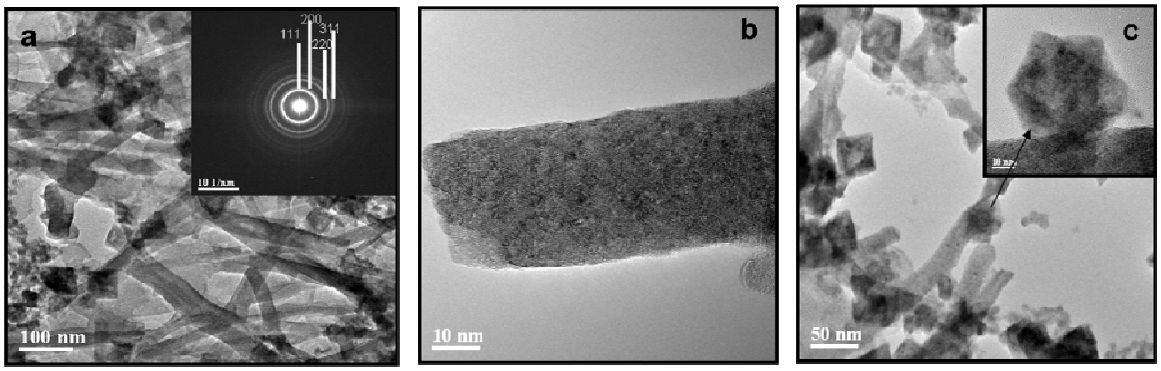

SI 2: TEM images of one week-aged frozen solution of ceria. a) bunch of ceria nanorods with some octahedral structures (SAED in the inset confirms the fluorite structure of the rods and particles) b) the dense packing of individual 3-5 nm ceria nanoparticles making up the nanorods c) TEM image showing the superstructure assembly of ceria octahedra along with nanorod (inset shows the star shape morphology of the superoctahedral ceria)

7.6.3 TEM image of 2 weeks aged nanoceria

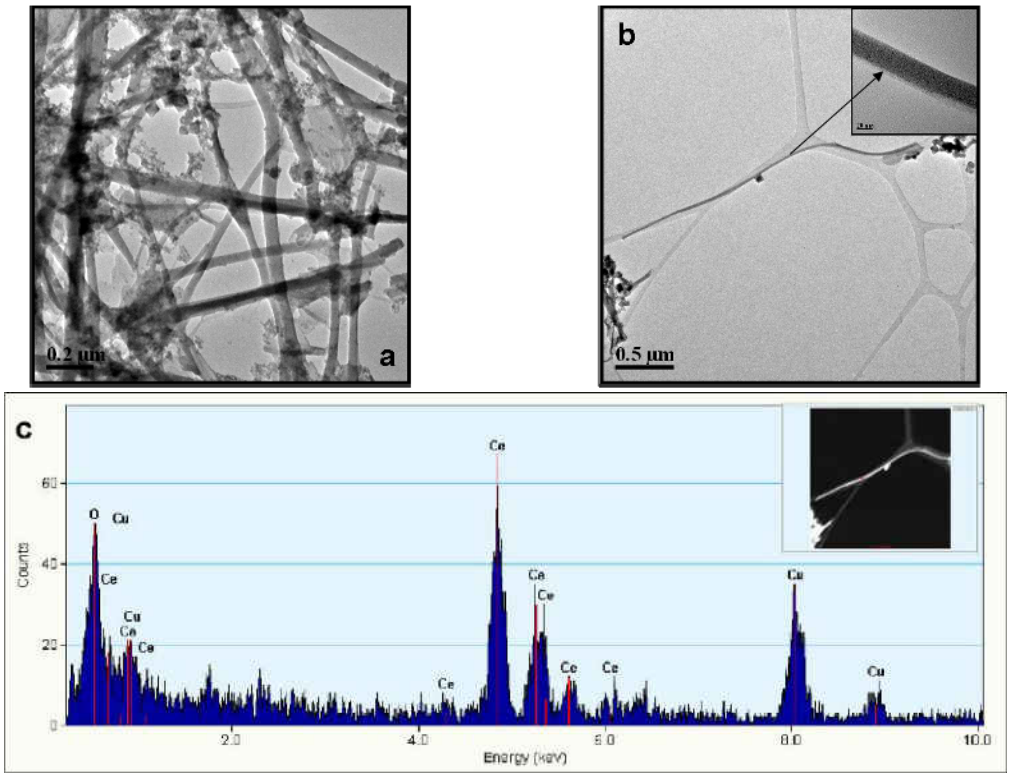

SI 3: TEM image of ceria nanorods taken from three weeks aged frozen solution of ceria. a) confirms high density of long ceria nanorods and octahedral arrangement of agglomerated nanoparticles after 2 weeks of aging b) 3.5 micron long nanorod of ceria (inset shows the diameter as 40 nm) c) EDX spectrum collected on a spot at the nanorod showing the signals from cerium and oxygen.

7.6.4 Mechanism of trapping of nanoparticles in ice channels

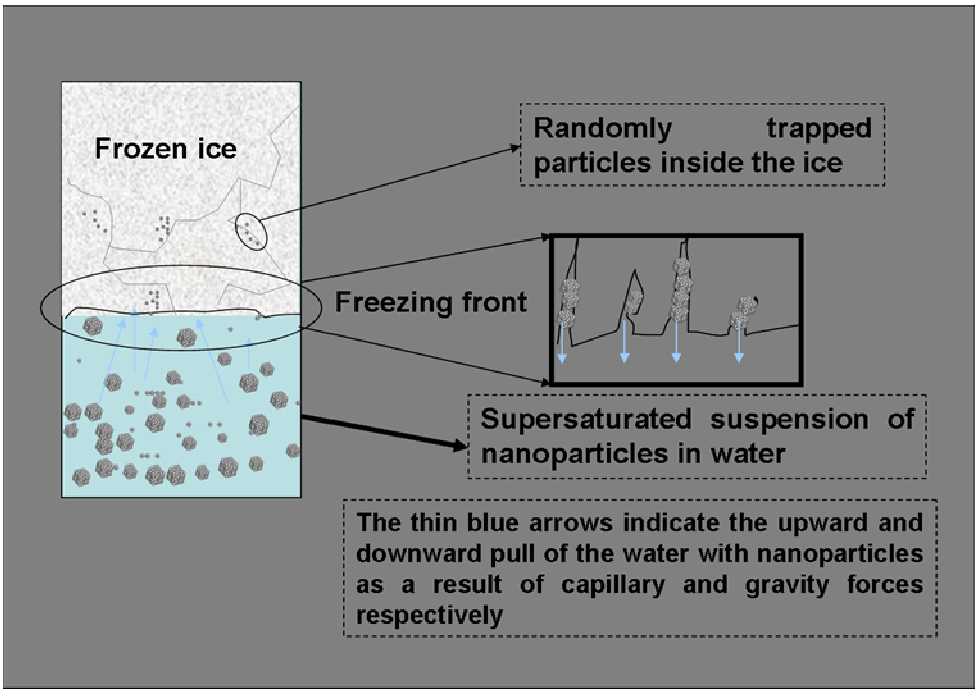

SI-4 Schematic of the process of freezing and entrapment of particles in the ice channels as the liquid moves out of the capillary during the progress of the ice front. The schematic tries to simulate a real situation during the freezing as the ice front progresses from top to bottom. The particles are sucked into the channels along with water into the nano channels and are trapped inside the channels as the water freezes and/or drives out of the channels.

7.6.5 HRTEM image showing oriented attachment of nanoparticles

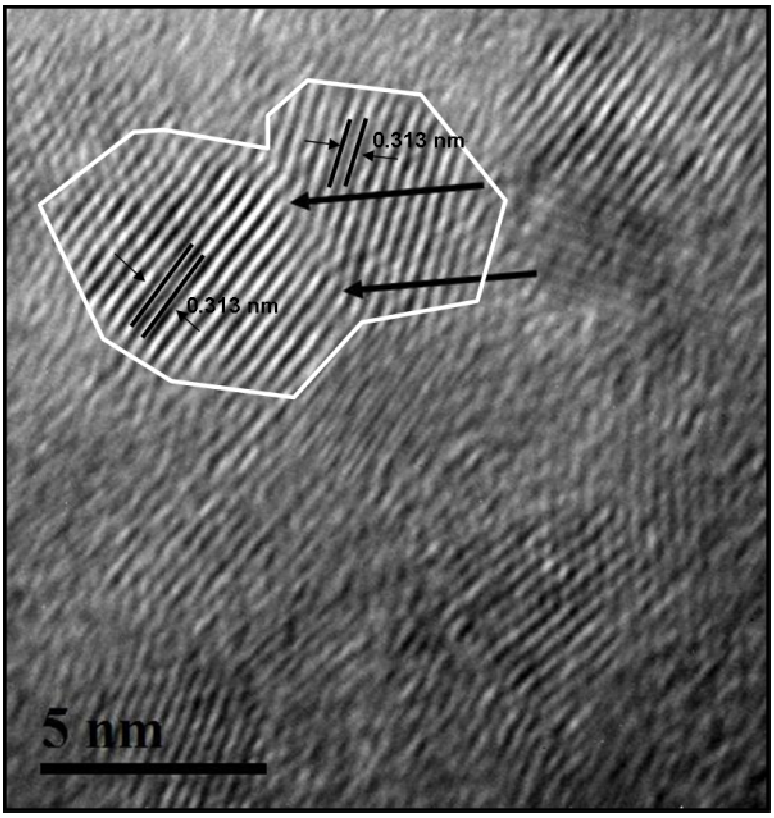

SI 5: HRTEM image of orientation attachment of ceria nanoparticles. Arrows indicate the presence of dislocations at interface during the orientation of two {111} surface terminated ceria nanoparticles. A semi-coherent interface is formed with dislocations which get annihilated over a period of time with aging (SI 6).

7.6.6 Atomistic structure of a screw dislocation

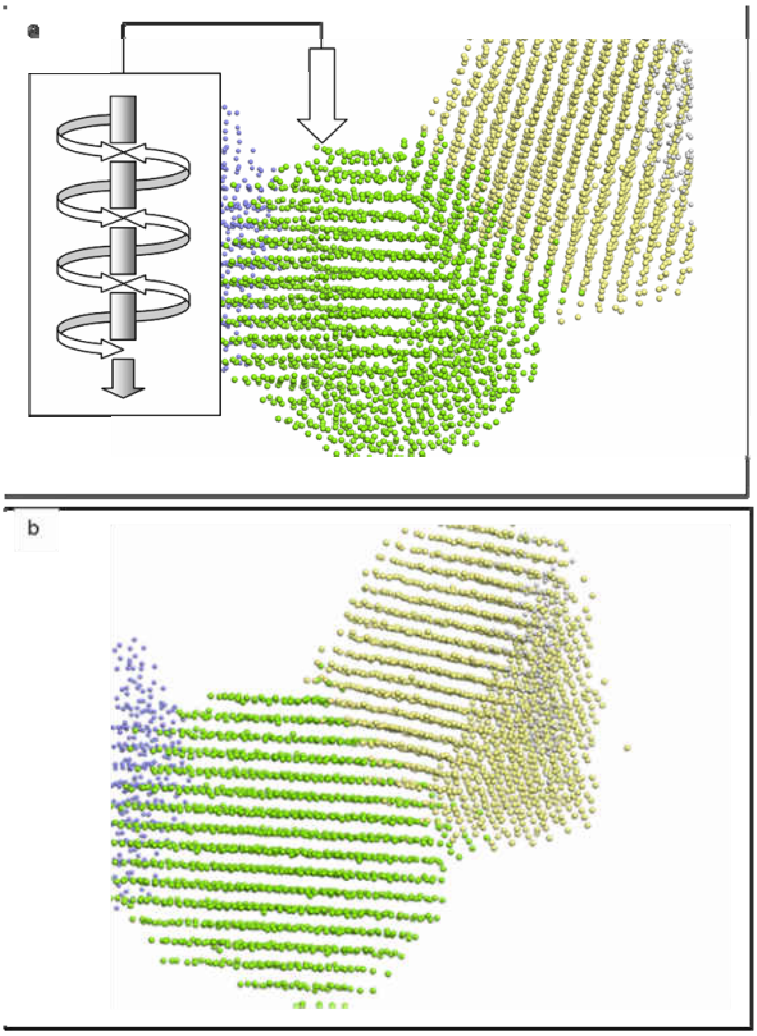

SI 6: (a) Snapshot of part of the simulation cell taken after 990 ps of MD simulation showing two ceria nanoparticles (green and yellow); a third (blue) is partially visible. Within the green nanoparticle, a screw dislocation has evolved. The arrow indicates the position of the core region, which resides at the center of the nanoparticle and traverses its entire diameter. (b) After 6800 ps, the screw dislocation can be seen to have annealed out.

7.6.7 Calculation of aggregation constant

SI-7: K_{os} was calculated using the supporting equations for the total interaction energy VT

$$V_T(h) = \pi R\left(\frac{-H_{121}}{12\pi h} + \frac{64 c_{io}^{*} kT\Gamma_0^{\,2} e^{-\kappa h}}{\kappa^2}\right)$$

For a non-symmetrical electrolyte the κ was calculated using

$$\frac{1}{\kappa} = \sqrt{\frac{\varepsilon_r \varepsilon_o kT}{2000 e^2 N_{Av} I}}$$

Where ε_r is the unitless dielectric constant of the medium, ε_o is the vacuum permittivity, κ is the reciprocal of Debye length, T is the temperature, I is the ionic strength and N_{Av} is the Avogadro's number.

While the Ґo is given by

$$\Gamma_o = \frac{\exp(ze\phi_o / 2kT) - 1}{\exp(ze\phi_o / 2kT) + 1}$$

It must be noted that the estimation of K_{os} assumes a spherical shape of the nanoparticles a homogenous distribution of surface charge over the particle surface. For ceria nanoparticles in a 30 mM solution using a surface potential value of 30 mV, a room temperature value of 298 K, particle size of 5 nm, and obtaining other values from reference (31) the stability constant was found on the order of 10^{-3}. It must be noted that value of K_{os} obtained is for ceria nanoparticles in solution at room temperature and not for rapidly changing conditions during the freezing of ice.

7.6.8 TEM images of nanoparticles under different freezing conditions

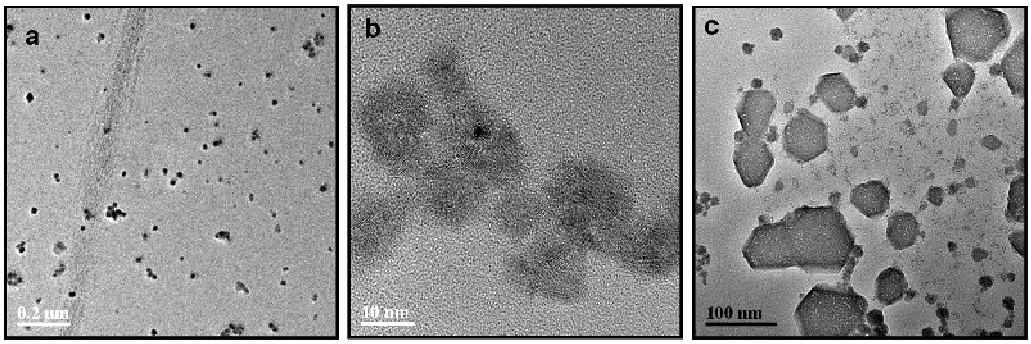

SI 8: Ceria nanoparticles formed in ice (fast freezing) after 2 weeks of aging a) well dispersed nanoparticles which does not show any anisotropic behavior b) high magnification images of ceria nanoparticles showing the individual 3-5 nm ceria nanoparticles c) truncated octahedron in refrigerated (2-3^{o}C) nanoceria after 3 weeks of aging.

7.6.9 High magnification TEM image of 1 day aged nanoparticles

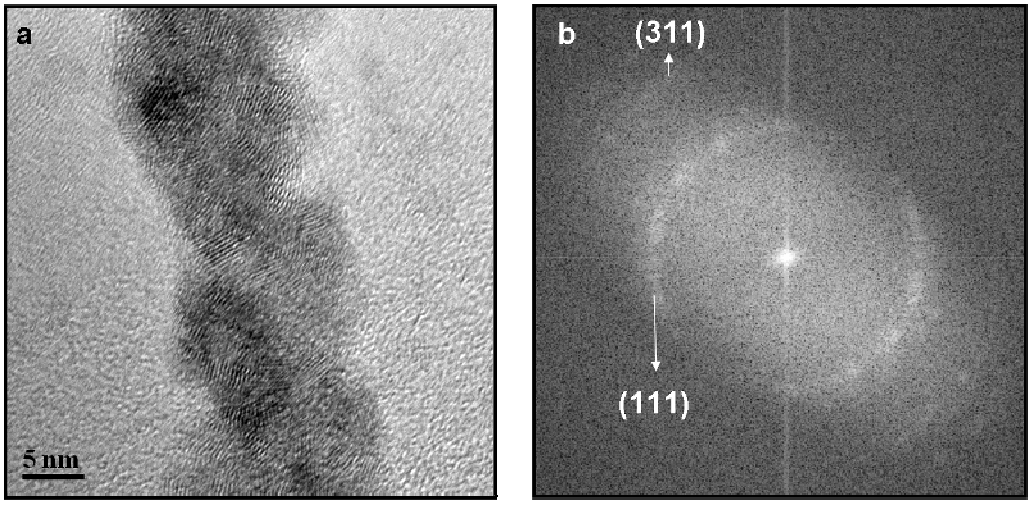

SI 9: High magnification TEM image from one day aged solution of ceria nanoparticles in ice a) shows the zigzag oriented attachment of nanoparticles b) the FFT pattern of figure (a) shows preferred orientation (texture) of {111} planes in during the evolution of nanorods from ceria nanoparticles.

7.6.10 Theoretical details

SI 11a) To facilitate three-dimensional agglomeration, crystalline {111} terminated CeO_2 nanoparticles, 8 nm in diameter, (models generated previously, see reference 13) were positioned, equally spaced, within a simulation box 13.5 x 13.5 x13.5 nm. Constant pressure MD was then applied to this system at -18 ^oC for 350 ps. Constant pressure enables the size of the simulation cell to change and therefore the nanoparticles can compact close together, driven by their attraction to one another. Here the nanoparticles agglomerated and attached via {111} surfaces to form a close packed structure, fig 4e.

SI 11b) When we do not constrain the nanocrystals to one-dimension (unconstrained) the resulting (kinetically driven) models are three-dimensional, fig. 4(e). However, in contrast to the 1D chain, the CeO_2 nanocrystals comprising the 3D superlattice are tightly bound to twelve nearest neighbors. Accordingly, the degrees of freedom are very much reduced and the activation energy associated with any movement of one nanocrystal (to improve, for example, epitaxy or coherence) is so high as to prevent rearrangement. Thus the initial agglomeration (kinetically driven) gets locked into the structure and any extended periods of simulated annealing have little influence upon structural rearrangement. The simulation thus provides model atom positions for the schematics shown in fig. 3b. We note that the CeO_2 nanocrystals in the close-packed structure are not space filling, rather the nanocrystals occupy 73% of the space (calculated using solvent surface of 1.4 Å; Ce^{4+}=0.92 Å, O^{2-}= 1.32 Å). We also performed simulations at 20 GPa pressure and found that the nanocrystals do not agglomerate into the bulk parent material; rather the nanocrystals retain their individual identity, while becoming more space filling.

8 APPENDIX B – APPLICATION OF NANOCERIA IN PREVENTING TUMOR STROMA INTERACTION

8.1 Summary of work

The dextran coated nanoparticles prepared in chapter 3 was tested to prevent the tumor stroma interaction of migrating tumor cells. This work is currently under development and has shown that dextran coated nanoceria can prevent the tumor stroma interaction in tumor cells. To verify and track the movement of nanoparticles inside the tumor cells the dextran coated nanoparticles were conjugated to fluorescent tag (Fluorescein Isothiocyanatae - FITC) using wet chemical procedure. Briefly, FITC was tagged to CNPs coated with dextran. The dextran was oxidized with 10mM sodium periodate which causes the cleavage of C3 and C4 carbon and simultaneous oxidation. This oxidation step was followed by extensive dialysis against deionized water for purification of the oxidized dextran. The oxidation of dextran coated on nanoparticles was confirmed by FTIR by the presence of C=O stretch at 1721cm-1. The FITC was then conjugated to CNPs using reductive amination in carbonate bicarbonate buffer (pH 8.0-9.0) and sodium cyanoborohydride as reducing agent. The final product was then dialyzed extensively followed by evaporation and resuspension of conjugated nanoparticles in deionized water by ultrasonication. The nanoparticle suspension was then washed several times followed by separation from free dye molecule using ultracentrifuge. After repeated washing the filtrate was no longer colored.

The presence of the dye was confirmed by the characteristic absorbance of absorbance of dye at 575nm. The FITC coated nanoparticles were then subjected to cellular uptake in two different cell lines and the cells could be visualized (not shown). The confocal microscopy showed that the nanoparticles can be viewed under excitation by 485nm laser and was used successfully for cellular imaging.

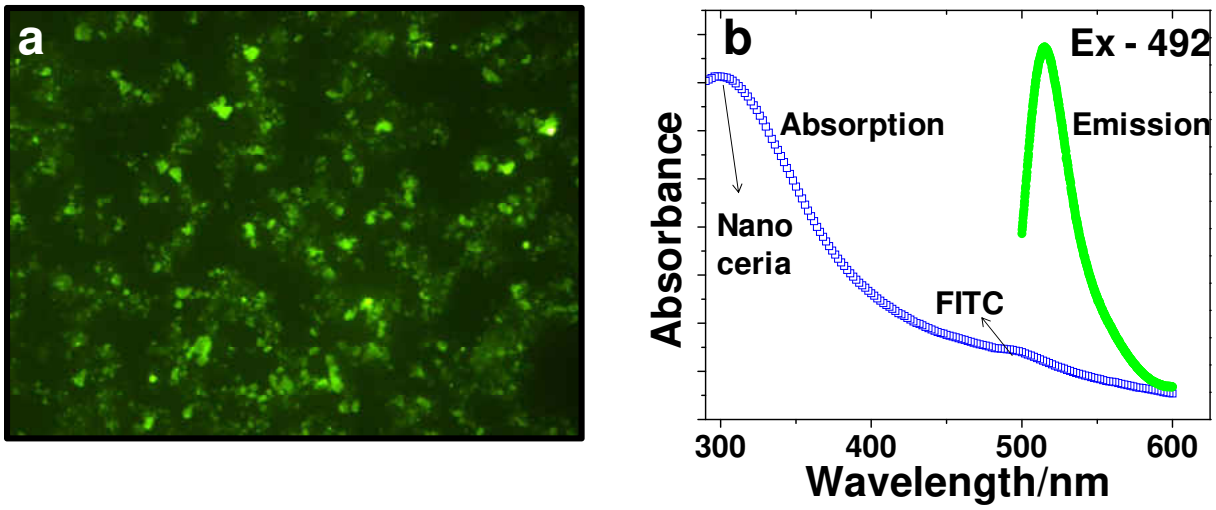

8-1 a) Fluorescent images showing the presence of nanoparticles attached to fluorescent tag (FITC – fluorescein isothicyanate) ex-situ image b) Absorption emission spectra of FITC conjugated nanoceria demonstrating teh absorbance of both nanoparticles and dye molecule as well as emission from the dye.

The prevention of tumor stroma interaction by dextran coated nanoceria particles were studied by standard invasion assay, western blotting and 3-D scaffold model (contaction assay). Nanoceria was found to supress the tumor pregression by reducing teh invasive capacity of tumor cells. It is known that the during the tumor invasion, reactive oxygen species, especially superoxide are involved in mesenchymal-mesenchymal transition of the fibroblast cells to myofibroblasts. This interaction is typicallly known as tumor stroma interaction and determines the invasive capacity of the tumor cells. It was found that nanoceria prepared in dextran could scavenge the superoxide species and thus reduced the invasive capacity of the tumor cells and prevented the conversion of fibroblast cells to myfibroblasts. In addition dextran based nanoceria was also found to kill the tumor cells thereby performing a dual function of protection of healthy mesenchymal cells from invasion and killing of tumor cells.

9 APPENDIX C - RARE EARTH OXIDES AS NANOADDITIVES IN NOVEL 3-D NANOCOMPOSITE SCAFFOLDS FOR BONE REGENERATION

9.1 Summary of work

In this work tailor made rare earth oxide (i.e nanoceria) additives were demonstrated to enhance the production of collagen by HMSCs (Human Mesenchymal Stem Cells) cultured on porous bioactive glass (nanocomposite) scaffolds. The addition of osteogenic supplements was not needed for this to occur. Two different preparations of nano cerium oxide were successfully incorporated in 3-D bioactive glass foam scaffolds and were compared with bioactive scaffolds without nanoceria. Preliminary investigations showed that nanoceria is non-toxic to the cells. HMSCs were cultured with and without osteogenic supplements, namely ascorbic acid, dexamethasone and β-glycerophosphate. After 10 days of culture, nanoceria containing scaffolds showed enhanced osteoblastic differentiation of HMSCs and collagen production compared to the scaffolds without nanoceria even in the absence of any osteogenic supplements. The incorporation of nanoceria may be speculated to control the molecular oxygen thereby regulating the differentiation of HMSCs.

It was shown that the cerium oxide nanoparticles can increase the production of collagen by the HMSCs cultured on the porous bioactive glass scaffolds. This enhancement was a function of the synthesis conditions and medium of nanoparticles as the water based nanoparticles enhanced while the dextran based CNPs reduced the production of collagen. The results were consistent in presence and absence of osteogenic supplements. Both the preparations (bare and dextran coated) were non-toxic to cells and the water based samples showed enhanced osteoblastic differentiation of HMSCs and collagen formation after 10 days of cell culture. Preliminary

investigations ascribe this behaviour to the differences in the initial oxidation state of nanoparticles. The changes that may have occurred during the calcination of the nanoparticles with the bioactive glass are not clear at present and will be a focus of future investigations.

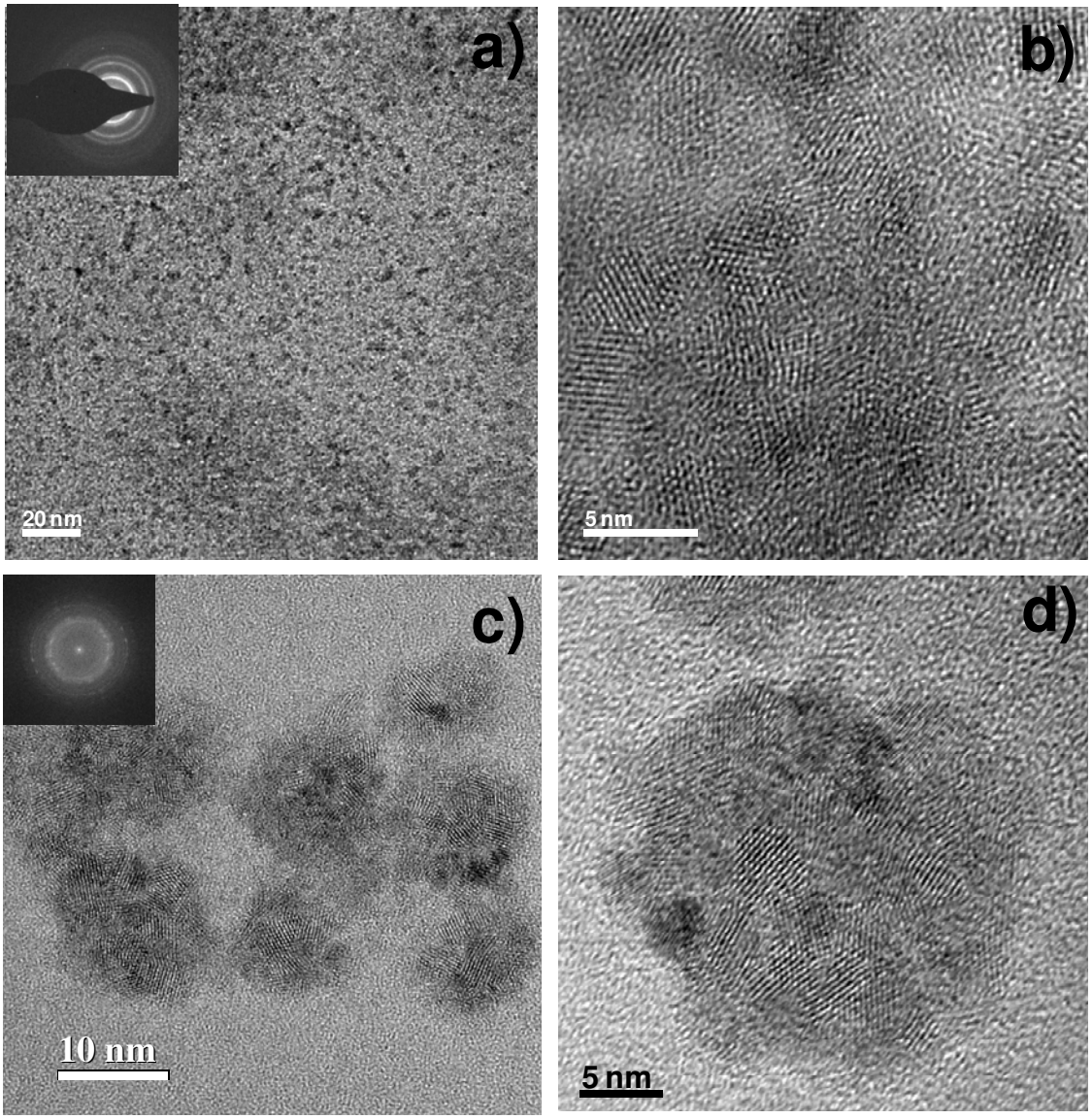

Figure 9-1 High resolution transmission electron micrographs of nanoceria prepared in a) dextran b) high magnification image of nanoceria in dextran c) water d) high magnification image of nanoceria in water. Inset depicts the polycrystalline nature of as prepared nanoceria. Individual particle size of 3-5nm is evident from high magnification images while the agglomerate size varies from 5-15 nm.

The nanoparticles were synthesized using wet chemical synthesis as described in chapter 3. Bare cerium oxide nanoparticles were compared for activity against the dextran coated nanoparticles. It can be observed from figure 9.1 that the dextran coated nanoparticles were highly dispersed and smaller in size as compared to the bare nanoparticles which were slightly more agglomerated. However the oxidation state of cerium in the two preparations was different as observed from spectrum from x-ray photoelectron spectroscopy shown in figure 9.2.

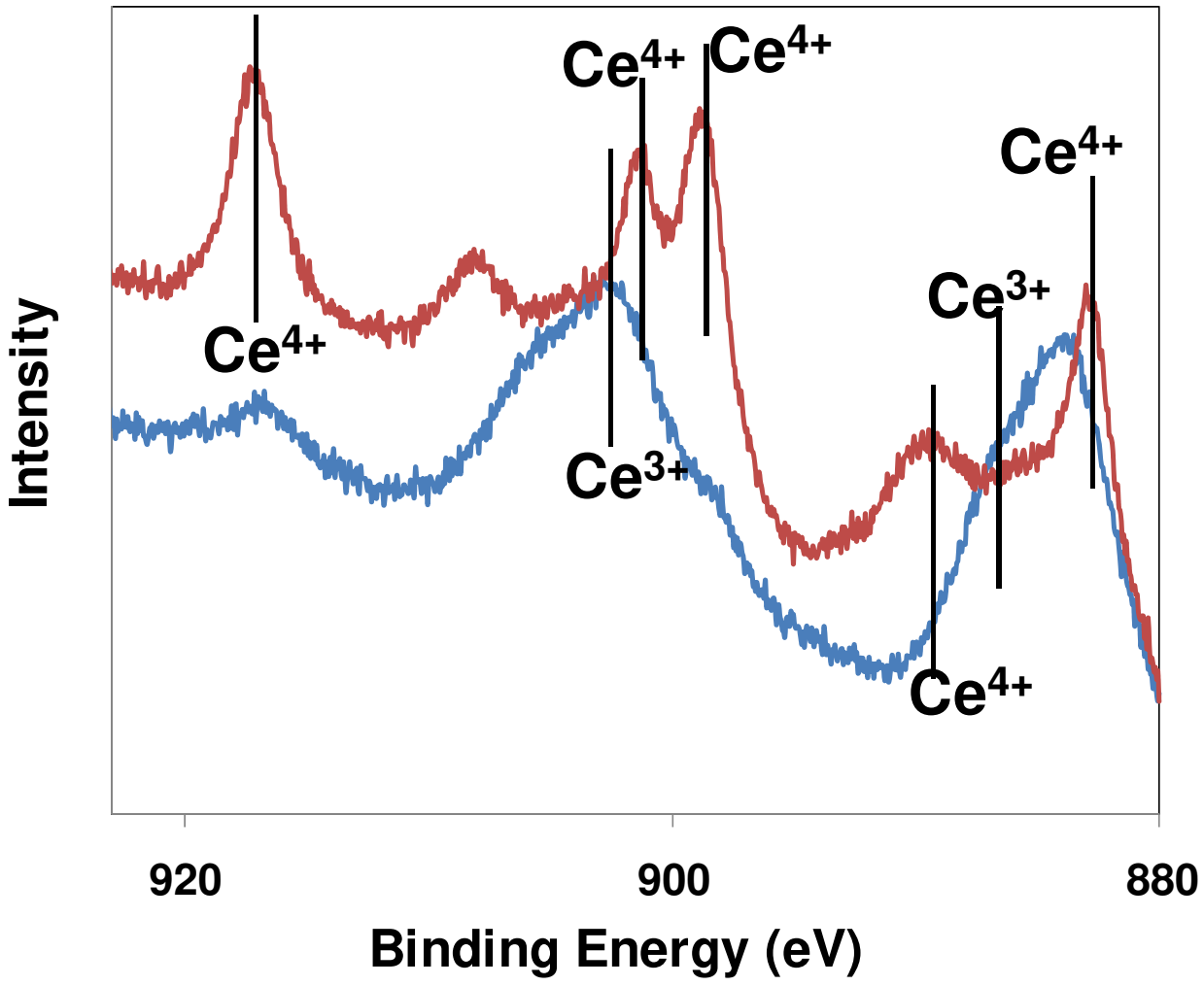

Figure 9-2: X-ray photoelectron spectra of nanoceria in water and dextran. The characteristic peaks at 885.0 and 903.5 eV correspond to cerium in 3+ oxidation state while peaks at 882.1, 898.0, 900.9 and 916.4 eV correspond to cerium in 4+ oxidation state shows that nanoceria synthesized in water has higher Ce^{3+} oxidation state as compared to ceria in dextran

The reversible switching of oxidation states of nanoceria upon addition of hydrogen peroxide was also tested and monitored using UV-Visible spectrophotometry. It can be observed from figure 9.3 that the nanoceria synthesized in water regenerates the Ce^{3+} oxidation state within 7-10 days while the nanoceria synthesized in dextran takes more than 21 days to regenerate the oxidation state. This indicates that the reversibility of oxidation state is more easily achieved in water than in dextran and thus it is expected that nanoceria in water may exhibit better radical scavenging properties than nanoceria in dextran.

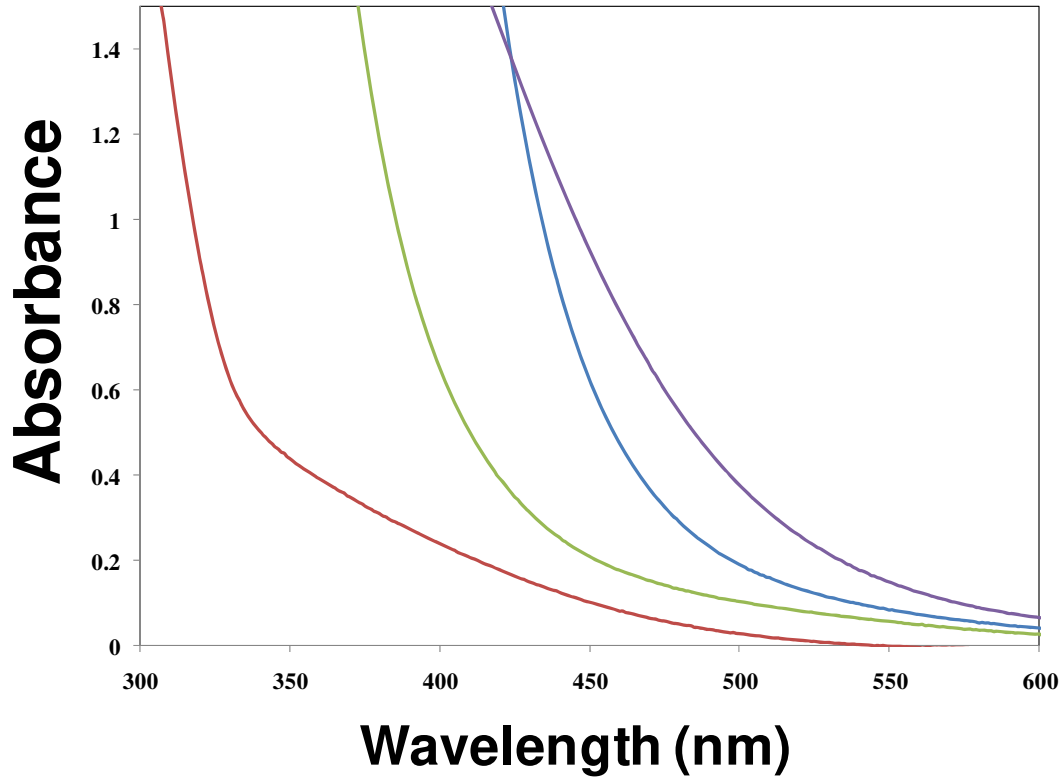

Figure 9-3 UV-Visible spectra of nanoceria synthesized in water and dextran. The graph shows the shift in oxidation state of cerium from 3+ oxidation state to 4+ in case of water based nanoceria while in dextran the oxidation state shifts to predominantly 4+ oxidation state within 7 days . The predominant oxidation state in dextran based sample is Ce^{4+} indicating that water based sample has more reduced nanoceria than the dextran based sample

It was shown previously that the superoxide dismutase activity of nanoceria is proportional to the concentration of Ce^{3+} ions. During the synthesis of scaffolds both the preparations of nanoceria

were subjected to calcination after the incorporation of nanoceria in the scaffolds. This heat treatment can change the oxidation state of material drastically as compared to its native oxidation state in water. However, since the ceria in dextran showed low concentration of Ce^{3+} oxidation state to begin with, it is possible that it retained low concentration of Ce^{3+} post heat treatment. On the other hand the ceria synthesized in water may have retained slightly higher Ce^{3+} oxidation state upon calcination due to significantly higher concentration of Ce^{3+} to begin with. This could also explain the difference between the activity of ceria preparation in dextran and in water and could also be the reason that the ceria preparation did not produce a dramatic influence on the synthesis of collagen. Future studies will be aimed at the incorporation of nanoceria in the scaffold after the heat treatment of the scaffold to avoid the oxidation of reduced form of nanoceria.

Apart from reversibility of oxidation state, the role of oxygen vacancies have been debated as one of the prime factors involved in ability of nanoceria to act as a catalyst in either biological or materials world. The molecular level understanding of the mechanism of antioxidant behaviour of nanoceria is not achieved in case of biological application. However, based on unique observations pertaining to the role of oxygen vacancies in application such as catalysis (water gas shift, CO oxidation etc) one can assume that the oxygen vacancies can play a crucial role in imparting nanoceria its potent antioxidant properties. It was shown theoretically that superoxide radicals are immediately converted to peroxide on the surface of reduced cerium oxide and in turn oxidize the cerium to Ce^{4+} oxidation state. The peroxide molecule is attached to surface more strongly than the molecular oxygen. Thus by scavenging radicals or adsorbing oxygen species on its surface nanoceria can regulate molecular oxygen available to cells. It is known that the level of oxygen is very crucial for growth and proliferation of cells especially HMSCs and

suggests that the increased osteoblastic differentiation observed in case of nanoceria may involve a control of molecular oxygen level by changing the partial pressure of oxygen available to cells. This suggests that the increase in collagen production by nanoceria may involve a co-relation of the surface oxygen vacancies which can regulate the oxygen partial pressure in culture medium. Further understanding of this mechanism will be a subject of future studies and require a multitude of controlled experiments.

10 APPENDIX D: LIST OF PUBLICATIONS

The following papers were published as a part of the work done during the five years of doctoral research. These works relate to the various projects that have been undertaken and some of them were not a part of the thesis but helped in increasing the fundamental understanding of the material science.

Publications

1. **A.S. Karakoti**, S. Singh, A. Kumar, M. Malinska, K. Wozniak, W. Self and S. Seal, "PEGlyated Nanoceria as Radical Scavenger with Tunable Redox Chemistry" ***JACS Comm***. 2009 131, 14144-145
2. **A.S. Karakoti**, Satyanarayana VNT Kuchibhatla, D.R. Baer, S. Thevuthasan, Dean C. Sayle, S. Seal, Self assembly mechanism of nanostructures in ice moulds, ***Small***, 2008, 4, 1210-16.
3. **A.S. Karakoti**, Nancy A. Monteiro-Riviere, R Narayan, William Self, J. McGinnis and S. Seal, Nanoceria as antioxidant - synthesis and biomedical applications, ***JOM***, March 2008, 33-37.
4. **A.S. Karakoti**, Satyanarayana VNT Kuchibhatla, K. Suresh Babu, S. Seal, Direct synthesis of ceria nanoparticles in polyhdroxyl groups using different oxidizing agents, ***Journal of Physical Chemistry C***, 2007; 111(46); 17232 -40
5. **A.S. Karakoti**, L.L. Hench, and S. Seal, The potential toxicity of nanomaterials—the role of surfaces, ***JOM***, 2006, 58(7), 77 - 81

6. **A.S. Karakoti**, R.Filmalter, D.Bera, Satyanarayana VNT Kuchibhatla, A.Vincent, and S.Seal, Spiral growth of one dimensional titania nanostructures using anodic oxidation, ***Journal of Nanoscience and Nanotechnology***, 6, 2006, 2084-89

7. J. Anderson, **A.S. Karakoti**, D.J. Diaz and S. Seal " Nanoceria modified platinum-gold composite electrodes for electrochemical oxidation of methanol and ethanol in acidic media" accepted ***Journal of Physical Chemistry C***

8. A. Vincent, T. Inerbaev, S. Babu, **A.S. Karakoti**, W. T. Self, A.E. Masunov and Sudipta Seal, "*Tuning Hydrated Nanoceria Surfaces: Experimental/Theoretical Investigations of Ion Exchange and Implications in Organic Inorganic Interactions*" ***Langmuir*****,** published on Web

9. R.K. Sharma, A.S. Karakoti, S. Seal, L. Zhai, " Multiwall carbon nanotubes poly(4-styrenesulfonic acid) supported polypyrrole/manganese oxide nano-composites for high performance electrochemical electrodes", ***Journal of Power Sources***, 2010, 195, 1256-1262

10. T. Pirmohamed, J. Dowding, B. Wasserman, E. Heckert, **A.S. Karakoti**, J.E.S. King, S. Seal and W.T. Self "*Nanoceria Exhibit Redox State Dependent Catalase Mimetic Activity*" ***Chem Comm*** accepted

11. S. Hirst, **A.S. Karakoti**, R. Tyler, N. Sriranganathan, S. Seal and C. Reilly, "Inhibition of inflammatory mediator production by cerium oxide nanoparticles" ***Small,*** 2009, 24, 2848-2856

12. B. Schanen, **A.S. Karakoti,** S Seal, D. Drake, W Warren and William Self, Exposure to Titanium dioxide Nanomaterials Provokes Inflammation of an in vitro Human Immune Construct, ***ACS Nano***, 2009, 3, 2523 - 32

13. A Kumar, S Babu, **A.S. Karakoti**, A Schulte and S Seal, "Luminescence Properties of Europium Doped Cerium Oxide Nanoparticles- Role of Vacancy and Oxidation States" ***Langmuir***, 2009, 25(18), 10998-1007

14. SVNT Kuchibhatla, **A.S. Karakoti**, D.C. Sayle, H. Heinrich and S. Seal, Symmetry driven spontaneous self assembly of nanoscale ceria building blocks to fractal superoctahedral, ***Crystal Growth and Design***, 9(3), 2009, 1614 – 20 **(Cover Page Article)**

15. Eric Heckert, **A.S. Karakoti**, Sudipta Seal, and William T. Self, The role of cerium redox state in the catalytic reaction of superoxide with nanoceria, ***Biomaterials***, 2008, 29, 2705-09.

16. D.C. Sayle, S. Seal, Z. Wang, B.C. Mangili, D.W. Price, **A.S. Karakoti**, S.V.N.T. Kuchibhatla, Q. Hao, G. Mobus, X. Xu, T.X.T Sayle, Mapping nanostructure: A systematic enumeration of nanomaterials by assembling nanobuilding blocks at crystallographic positions, ***ACS NANO***, 2008, 2, 1237-51.

17. D.R. Baer, J.E. Amonette, M.H. Engelhard, D.J. Gaspar, **A.S. Karakoti**, S. Kuchibhatla, P. Nachimuthu , J.T. Nurmi, Y. Qiang, V. Sarathy, S. Seal, A. Sharma, P.G. Tratnyek, C.M. Wang, Characterization challenges for nanomaterials, ***Surface and Interface Analysis***, 2008, 40, 529-37

18. K. Balani, T. Zhang, **A.S. Karakoti**, W.Z. Li, S. Seal, A. Agarwal, In situ carbon nanotube reinforcements in a plasma-sprayed aluminum oxide nanocomposite coating, ***Acta Materialia***, 56, 2008, 571–579

19. K.S. Babu, **A.S. Karakoti** and S. Seal, A cost effective nanostructure rare earth catalytic coating to prevent environmental degradation" **Steel Tech**, 2008, 2, 26-29.

20. D.J. Diaz, N. Greenletch, A. Solanki, **A.S. Karakoti**, S. Seal, Novel nanoscale ceria–platinum Composite electrodes for direct alcohol electro-oxidation, ***Catalysis Letters***, 119, 2007, 319-326

21. SVNT Kuchibhatla, **A.S. Karakoti**, D. Bera and S. Seal, "One Dimensional Nanomaterials", ***Progress in Materials Science***, 52, 2007, 699-914 (Ranked as Number 1 and 2 since 2007)

22. A. Vincent , S. Babu, E. Brinley, **A.S. Karakoti**, S. Deshpande, S. Seal, Role of catalyst on refractive index tunability of porous silica antireflective coatings by sol-gel technique, ***Journal of Physical Chemistry*** C 2007; 111, 8291-8298

23. S. Deshpande S, **A.S. Karakoti**, G. Londe, H.J. Cho, S. Seal, "Room temperature hydrogen detection using 1-d nanostructured tin oxide sensor" Journal of Nanoscience and Nanotechnology, 2007, 7, 3354-57

24. S.V.N.T Kuchibhatla, **A.S. Karakoti** and S. Seal, Hierarchical assembly of inorganic nanostructure building blocks to octahedral superstructures — a true template-free self-assembly, ***Nanotechnology***, 2007, 18, 075303-307

25. S.V.N.T Kuchibhatla, **A.S. Karakoti** and S. Seal, Colloidal stability by surface modification, ***JOM***, 2005, 57, 52-56

26. **A.S. Karakoti**, D.K. Pattanayak, A.S. Khanna, T.R. Rama Mohan, V.P. Soni, Polymer/AW coating on stainless steel, ***Transactions of PMAI***, Vol. 29, December 2003, pages: 06 – 12

Manuscripts Submitted

1. T. Inerbaev, **A.S. Karakoti** , A.E. Masunov, SVNT Kuchibhatla, S Seal, "*Origin of Blue Shift in the Optical Spectra of Cerium Oxide Nanoparticles in Aqueous Solution*" Submitted to PRL
2. **A.S. Karakoti**, S. Singh, J. Dowding, S. Seal and W. Self, "*Redox Active Radical Scavenging Nanomaterials*" submitted to Chemical Society Reviews
3. S. Singh, A. Kumar**, A.S. Karakoti**, S. Seal, W. Self, "*Active Uptake Mechanism and Widespread Cellular Distribution of Rare Earth Oxide Nanoparticles* " Submitted to Chemistry of Materials
4. **A.S. Karakoti,** O. Tsigkou, S. Yue, J.R. Jones, S. Seal, "*Rare earth oxides as nanoadditives in novel 3-D nanocomposite scaffolds for bone regeneration*" submitted to Nanoscale
5. A.S. Karakoti, J.E.S. King, A. Vincent and Sudipta Seal "*Synthesis Dependent Core Level Binding Energy Shift in the Oxidation State of Platinum Coated on Ceria-Titania Controls the Activity of Methanol Decomposition*" Submitted to Applied catalysis A

Manuscripts under Preparation

1. Satyanarayana VNT Kuchibhatla, **A.S. Karakoti**, S. Samudrala, S. Seal, M.H. Engelhard, J. E. Amonette, Charles Windisch, D.R.Baer, S. Thevuthasan, "*Influence of*

aging and environment on nanoparticle chemistry – implication to confinement effects in nanoceria"

2. **A.S. Karakoti**, A. Vincent, T. Spalding, D. Patel, P. Nachimuthu and S. Seal, "Tunable and selective decomposition of methanol using hybrid ceria titania nanostructures"

3. Satyanarayana VNT Kuchibhatla, **A.S. Karakoti**, Maura Malinka, Krzysztoff Wozniak and Sudipta Seal, *" Tuning the Band Gap of Nanoceria using Mono and Polyol's"*

4. **A.S. Karakoti,** J. King, S. Singh, W. Self and S Seal "*Molecular weight dependence of polyethylene glycol on the size, shape, stability and redox activity of cerium oxide nanoparticles*"

5. **A.S. Karakoti,** J. King, S. Singh, W. Self and S Seal, "*PEG-Dex copolymers for enhanced stability and activity of cerium oxide nanoparticles against free radical damage in neutral to alkaline conditions*"

11 APPENDIX E: LIST OF COPYRIGHTS

AMERICAN CHEMICAL SOCIETY LICENSE
TERMS AND CONDITIONS

May 26, 2010

This is a License Agreement between Ajay S Karakoti ("You") and American Chemical Society ("American Chemical Society") provided by Copyright Clearance Center ("CCC"). The license consists of your order details, the terms and conditions provided by American Chemical Society, and the payment terms and conditions.

All payments must be made in full to CCC. For payment instructions, please see information listed at the bottom of this form.

License Number	2436571294092
License Date	May 26, 2010
Licensed content publisher	American Chemical Society
Licensed content publication	The Journal of Physical Chemistry C
Licensed content title	Direct Synthesis of Nanoceria in Aqueous Polyhydroxyl Solutions
Licensed content author	A. S. Karakoti et al.
Licensed content date	Nov 1, 2007
Volume number	111
Issue number	46
Type of Use	Thesis/Dissertation
Requestor type11	Not specified
Format	Electronic
Portion	50% or more of original article
Author of this ACS article	Yes
Order reference number	
Title of the thesis / dissertation	Tuning the Properties of Nanomaterials as a Function of Surface and Environment
Expected completion date	Aug 2010
Estimated size(pages)	203
Billing Type	Invoice
Billing Address	12021 Solon Drive Apt 116 Orlando, FL 32816 United States
Customer reference info	
Total	0.00 USD
Terms and Conditions	

Thesis/Dissertation

AMERICAN CHEMICAL SOCIETY LICENSE
TERMS AND CONDITIONS

May 26, 2010

This is a License Agreement between Ajay S Karakoti ("You") and American Chemical Society ("American Chemical Society") provided by Copyright Clearance Center ("CCC"). The license consists of your order details, the terms and conditions provided by American Chemical Society, and the payment terms and conditions.

All payments must be made in full to CCC. For payment instructions, please see information listed at the bottom of this form.

License Number	2436570565023
License Date	May 26, 2010
Licensed content publisher	American Chemical Society
Licensed content publication	Journal of the American Chemical Society
Licensed content title	PEGylated Nanoceria as Radical Scavenger with Tunable Redox Chemistry
Licensed content author	Ajay S. Karakoti et al.
Licensed content date	Oct 1, 2009
Volume number	131
Issue number	40
Type of Use	Thesis/Dissertation
Requestor type11	Not specified
Format	Electronic
Portion	50% or more of original article
Author of this ACS article	Yes
Order reference number	
Title of the thesis / dissertation	Tuning the Properties of Nanomaterials as a Function of Surface and Environment
Expected completion date	Aug 2010
Estimated size(pages)	203
Billing Type	Invoice
Billing Address	12021 Solon Drive Apt 116 Orlando, FL 32816 United States
Customer reference info	
Total	0.00 USD
Terms and Conditions	

Dear Customer,

Thank you for your email.

We hereby grant permission for the requested use expected that due credit is given to the original source.
Please note that the author's permission is also required.

Please note that we only grant rights for a printed version, but not the rights for an electronic/ online/ web/ microfiche publication, but you are free to create a link to the article in question which is posted on our website (http://www3.interscience.wiley.com)

- ⇨ ***You may use the version of the contribution as originally submitted for publication for an electronic presentation of the thesis. The contribution <u>may not be updated or replaced</u> with the published version. The version posted must contain a legend as follows: This is the pre-peer reviewed version of the following article: FULL CITE.***

With kind regards

Bettina Loycke
****
Bettina Loycke
Senior Rights Manager
Wiley-VCH Verlag GmbH & Co. KGaA
Boschstr. 12
69469 Weinheim
Germany

Phone: +49 (0) 62 01- 606 - 280
Fax: +49 (0) 62 01 - 606 - 332
Email: rights@wiley-vch.de
